Structural and Wetting Studies of Visible Light Active TiO$_2$ Thin Films

By

Madhusmita Sahoo

(Enrolment No. PHYS 02 2011 04 014)

Indira Gandhi Centre for Atomic Research, Kalpakkam, India.

A thesis submitted to the

Board of Studies in Physical Sciences

in partial fulfillment of requirements

for the Degree of

DOCTOR OF PHILOSOPHY

of

HOMI BHABHA NATIONAL INSTITUTE

July, 2018

Homi Bhabha National Institute

Recommendations of the Viva Voce Board

As members of the Viva Voce Committee, we certify that we have read the dissertation prepared by **Madhusmita Sahoo** entitled **"Structural and Wetting Studies of Visible Light Active TiO$_2$ Thin Films"** and recommend that it may be accepted as fulfilling the thesis requirement for the award of Degree of Doctor of Philosophy.

(Chairman- Dr. M. Kamruddin) Date: 20/12/18

(Guide/Convener- Dr. Tom Mathews) Date: 20/12/18

C. S.
(External Examiner - Dr. C. S. Gopinath) Date: 20/12/2018

(Member 1: Dr. H. N. Jena) Date: 20/12/2018

S. Tripurasundari
(Member 2: Dr. S. Tripurasundari) Date: 20/12/18

Arindam
(Member 3: ~~Dr.~~ Dr. Arindam Das) Date: 20/12/2018

Final approval and acceptance of this thesis is contingent upon the candidate's submission of the final copies of the thesis to HBNI.

I hereby certify that, I have read this thesis prepared under my direction and recommend that it may be accepted as fulfilling the thesis requirement

Date: 20.12.2018

Place: Kalpakkam

(Dr. Tom Mathews)

STATEMENT BY AUTHOR

This dissertation has been submitted in partial fulfillment of requirements for an advanced degree at Homi Bhabha National Institute (HBNI) and is deposited in the Library to be made available to borrowers under rules of the HBNI.

Brief quotations from this dissertation are allowable without special permission, provided that accurate acknowledgment of source is made. Requests for permission for extended quotation from or reproduction of this manuscript in whole or in part may be granted by the Competent Authority of HBNI when in his or her judgment the proposed use of the material is in the interests of scholarship. In all other instances, however, permission must be obtained from the author.

Date: 20/12/2018.
Place: Kalpakkam.

Sahoo

Madhusmita sahoo

DECLARATION

I, hereby declare that the investigation presented in the thesis has been carried out by me. The work is original and has not been submitted earlier as a whole or in part for a degree / diploma at this or any other Institution / University.

Sahoo

Madhusmita Sahoo

List of Publications

PUBLICATIONS

(a). Published

1. **Madhusmita Sahoo**, Tom Mathews, Rajini P Antony, D. Nandagopala Krishna, S. Dash, A. K. Tyagi, "Physico-chemical Processes and Kinetics of Sunlight-Induced Hydrophobic ↔ Superhydrophilic Switching of Transparent N-Doped TiO_2 Thin Films." *ACS Appl. Mater. Interfaces*, **2013**, *5*, 3967-3974.

2. **Madhusmita Sahoo**, A. K. Yadav, S. N. Jha, Dibyendu Bhattacharyya, Tom Mathews, N. K. Sahoo, S. Dash, A. K. Tyagi, "Nitrogen Location and Ti-O Bond Distances in Pristine and N-Doped TiO_2 Anatase Thin Films by X-ray Absorption Studies." *J. Phys. Chem. C*, **2015**, *119*, 17640-17647.

(b). Communicated

1. **Madhusmita Sahoo**, A. K. Yadav, Subrata Ghosh, S.N. Jha, Dibyendu Bhattacharyya, Tom Mathews, "Ti K-edge Spectra of Spray Pyrolysis Synthesized Oxygen Deficient Anatase TiO_2 Thin Films." *Communicated to JPCC.*

(c). Other publications not included in the thesis

1. Padmalochan Panda, R. Ramaseshan, **Madhusmita Sahoo**, Nanda Gopala Krishna, A. K. Yadav, S. N. Jha, D. Bhattacharyya, "Local crystal structure in the vicinity of Cr in doped AlN thin films studied by X-ray absorption spectroscopy. " *Phys. Chem. Chem. Phys.* **2018**, *20*, 13084-13091.

(d). Conference/Symposium:

1. **Madhusmita Sahoo**, Tom Mathews, S. Dhara, S. Dash, A. K. Tyagi, Ultrasonic spray pyrolytic synthesis and characterisation of ZnO-TiO_2 nanocomposite thin films, International Conference on Nanoscience, Engineering and Technology (ICONSET 2011), IEEE, 10.1109/ICONSET.2011.6167962.

2. **Madhusmita Sahoo**, Ashok kumar Yadav, S N Jha, Dibyendu Bhattacharyya, Tom Mathews, S. Dash, Ti K-edge X-ray Absorption Spectra of Spray Pyrolysis Synthesized TiO_{2-x} and $TiO_{2-x}N_x$ Thin Films, DAE-SSPS (Dec 26-30) 2016.

Sahoo

Madhusmita Sahoo

Dedicated To

Lord Jagannath

Acknowledgments

It is a pleasure to express my sincere and heartfelt gratitude to Dr. Tom Mathews for his excellent guidance and encouragement. His attention to details have helped me improve my skills in writing and comprehension. His cool persona and ability to think out of the box is something I would like to emulate. It is a pleasure to work with him and push beyond the limit to achieve superior scientific goals. I would like to express my heartfelt gratitude to Dr. Tripura Sundari, who devoted her precious time to read through a part of my thesis. Apart from that i will always remain indebted to her for all her support in personal space, which made my life easier at a distant place away from my hometown. I am thankful and find myself extremely lucky to have interacted with few great and dedicated researchers during the course of my Ph.D work. Dr Sivakumar's mathematical skills to explain complex equations in simpler terms has left me amazed and helped me sail through crucial junctures of data analysis. I am thankful to Dr Ashok ku Yadav, who guided me through the XAS analysis even in night, without whom this thesis would not have become a reality. His scientific temperament is something which i would like to imitate. I appreciate the friendly nature of Dr S N Jha and Dr Dibyendu Bhattacharya who encouraged me to explore synchrotron studies and extended beam time to conduct the experiments. I remain thankful to both of them.I am grateful to Dr S Raju for discussing research ideas with me which enabled me to frame my research work. I would like to extend my sincere thanks to the doctoral committee members Dr. M kamaruddin, Dr Arindam Das, Dr H.N Jena, Dr S Dhara for their comments and suggestions. I would like to thank Prof. N. V. Chandra Shekar, Dean and Prof. B. V. R. Tata, former Dean, Physical Sciences for their support.

I thank my juniors, whose presence in the lab and township made my stay pleasant. My special thanks to Subrata Ghosh, Soumee Chakraborty, Herojit loushambam, Santanu Parida, Padmalochan Panda for proof reading my manuscripts and thesis. I

thank all my co-authors for their suggestion and timely review of manuscripts. I thank my friends Vinita Daiya, Molly Mehra from other groups whose presence helped me relieve stress.

I am indebted to all my teachers for their excellent teaching and support. Above all I thank my friends and foe alike for teaching me lessons of life. I would also like to thank the office staff members of MSG for their help. I thank all, who have helped me in carrying out my research in a meaningful way.

I thank our present group direct Dr G Amarendra and our previous group director Dr C S Sundar for their support.

Synopsis

TiO_2 exists in three phases: anatase, brookite and rutile. Anatase and rutile are the common polymorphs of synthetic TiO_2. Experimental data on TiO_2 brookite is limited due to its rareness and difficulty in preparation. Among rutile and anatase, anatase has been found to have a wider applicability with optimum performance in the fields of photo-catalysis,[1] solar cell,[2] gas sensors,[3] hydrophobic -hydrophilic switching coatings,[4] antimicrobial coatings etc.[5] Since for all practical purposes rutile and anatase phase occur commonly, it is prudent to consider the properties of rutile and anatase while weighing their merits for photo-catalytic applications. It is known that charge carriers (electrons and holes) are created upon photo-irradiation when electrons jump from the highest occupied density of states (DOS) of valence band to the lowest occupied DOS of the conduction band. The utility of these charge carriers at the surface depends on the amount of charge carriers available on the surface. In anatase TiO_2, the transfer of charge carriers to the surface takes precedence over inter site transfer owing to the open (crystallographic) structure of anatase phase. In addition to this, the nature of optical absorption process also affects the photo catalytic process. It is known that rutile is a direct band gap semiconductor, while anatase has an indirect band gap. Hence, an electron can jump from valence band to conduction band in rutile without any help from the surrounding lattice, whereas it has to rely on surrounding phonons in case of anatase to acquire the necessary momentum to occupy an excited state. Phonon involvement increases recombination time. This, combined with the fact that the effective electron mass in rutile is about twenty times larger than in anatase, means more photoelectrons will reach the surface in anatase where they can interact with surface species. Hence, for the present study anatase phase of TiO_2 was chosen for various studies. However, anatase titanium dioxide is a wide band gap ($\sim$3.2eV) semiconducting oxide and one of the main issues associated with it is the requirement of UV radiation for charge carrier generation. The most abundant source of UV radiation is sun light which constitutes only $\sim 5\%$ of it and has been exploited for the photo-catalytic applications. It is well known that the visible region of solar spectrum is $\sim 50\%$ and the effective utilization of natural solar energy warrants the proper tapping of this part of spectrum too. Therefore, among several methods adopted in literature for utilizing the visible light radiation, nitrogen doping of TiO_2 is found to be the most viable method, taking into consideration the detrimental effects such as photo-corrosion, generation of electron-hole recombination sites etc.[6–11] However, introduction of an anion (nitrogen) in TiO_2 lattice results in creation of oxygen vacancy so as to maintain charge neutrality. Since, structure plays an important role in deciding the photo-activity, this thesis focuses on synthesizing phase pure anatase TiO_2, N- doped TiO_2, oxygen deficient TiO_2 (TiO_{2-x})films and studying the effect of N-doping and oxygen vacancy on its local structure. In addition, the visible light activity of N-doped anatase TiO_2 and TiO_{2-x} films are studied. A brief chapterwise outline of the thesis is given below.

Chapter 1: This chapter introduces three predominantly occurring phases of Titanium dioxide, their crystal structures, optical properties and rationale behind band gap tuning. Several methods of band gap tuning such as surface sensitization, transition metal doping, nonmetal doping are briefly discussed with special emphasis on nitrogen doping owing to its technological importance and ease of synthesis. As, nitrogen doping leads to concomitant formation of oxygen vacancy in the TiO_2 matrix, the issues related to oxygen vacancy in TiO_2 are also discussed in great detail. The prevailing synthetic methods for N-doping and oxygen deficient TiO_2 are carefully scrutinized for finalizing the suitable synthetic method to be used in this study. The chapter ends with a presentation of scope of the work and investigations carried out in the present thesis.

Chapter 2: This chapter describes experimental methods used for synthesizing and characterising TiO_2, N-doped TiO_2 and oxygen deficient TiO_2 thin films. Synthesizing and characterising tools include a custom built spray pyrolysis unit and GIXRD (Grazing Incidence X-ray Diffractometer), FESEM (Field Emission Scanning Electron Microscope), Contact angle set-up, UV-Vis spectrometer, XPS (X-ray Photoelectron Spectrometer) , XAS (X-ray absorption Spectrometer; Indus-II, RRCAT, Indore), respectively. The chapter describes the basic principles of these techniques briefly. In addition, theoretical aspects and the fitting methodology of X-ray Absorption Spectra are discussed in detail.

Chapter 3: This chapter focuses on the synthesis and characterisation of N-doped anatase TiO_2 thin films. Emphasis is given on the optical properties, chemical and bonding nature of the nitrogen dopant. It also discusses the local structure of the N-doped anatase TiO_2 thin films. A brief description of the study and the discussion of the results covered in this chapter are given below. Nano-structured TiO_2 and N-doped TiO_2 thin films were synthesized using a cost effective and environment friendly spray pyrolysis technique by keeping the substrate temperature (T_s) at 400, 450, 500 and 550 °C. Crystallographic studies of the films confirmed formation of phase pure anatase TiO_2. Microstructure studies of these films revealed early stages of grain formation at T_s = 400 and 450 °C and well defined 20 nm wide and 10 nm long crystalline grains at T_s = 500 and 550 °C. Optical absorption studies carried out by using UV-Vis spectrometer revealed formation of interband states in case of N-doped TiO_2. The stoichiometry of the films was calculated from X-ray photoelectron spectra and the film synthesized at T_s = 450 °C is found to be nearly stoichiometric compared to the films synthesized at T_s = 400, 500 and 550 °C. The chemical nature and location of the nitrogen dopant was deduced using X-ray photoelectron spectroscopy (XPS) and X-ray absorption spectroscopy (XAS), respectively. Nitrogen 1s (XPS) spectra showed three peaks with an energy value of 396.6, 397.5 and $\sim$400eV, corresponding to substitutional nitrogen, interstitial nitrogen and as NO species, respectively.[12] Out of these three peaks, the peak at 396.6eV is traditionally referred as substitutional nitrogen by several authors. However, a careful reading of literature revealed that it corresponds to Ti-N bond of Titanium nitride, implying that it merely represents a Ti-N linkage and is not exactly substituting lattice oxygen. Moreover, XPS as a technique is capable of only differentiating different chemical surroundings around a particular atom and cannot pinpoint the location of the said atom. Hence, X-ray absorption studies (XAS) are undertaken to delineate the exact location of nitrogen. XAS is divided into three regions, viz. pre-edge, edge and post-edge. Pre-edge region revealed three peaks (A1, A2, A3) viz. 4957, 4961, and 4963 eV corresponding to 1s- $1t_{1g}$, 1s- $1t_{2g}$ and 1s- $3e_g$ electronic transition due to the distorted TiO_6 octahedron geometry in anatase phase of TiO_2.[13,14] Analysis of post edge region, which is also known as extended absorption fine structure (EXAFS), revealed that nitrogen in the TiO_2 host is located at a distance of $\sim$2.3 Å. The average $(Ti\text{-}O)_{axial}$ and $(Ti\text{-}O)_{equatorial}$ distances in pristine TiO_2 and their changes on nitrogen doping, corresponding to different nitrogen concentrations, were calculated from the EXAFS results. (Ti-O) axial and (Ti-O) equatorial bond lengths calculated from EXAFS are found to be in agreement with the theoretically calculated values by Ceotto et. al.[15] There is an overall increase in (Ti-O) axial and (Ti-O) equatorial bond distances in doped TiO_2 with respect to TiO_2 thin films, which is attributed to the dominant effect of nitrogen doped into the crystal lattice.

Chapter 4: This chapter describes synthesis of oxygen deficient TiO_2 (TiO_2-x) films and its characterisation using FESEM and GIXRD. Formation of oxygen vacancy and its effect on the local structure are studied using X-ray absorption spectrometer. The major findings of these studies are described below.

Anatase TiO_{2-x} films are synthesized by adopting a simple two step method, i.e., synthesizing anatase TiO_2 films followed by annealing in vacuum/ under hydrogen flow. Hence, anatase TiO_2 films are first synthesized by using the custom made spray pyrolysis set up as described in chapter 2. Since, it is known from chapter 3 that synthesis of TiO_2 at T_s = 450 °C yields stoichiometric anatase TiO_2 and synthesis at T_s = 500 °C yields well defined crystalline grains of anatase TiO_2, two synthesis temperatures i.e. ts= 450, 500 °C are chosen. The above synthesized films are then annealed at their respective ts in vacuum (for 2, 4. 6 and 8 hours) and under a reducing atmosphere (using H_2 gas) in a CVD chamber. As, annealing is known to cause phase transition of anatase to rutile, Grazing incidence X-ray diffraction (GIXRD) studies are undertaken. GIXRD of the films revealed that there is no change in crystal structure due to annealing. The crystallite sizes are calculated from the GIXRD spectra by using Scherrer Formula and are found to be in the range of 29 to 91 nm. The formation of oxygen vacancies, due to annealing in vacuum/ under H_2 flow, is ascertained by comparing the co-ordination number (C.N) obtained from EXAFS analysis with the C.N obtained by using the equation devised by Frenkel et. al. for calculating the C.N in nanoparticles.[16] The calculated C.N for the nano-sized crystallites of TiO_{2-x} films in the present study is found out to be 5.9. C.N obtained from EXAFS analysis is less than 5/5.7 for TiO_{2-x} films synthesized at T_s= 450 0C /500 °C. Comparison of C.N between EXAFS calculation and the theoretical calculation using Frenkel's equation proved that the oxygen vacancy is indeed induced due to vacuum/H_2 annealing and is not due to nano-sized crystallites. Furthermore, it is observed that the films synthesized and annealed at T_s = 450 0C are more oxygen deficient (CN of TiO_{2-x}- 450 °C is in the range of 4.6 to 4.8) compared to the films synthesized at T_s = 500 °C (CN of TiO_{2-x}- 500 °C is in the range of 4.6 to 5.7). This is attributed to the porous microstructure of the film synthesized at T_s = 500 °C, which undergoes surface restructuring and absorbs the desorbed oxygen species available near surface as pointed out by Krivtsov et.al.[17] In addition, the effect of oxygen vacancy on the local structure is understood by analyzing X-ray absorption near edge spectra (XANES). XANES of oxygen deficient TiO_2 films show three peaks (A_1, A_2, A_3) positioned around 4957, 4961, and 4963 eV with varying intensity. Analyzing peak position and height of A_1, A_2 and A_3 revealed that TiO_{2-x} films consist of both six and few five coordinated Ti centers. In addition to the above, oxygen vacancies are known to induce disorderness in the system, which is reflected in the integrated intensity of A_2 peak. To understand this, A_2 peak was fitted and its integrated intensity is found to be highest for the films annealed for 2 hours. This is in accordance with the fact that grain size and crystallinity increases with increase in annealing time as seen in the literature. This chapter also includes the comparison between theoretically simulated XAS spectra using FEFF with the experimental results to elucidate the pre-edge peak features of pure anatase TiO_2 and oxygen deficient anatase TiO_2. Few TiO_{2-x} films are also prepared by reducing the films under H_2 flow and are studied using XAS.

Chapter 5: This chapter focuses on the photo-induced wetting studies of N-doped anatase TiO_2 and TiO_{2-x} films. The major findings of the wetting studies are described below. It is observed that nitrogen doping transforms the surface of undoped TiO_2 from hydrophobic to super-hydrophilic upon sunlight irradiation. The surface of N-doped anatase TiO_2 reverted back to the hydrophobic one when kept in dark, indicating reversibility in wetting behaviour, known as switching behaviour. This chapter also includes kinetics of variation in contact angle upon photo irradiation and under dark condition. Wetting studies of TiO_2-x films revealed that TiO_{2-x} films attained super-hydrophilicity in 65mins.

Chapter 6: This chapter summarizes the major findings of the studies carried out on spray pyrolysis synthesized anatase TiO_2, N-doped TiO_2 and TiO_{2-x} films. The chapter ends with directions for future work. The important findings from these studies are as follows:

1. Synthesis of phase pure anatase TiO_2 and N-doped TiO_2 films (at T_s = 400, 450, 500 and 550 °C) by using custom made spray pyrolysis unit is evidenced by GIXRD studies. Microstructural evolution confirms formation of well defined grains for films synthesized at T_s= 500 and 550 °C.

2. Nitrogen doping in TiO_2 is confirmed from X-ray photo-electron spectra and its exact position is delineated by using X-ray absorption spectra. EXAFS analysis reveals that nitrogen in N-doped TiO_2 is interstitial in nature and is located at a distance of ~2.3 Å. The change in local structure owing to N-doping is reflected in Ti-O_{axial} and Ti-$O_{equatorial}$ bond lengths, which are found to be elongated in N-doped TiO_2.

3. Concomitant formation of oxygen vacancy owing to nitrogen doping is studied by synthesizing oxygen deficient TiO_2 (TiO_{2-x}) films, wherein oxygen vacancies are deliberately introduced in TiO_2 by following a post-synthesis annealing in vacuum/H_2 atmosphere. The formation of oxygen vacancies are confirmed from the EXAFS analysis of the TiO_{2-x} films. In addition, the change in local coordination i.e. the change in Ti-O_{axial} and Ti-$O_{equatorial}$ bond lengths due to oxygen vacancy matches with the theoretically calculated bond distance for oxygen deficient TiO_6 octahedrons.

4. The photo-induced wetting studies of N-doped TiO_2 films reveal, N-doped TiO_2 films become superhydrophilic upon 40 min sunlight irradiation and revert back to initial hydrophobic state when kept in dark for 5 days. This confirms the switching (hydrophobic ↔ superhydrophilic) behaviour and the rate of hydrophobic → superhydrophilic and superhydrophilic → hydrophobic transition is found to be 0.224 min^{-1} and 2.03 x10 $^{-4}$ min^{-1}, respectively.

Bibliography

[1] Shaham-Waldmann, N.; Paz, Y. Modified Photocatalysts, Photocatalysis and Water Purification. Wiley-VCH Verlag GmbH and Co. KGaA, 2013, 103-143.

[2] Richards, B. S. Comparison of TiO_2 and other Dielectric Coatings for Buried-Contact Solar Cells: a Review. Progress in Photovoltaics: Research and Applications 2004, 12, 253.

[3] Panjawi, N.; Naik, A.; Warwick, M. E. A.; Hyett, G.; Binions, R. The Preparation of Titanium Dioxide Gas Sensors by the Electric Field Assisted Aerosol CVD Reaction of Titanium Isopropoxide in Toluene. Chem. Vap. Deposition. 2012, 18, 102.

[4] Miyauchi, M.; Kieda, N.; Hishita, S.; Mitsuhashi, T.; Nakajimam, A.; Watanabe, T.; Hashimoto, K. Reversible Wettability Control of TiO_2 Surface by Light Irradiation, Surface Science, 511, 2002, 401.

[5] Muranyi, P.; Schraml, C.; Wunderlich, J. Antimicrobial Efficiency of Titanium Dioxide-Coated Surfaces. J. Appl. Microbiol. 2010, 108, 1966 - 1973.

[6] Serpone, N. Is The Band Gap of Pristine TiO_2 Narrowed by Anion- and Cation-Doping of Titanium Dioxide in Second-Generation Photocatalysts? J. Phys. Chem. B. 2006, 110, 24287.

[7] Sathish, M.; Viswanathan, B.; Viswanath, R. P.; Gopinath, C. S. Synthesis, Characterization, Electronic Structure, and Photocatalytic Activity of Nitrogen-Doped TiO_2 Nanocatalyst. Chem. Mater. 2005, 17, 6349.

[8] Mrowetz, M.; Balcerski,W.; Colussi, A. J.; Hoffmann, M. R. Oxidative Power of Nitrogen-Doped TiO_2 Photocatalysts under Visible Illumination. J. Phys. Chem. B. 2004, 108, 17269.

[9] Cong, Y.; Zhang, J.; Chen, F.; Anpo, M. Synthesis and Characterization of Nitrogen-Doped TiO_2 Nanophotocatalyst with High Visible Light Activity. J. Phys. Chem. C. 2007, 111, 6976.

[10] Tian, H.; Hu, L.; Zhang, C.; Liu, W.; Huang, Y.; Mo, L.; Guo, L.; Sheng, J.; Dai, S. Retarded Charge Recombination in Dye-Sensitized Nitrogen- Doped TiO_2 Solar Cells. J. Phys. Chem. C. 2010, 114, 1627.

[11] Raut, N. C.; Mathews, T.; Ajikumar, P. K.; George, R. P.; Dash, S.; Tyagi, A. K.Sunlight Active Antibacterial Nanostructured N-doped TiO_2 Thin Films Synthesized by an Ultrasonic Spray Pyrolysis Technique. RSC Adv. 2012, 2, 10639.

[12] Saha, N. C.; Tompkins, H. G. Titanium Nitride Oxidation Chemistry: An X-ray Photoelectron Spectroscopy Study, J. Appl. Phys. 1992, 72, 3072.

[13] Sandstrom, D. R.; Filby, R. H.; Lytle, F. W.; Greegor, R. B. Study of Ti in Solvent-Refined Coal by X-ray Absorption Spectroscopy. Fuel 1982, 61, 195.

[14] Chen, L. X.; Rajh, T.; Wang, Z.; Thurnauer, M. C. XAFS Studies of Surface Structures of TiO_2 Nanoparticles and Photocatalytic Reduction of Metal Ions. J. Phys. Chem. B 1997, 101, 10688.

[15] Ceotto, M.; Lo Presti, L.; Cappelletti, G.; Meroni, D.; Spadavecchia, F.; Zecca, R.; Leoni, M.; Scardi, P.; Bianchi, C. L.; Ardizzone, S., About the Nitrogen Loca-

tion in Nanocrystalline N-Doped TiO_2: Combined DFT and EXAFS Approach, J. Phys. Chem. C 2012, 116, 1764.

[16] Frenkel,A. I.; Yevick, A.; Cooper, C.; Vasic, R. Modeling the Structure and Composition of Nanoparticles by Extended X-Ray Absorption Fine-Structure Spectroscopy. Annu. Rev. Anal. Chem. 2011, 4, 23.

[17] Krivtsov,I.; Ilkaeva, M.; Salas-Colera, E.; Amghouz, Z.; Garcia,J. R.; Diaz, E.; Ordonez, S. ; Villar-Rodil, S. Consequences of Nitrogen-Doping and Oxygen Enrichment on Titanium Local Order and Photocatalytic Performance of TiO_2 Anatase. J. Phys. Chem. C. 2017, 121, 6770.

Contents

List of Figures

List of Tables

Chapter 1

Introduction

1.1 Titanium Dioxide

Semiconducting oxide materials have been the subject of intense research because of their practical applications. They also provide fundamental insight into the electronic processes involved when used in various applications. Within the class of inorganic semiconducting materials, oxide semiconductors display diverse range of properties, due to their dependence on the nature of metal – oxygen bonding. Wide band gap semiconducting oxides are of high interest as these exhibit wide ranges of electrical and optical properties. Among the wide band gap oxide materials, titanium dioxide (TiO_2) nanomaterials are used in a wide range of applications such as (photo)catalysis, sensor devices, paints, and dye-sensitized solar cells.[1–4] The material properties of TiO_2 nanoparticles are a function of crystal structure, nanoparticle size, and morphology, hence are strongly dependent on the method of synthesis.[5–7] TiO_2 exists in three main phases: anatase, brookite and rutile. Anatase and rutile are the common polymorphs of synthetic TiO_2. Experimental data on TiO_2 brookite is limited due to its rareness and difficulty in preparation. In view of this, a comparative discussion on Rutile and Anatase is taken up in the following section. Crystal structure and stability of these phases determine its usage. Since difference in crystal structure can lead to different mass densities, the electronic and optical properties of these two phases are distinctly different. This warrants phase selective synthesis for practical applications. The crystal structure of these three phases are discussed below and are represented in Fig 1.1. These structures can be described in terms of networks of edge - and/ or corner linked distorted TiO_6 octahedron building blocks. In the rutile structure, each octahedron is in contact with 10 neighbor octahedrons (two sharing edge oxygen pairs and eight sharing corner oxygen atoms). In the anatase structure, each octahedron is in contact with eight neighbors (four sharing an edge and four sharing a corner). In brookite, octahedrons share three edges and also corners. The octahedrons in each polymorph is distorted to different extent giving rise to different symmetry elements. In rutile, the O_h symmetry of an ideal octahedron is reduced to D_{2h} symmetry due to different in-plane (equatorial) and out-of-plane (axial) Ti–O bond lengths and two types of Ti–O–Ti in-plane bond angles deviating from 90°. In the anatase phase, additional displacements of the O ions from the equatorial positions generate a local D2h symmetry seen by the Ti ions. Due to stronger distortions in TiO_2 brookite, all bond lengths and bond angles slightly differ from each other, thus leading to the formal loss of local symmetry and C_1 symmetric TiO_6 units. Crystal structure data of rutile and anatase is given in Table 1.1.[8]

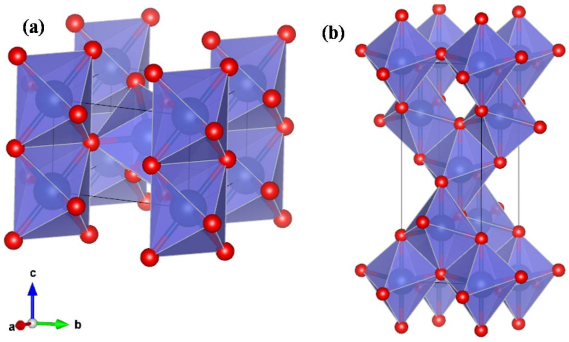

Figure 1.1 – Crystal structure of (a)Rutile, (b)Anatase.

In addition to the differences in crystal structures, it is pertinent to discuss the stability of anatase and rutile with respect to the size of the particle and the synthetic methodology. Ever since the discovery of size quantization effect in semiconductor

Table 1.1 – Crystal Structure data of anatase and rutile TiO_2

	Rutile	Anatase
Crystal structure	Tetragonal	Tetragonal
lattice constants Å	a=4.5936;	a=3.784
	c=2.9587;	a=9.515
Space Group	$P4_2/mmm$	$I4_1/amd$
Molecule/cell	2	4
Volume/molecule $Å^3$	31.2160	34.061
Density (g/cm^3)	4.13	3.79
Ti-O bond length Å	1.949(4)	1.965(4)
	1.980(2)	1.965(2)
O-Ti-O bond angle	81.2°	77.7°
	90.0°	92.6°

nanomaterials, research in nanostructured materials has generated considerable interest.[9,10] The properties of interest viz. optical, electronic and catalytic are found to be related to size in the nanoscale regime and drastically differ from those of bulk counterparts. With respect to photo-activity, TiO_2 nanoparticles have specific advantages in enhancing light absorption due to the presence of large fraction of atoms in surfaces and interfaces. It has also been observed that certain synthetic procedures lead to the metastable anatase phase owing to this size quantization effect. The stability and the occurrence of these two phases is described here in brief.

Rutile is the stable phase as a bulk material; however, as the size of the material goes down to the nanoscale regime, anatase becomes more stable. This is attributed to two main effects: surface energy and precursor chemistry. At very small particle dimensions, the surface energy is an important part of the total energy and it has been found that the surface energy of anatase is lower than those of rutile and brookite.[11,12] Surface energy considerations accurately describe the observation of a crossover size of about 30 nm where anatase nanoparticles transform to rutile.[13,14] Secondly, the crystal structure stability has been explained on the basis of a molecular picture, where the nucleation and growth of the different polymorphs of TiO_2 are determined by the precursor chemistry, which depends on the reactants used.[15–19] A complicating factor in the understanding of nanoparticle formation is the multitude of experimental conditions used for synthesis of the different TiO_2 phases, making it difficult to compare mechanisms. However, a few selected cases of phase specific synthesis methods is taken up for discussion here. Cheng et al.[15] and Yanagisawa et al showed that altering reaction conditions in hydrothermal synthesis route can lead to different phases.[16] It was observed that changing pH of the synthesizing medium favoured a certain phase e.g. acidic medium favoured rutile phase formation while basic medium favoured anatase phase.[15,16] Reyes et al.[19] have studied use of various reactants to obtain phase pure anatasa, rutile and brookite. They have shown that phase formation was achieved by hydrothermal treatment at elevated temperatures with the appropriate reactants. Anatase nanoparticles were obtained using acetic acid, while phase-pure rutile and brookite nanoparticles were obtained with hydrochloric acid at a different concentration. They proposed that anatase formation is dominated by surface energy effects, and that rutile and brookite formation follows a dissolution–precipitation mechanism, where chains of sixfold-coordinated titanium complexes arrange into different crystal structures depending on the reactant chemistry.[19] Similarly, Rafieian et al.[20] have studied the the synthesis of rutile and anatase thin films using Reactive magnetron sputtering. It was observed that oxygen deficient atmosphere during deposition lead to substoichiometric TiO_2 thin films, which in turn yield rutile phase upon annealing at a temperature below 500 °C. Anatase phase was obtained from annealing of stoichiometric films.[20]

From the application point of view rutile is preferred over anatase for optical and dielectric applications because of its high refractive index and dielectricity. Whereas, anatase is preferred for all applications related to photocatalytic activity due to its higher charge carrier mobility.

1.1.1 Optical properties

Anatase and rutile TiO_2 have band gaps of 3.2 and 3.0 eV, respectively and therefore, are visible light transparent. They have refractive indices higher than that of diamond and is highest of all the oxides. Hence, large and pure TiO_2 crystals have gem-like reflectance, refraction, and brilliance and are suitable for use in jewellery. The high refractive index has also enabled wide use of TiO_2 as a white pigment and also in many other optical applications. Because TiO_2 absorbs UV light and is biocompartible, it is used in sunscreen. Most pertinent for our discussion is the type of bandgap rutile and anatase possess. For any bandgap, the highest probability of creating charge carriers happens when there is coupling between highest density of states (DOS) at the maximum of the valence band and the minimum of the conduction band. For rutile, this happens at the same point in k-space making it a direct bandgap semiconductor – wherein an electron can jump to its excited state without any help from the surrounding lattice. For anatase, this happens at different points in k-space forcing a stimulated electron to rely on surrounding phonons to acquire the value of momentum necessary to occupy an excited state. Phonon involvement also increases recombination time. This, combined with the fact that the effective electron mass in rutile is about twenty times larger than in anatase, means more photoelectrons will reach the surface in anatase where they can interact with surface species. In all, the lifetime of $e^- - h^+$ pair in case of rutile is very less ($<$ 1 ns), whereas it is higher for anatase ($>$ 10 ns). Longer lifetime of $e^- - h^+$ pairs in anatase facilitates the trans-location of the photon-excited electrons and holes from the bulk to the surface, where the photochemical reactions take place.[21,22]

In addition to this, it will be apt to discuss about difference in absorption behavior of these two polymorphs from exciton point of view. The schematic of the recombination process is given in figure 1.2.

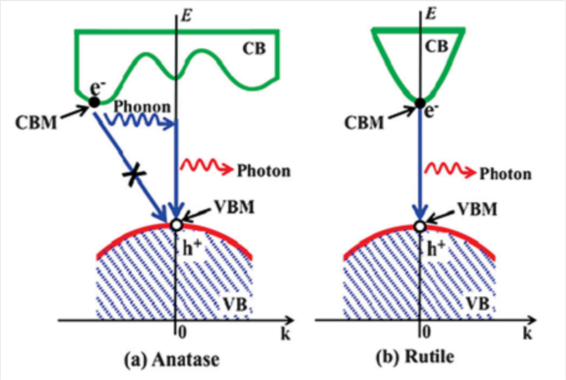

(a) Anatase (b) Rutile

Figure 1.2 – Schematic of recombination processes of photogenerated electrons and holes within (a) indirect gap anatase and (b)direct gap rutile.

Tang et al have studied the absorption behaviour of anatase and rutile at different temperatures and found that the absorption edge of rutile is characterized by phonon sidebands extending near the fundamental transition thresholds at low temperature. In contrast, the spectral dependence of the absorption edge in anatase fo11ows the Urbach rule at all temperatures down to liquid-helium temperature. They also concluded that excitons are self-trapped in anatase, while that in rutile are free.[23] The opposite nature of exciton states in anatase and rutile correlates with their structural differences of having different number of corner and edge sharing octahedrons as discussed earlier. Excitons in such structures are called charge-transfer excitons. They result from interaction between conduction-band electrons located on Ti $3d$ states and holes formed essentially by the O $2p$ states. Anatase has a more open structure compared to rutile owing to the fact that in rutile each TiO_6 octahedron is connected to ten neighboring ones on sharing a corner or an edge and in anatase each octahedron is coordinated only with eight neighboring ones. In consequence, in the anatase structure, the inter site transfer of excitons is weaker and the excitons travels to the surface mediated via phonons.[23]

1.1.2 Photon Induced Surface Properties

A material is known to be photo-responsive when various oxidative and reductive chemical reactions are induced on its surface in the presence of light. It is well-known that TiO_2 is a promising candidate for applications wherein UV light is used to induce reactions at surface and subsurface level. TiO_2 is chemically inert, biocompartible, photocatalytically active, easy to produce and use, sunlight activated, non-toxic and cheap. A vast amount of information about the light induced properties of TiO_2 especially photocatlytic properties is available in literature. Its photocatalytic properties would be discussed in detail in this section. Most of these articles are focused on TiO_2 powders and only a fraction deals with thin films. Although the present work is focused on thin films, a general understanding of materials properties requires the knowledge of all forms of TiO_2 because many important studies and major advances in properties are often first reported on powder samples.

The photocatalytic process begins with the absorption of light with energy greater than the band gap of the semiconducting photocatalyst (Figure 1.3) followed by the formation of electron-hole pair. The band gap of anatase and rutile phases are 3.2 and 3.0 eV, respectively. Some of the generated electron-hole pairs recombine immediately and release the energy as heat. Some of the electrons and holes avoid recombination and diffuse to the surface of the photocatalyst where they participate in charge transfer reactions with available surface species while the photocatalyst itself remains intact. The electrons and holes can either react directly with the target compounds or indirectly by forming first superoxide ($O_2^{\cdot -}$), singlet oxygen ($^1O\ _2$), hydroxyl radicals (.OH) or hydrogen peroxide (H_2O_2) from O_2, H_2O and OH groups which are typically present in atmospheric conditions. The organic compounds in contact are decomposed to CO_2, H_2O and mineral acids by these active oxygen species when the photocatalyst is irradiated with light of sufficient energy. Direct oxidation of the target compound by the photogenerated hole is also possible.

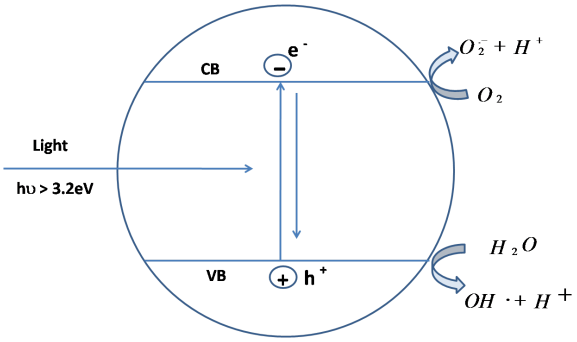

Figure 1.3 – Schematic of the main processes occurring at TiO_2 photocatalyst.

The oxidation and reduction mechanisms, involved are dependent on the properties of the photocatalyst, the nature of the compound being oxidized and the surrounding medium (water, air and vacuum). The necessary condition is that the reduction reactions by the photogenerated electrons and oxidation reactions by the photogenerated holes must balance precisely so that the photocatalyst itself remains intact. Among the two phases of TiO_2, anatase phase has been found to possess the best photocatalytic properties in spite of its larger band gap (3.2 eV) compared to rutile (3.0 eV).[24] The photocatalytic efficiency of TiO_2 depends also on the crystalline morphology and interfacial contact. The Fermi level in anatase is higher by about 0.1 eV than that of rutile.[25] Since, the anatase phase has a higher Fermi level than the rutile phase by about 0.1 eV, the anatase phase will have lower capacity to adsorb oxygen and higher degree of hydroxylation (i.e. number of hydroxy groups on the surface) and thus, should have greater photocatalytic activity than the rutile phase.[25–28]

As discussed earlier the anatase phase has a wider optical absorption gap, smaller electron effective mass and hence higher mobility. In addition to this the indirect band gap of anatase lead to decrease in the recombination rate of the $e^- - h^+$ pair generated upon illumination.

From the application point of view, due to its wide band gap only a small portion of the solar light, in the UV region, which occupies only 4-5 % of the total solar spectrum, can be absorbed. Thus, efficient absorption of the visible light which constitutes the major part of solar spectrum is prevented and the photocatalytic efficiency of TiO_2

is hindered. Therefore, a stable photocatalyst which could operate under visible light is an important subject of studies in the past ten years. Various semiconductors with smaller band gaps have been studied as potential candidates for visible light photocatalysis, but TiO_2 remains the most suitable candidate for large section of photocatalytic applications. Usually the smaller band gap materials are less stable and more prone to photocorrosion. A major advantage of TiO_2 is its good stability. In addition, the locations of the valence and conduction band edges in TiO_2 are suitable for photocatalysis.[29] Figure 1.4 depicts the valence band maximum and conduction band minimum of various semi-conductors with respect to the water redox couple. This helps in finding out which charge transfer reactions are possible on a given semiconductor. The location of the conduction band should be more negative than the reduction potential of O_2 so that O_2^- or HO_2 can be created. The production of O_2^- and HO_2 by the conduction band electrons is possible on TiO_2 but not on WO_3 or Fe_2O_3 (Figure 1.4). In turn, the location of the valence band should be more positive than the OH radical generation potential. This requirement is fulfilled by TiO_2, ZrO_2 and WO_3. It should also be kept in mind that the band edge positions and redox couples move to more negative potentials when the pH is raised.[30]

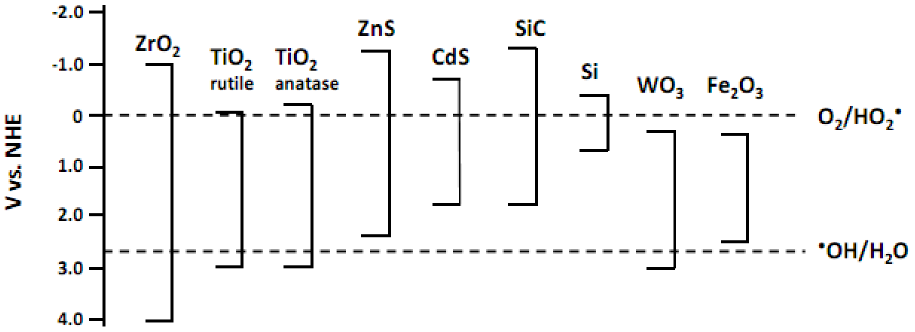

Figure 1.4 – Valence and conduction band positions of various semiconductors and relevant redox couples at pH = 0. (Drawn after refs. [14] and [15]).

1.2 Photo-induced wetting properties.

Materials with controllable wetting properties find applications in industrial processes, such as oil recovery, lubrication, liquid coating, printing, spray quenching, self cleaning surfaces, window shield etc. Wettability i.e. the ability of a liquid to wet a solid can be quantified by measuring the angle at which the liquid/vapor interface intersects the solid (Fig 1.5). This angle is referred to as the ”contact angle”. Usually many polar and non polar liquids viz. water, n-hexane, di-idomethane etc. are used to study wettability. Among them water is most widely used liquid to study wettability of film surfaces. Hence, contact angle referred henceforth will be with respect to the water contact angle. Small contact angles (<< 90°; hydrophillic) correspond to high wettability, while large contact angles (>>90°; hydrophobic) correspond to low wettability.

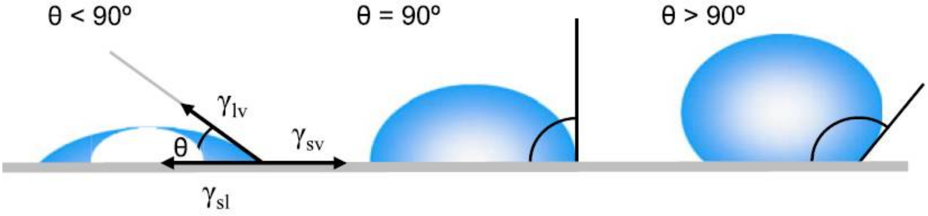

Figure 1.5 – Illustration of contact angles formed by sessile liquid drops on a smooth homogeneous solid surface.

A wide variety of approaches have been explored in the attempt to attain a system with controllable wetting properties. These approaches include manipulating magnetic fields over magnetically responsive materials,[31,32] applying electric fields – both static and oscillating,[33,34] combining materials with different wetting properties,[35] roughening or nanostructuring materials,[36–38] adjusting the pH of immersed surfaces,[39] forcing a liquid to spread at a certain speed,[40] directly changing the energy of a given surface via partial or complete coating,[41] and changing the frequency and/or the intensity of light irradiation on the substance under examination.[42,43] TiO_2

being a photoactive material as discussed in the previous section, this thesis will have specific focus on light induced surface wettability of N-doped TiO_2 and oxygen deficient TiO_2 thin films. It is known that stoichiometric TiO_2 surfaces change from hydrophobic to hydrophillic upon irradiation. However, due to the band gap energy, this photoinduced hydrophilicity (PIH) will manifest only when the wavelength of the irradiation is smaller than visible light wavelengths.[44] The presented experiments will explore applications based on this photoinduced wetting property as well as extending the range of response to visible light wavelengths. The details of theory pertaining to the contact angle will be discussed in Chapter 2. For the present discussion purpose, it can be concluded that pristine TiO_2 needs band gap alteration for utilization of visible light spectrum from solar radiation. There are numerous studies on the methods to utilize visible light using TiO_2 photocatlysts, which will be briefly discussed in the following section.

1.3 Doping

The efficient utilization of solar energy is one of the major goals in the modern era. Since the discovery of water splitting over TiO_2 by Fujishima and Honda,[45] the photocatalytic properties of TiO_2 have been widely studied. Of the materials being developed for photocatalytic applications, TiO_2) remains the most promising because of its high efficiency, low cost, chemical inertness, and photostability.[46–48] However, the widespread technological use of TiO_2 is impaired by its wide band gap (3.2 eV for anatase and 3 eV for Rutile), which requires UV irradiation for photocatalytic activation. Since, UV light accounts for only a small fraction (8%) of the sunlight compared to visible light (45%), any shift in the optical response of TiO_2 from the UV to the visible spectral range will have a profound positive effect on the photocatalytic efficiency of the material.[49,50] To engineer any change in the band gap, one needs to understand the band structure of the TiO_2, which is briefly discussed here. Electronic structure of TiO_2 has been determined experimentally by various groups.[51–54] The valence bands of TiO_2 can be split into three main regions: the σ bonding in the lower energy region mainly due to O-p σ bonds; the π bonding in the middle energy region; and O-p π states in the higher energy region due to O-p π nonbonding states where the hybridization with d states of Ti is almost negligible. The conduction band is split into Ti e_g (> 5 eV) and t_{2g} bands (< 5 eV). The d_{xy} states of t_{2g} are dominantly located at the bottom of the conduction band. The rest of the t_{2g} bands are anti-bonding with p states of oxygen. The main peaks of the t_{2g} bands are identified to be constituted by mostly d_{yz} and d_{zx} states.[51] The molecular orbital energy level diagram for TiO_2 is given in Fig 1.6.

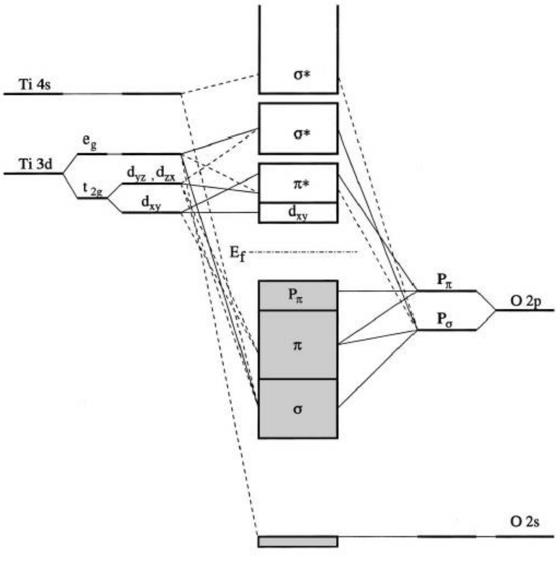

Figure 1.6 – Molecular orbital energy level diagram of TiO_2 taken from ref[51]

Several methods were adopted to shift the optical response of TiO_2 from the UV to the visible spectral range. Transition metal doping, non-metal doping, surface sensitization are the most widely used methods to change the optical response of TiO_2. Since doping is the widely used method for enhancing the visible light activity of TiO_2, the recent developments in the area is discussed in the next section. Among the other methods, surface sensitization is briefly discussed here.

In surface sensitization, different semiconductor photocatalysts having different energy levels are coupled.[55–58] The photocatalyst surface is loaded with another semiconductor of lower band gap that can be easily excited by visible light, such that the electron transfer from the conduction band of the narrow band gap semiconductor to that of TiO_2 can lead to efficient charge separation thereby reducing the $e^- - h^+$ recombination rates. The benefits of this method are expansion of absorption spectrum and efficient charge separation. The synergic effect of the composite semiconductors is used in dye-sensitized solar cells.

1.3.1 Doped TiO_2 Photocatalysts

An initial approach to shifting the optical response of TiO_2 from the UV to the visible spectral range has been the doping with transition metals and subsequently with anions. In particular, the primary aim was to narrow the band gap. When the band gap is narrowed, the oxidation potential of the valence band holes and/or the reduction potential of the conduction band electrons decreases and the photocatalytic activity can drop dramatically. This is the case especially if the conduction band edge drops below the reduction potential of O_2 or if the valence band edge rises so that the oxidation of H_2O or OH groups to OH is prevented. Therefore, it is beneficial to focus on the modification of the valence band while trying to narrow the band gap. When separate energy states are created in the band gap the outcome can also be a dramatic decrease in activity. This is caused by the creation of recombination centers for electrons and holes and it is not clear which energy states are beneficial and which are not.

Initially, doping of TiO_2 has been done with transition-metal elements.[59–62] In this case the modification of the electronic states occurs closer to the conduction band of TiO_2. This typically results when some of the titanium ions are substituted by other transition metal cations leading to mixing of the d orbitals or creation of separate impurity levels below the conduction band.

In the case of cation doping, the observed increase in photocatalytic activity is due to enhanced charge carriers in the presence of the effective dopant. However, metal doping has several drawbacks. The doped materials have been shown to suffer from thermal instability, and the metal centers act as electron traps, which reduces the photocatalytic efficiency. For this reason the photocatalytic activity is very sensitive to the concentration of the cationic dopant. The photoreactivity of cation doped TiO_2 was reported to be a complex function of the dopant concentration, the energy level of the dopants within the TiO_2 lattice, their d electron configuration, the distribution of dopants, and the light intensity.[63] The absorption of TiO_2 can be shifted perhaps more efficiently towards visible light with transition metal doping but the photocatalytic properties of these materials tend to be usually worse. Furthermore, the preparation of transition-metal doped TiO_2 requires more expensive ion-implantation facilities.[64,65]

Recently, it was shown that the desired band gap narrowing of TiO_2 can be better achieved by using anionic dopant species such as N, S, C and F rather than metals ions.[48–50,66,67] Especially N, S and C doping is expected to decrease the band gap of TiO_2 due to the metallic nature of the compounds TiN, TiS_2 and TiC. The resulting materials are often referred to as anion doped TiO_2 because the dopant is targeted to substitute O^{2-} ions in the TiO_2 lattice. The p orbitals of these dopants will mix with the O $2p$ orbitals in TiO_2 which causes the rise of the valence band. With small dopant levels, the mixing is not complete, however, isolated energy states just above the valence band are created. From the results of the research conducted on anion doping since early 1990s it can be assumed that the increase in photocatalytic activity is because of band gap narrowing and/or creation of mid gap localized states depending on dopant concentration. However, controversial experimental results have been reported in literature, and different theoretical models have been proposed to analyze these phenomena. The mechanisms of the optical and photocatalytic properties of anion-doped semiconductors are still open to discussion.

In addition to doping, creation of oxygen vacancies in TiO_2 has been reported to cause visible light photocatalytic activity as well.[68–70] It is well known that when TiO_2 is reduced it loses oxygen and visible light absorbing F-type color centers are created in the O vacancies.[71] Nakamura et al.[68] prepared reduced anatase TiO_2 powders by a H_2 plasma treatment at 400 °C. No difference in the crystal structure, crystallinity, and specific surface area was observed between raw TiO_2 and plasma-treated TiO_2 materials. Only the color of the powders turned from white to light yellow. The H_2 plasma-treated powders showed photocatalytic activity in NO_x removal, at wavelengths 450-600 nm, whereas the untreated powder did not. Activity under UV light was also slightly better compared to the undoped sample. Electron spin resonance (ESR) measurements with visible light irradiation showed a signal for the F^+ color center (O vacancy with one trapped electron) only in the plasma treated samples. The intensity of the signal correlated fairly well with the NO_x removal rate when different visible light wavelengths were used, thereby indicating that oxygen vacancy states played an important role in the visible light activity. The energy states caused by oxygen vacancies were reported to lie about 0.75-1.18 eV below the conduction band of TiO_2.[68] Excitation of electrons from the valence band to these states is thus possible using visible light. Holes left in the valence band are then free to oxidize compounds directly or through the creation of OH.

1.4 Nitrogen Doping

Stimulated by the report of Asahi et al. in 2001,[49] recently there has been an explosion of interest in TiO_2 doping with non-metal ions, especially with nitrogen.[72] Many authors have reported that N-doped titanium dioxide (N-TiO_2), shows a significant catalytic activity in various reactions performed under visible light irradiation.[50,73–77] However, there is also an open debate on how doping achieves this, as well as disagreements in many of the conclusions drawn from the results.[78–80] One of the reasons for this, is different strategies used for incorporation of nitrogen into titanium dioxide, either based on chemical reactivity i.e. sol–gel synthesis[73,74,81,82], chemical treatments of the bare oxide,[50,73,75,83] oxidation of titanium nitride,[84] or by physical methods such as ion implantation,[85–87] magnetron sputtering.[88,89] These different procedures lead to materials with different properties.

Asahi et al. carried out first-principles calculations to examine the effects of substitutional doping of C, N, S, P and F for O in anatase TiO_2.[49] The computational results suggested that nitrogen doping would be the best option. They prepared nitrogen doped TiO_2 films by sputtering a TiO_2 target in an N_2 (40 %)/Ar gas mixture and annealing at 550 ° C in N_2 gas for 4 hours. Nitrogen doped TiO_2 powders were also prepared by annealing pure anatase TiO_2 powder in NH_3 gas at 600 °C for 3 hours. The samples thus prepared were yellowish with a clear visible light absorption tail reaching to around 500 nm. The substitutional nitrogen doping in the samples was confirmed using XPS. They observed enhanced photocatalytic activities for nitrogen doped samples under UV light in comparison to undoped TiO_2.

The origin of visible light activity in nitrogen doped TiO_2 materials have been investigated and both substitutional and interstitial nitrogen doping has been found effective in increasing the visible light absorption .[49,75,90–92] Nitrogen doping has been also reported to lower the formation energy of oxygen vacancies which can have a strong impact on the photocatalytic properties.[86,92] Visible light photocatalytic activity in nitrogen doped TiO_2 has been reported in many cases but several studies have also reported serious degradation of photocatalytic performance in these materials.[93,94] It appears that nitrogen doping increases the amount of recombination centers in TiO_2 which destroys the photocatalytic activity. The preparation route obviously plays a decisive role in the outcome.

Properties and behavior of N-TiO_2 depends on the chemical nature and the location of nitrogen in the solid. Presence of different chemical species like NO_x,[73,74,91,92,95] substitutional N,[49,75,76,81] or NH_x[75] have been proposed. It is essential to know whether the species are primarily interstitial or substitutional, because the behavior of these two species is very different and affect the material properties accordingly. A schematic of the effect of substitutional and interstitial doping is given in Fig 1.7.

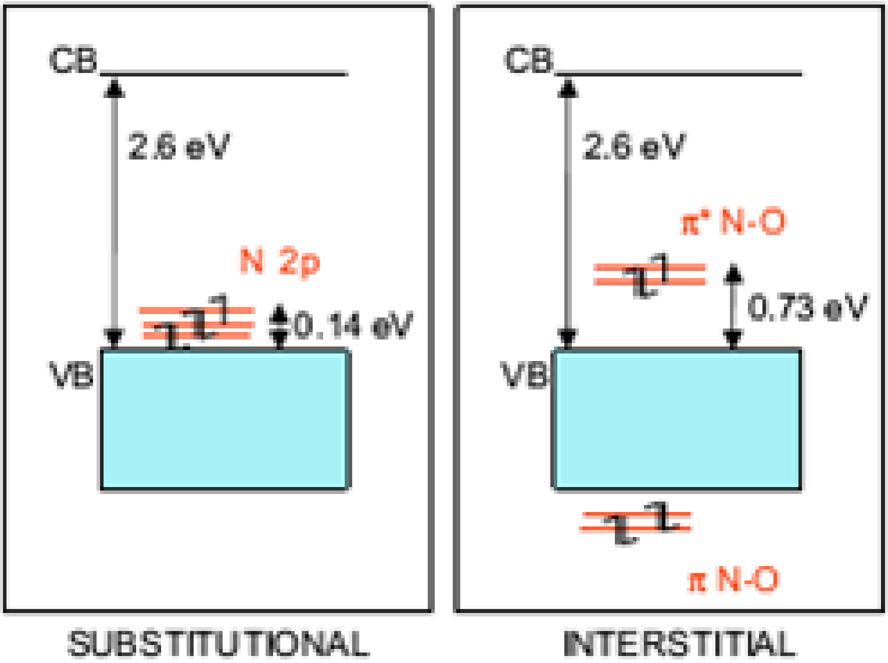

Figure 1.7 – Electronic structure of substitutionally and interstitially doped Anatase.[72]

In addition, in some cases doping reduces band gap of the solid owing to the valence band shift,[49,84,89] while in other cases dopant introduces localised impurity state in the band gap.[50,74,76,82] Interestingly, it appears that the N-doping induced modifications of the electronic structure may be slightly different for the anatase and rutile polymorphs of TiO_2. However, it is well established that in case of anatase TiO_2, nitrogen doping lowers the onset of optical absorption to the visible region of the electromagnetic spectrum.[75]

1.5 Oxygen Vacancies in TiO_2 matrix

When a nitrogen dopant is introduced into the matrix, oxygen vacancy formation is a concomitant effect. It has been calculated computationally that the cost of oxygen vacancies ($V_o$formation) in bulk anatase TiO_2 is drastically reduced in the presence of N-impurities, from 4.2 eV in pure TiO_2 to 0.6 eV in N-doped TiO_2.[72] Introducing defects such as oxygen vacancies is one among many methods to improve photoefficiency of TiO_2.[96] Oxygen vacancies create trap centers, rather than the recombination centers unlike the high doping case, and results in the variation of band gap of pristine TiO_2.[97]

1.5.1 Issues related to oxygen vacancies synthesis

A common factor that keeps appearing in studies on C and N doped visible light active TiO_2 photocatalysts is oxygen vacancies. Because they form so easily and have significant effects on the properties of TiO_2, their role is important. Recently, Kuznetsov et al. conducted a systematic analysis of the spectral features of various undoped and doped TiO_2 specimens reported in the literature.[98] The purpose of the work was to gain understanding on the origin of visible light activity in samples doped with different elements. First, absorption bands of various reduced undoped TiO_2 samples, mostly single crystal, were derived from the literature. Six absorption maxima could be distinguished ranging from 0.73 to 2.93 eV. Next, a careful analysis of the spectral features of various N, C and S doped samples revealed that they each contain the same three highest energy absorption bands as detected in the undoped reduced TiO_2 samples. The authors therefore concluded that the origin of visible light absorption in the visible light active doped TiO_2 samples are F-type color centers associated with oxygen vacancies. These same visible light absorbing defects exist in the undoped reduced TiO_2 and the role of the various dopants seems to be merely to stabilize and increase the number of these intrinsic defects.

Incorporation of oxygen vacancies into the matrix have been carried out using different approaches. These methods include surface hydrogenation,[99] vacuum activation[97] and plasma treatment.[100] However, all these methods have some pros and cons. In hydrogenation method, the surface of TiO_2 is terminated with hydrogen leading to an enhanced photocatalytic activity[101] in visible region; however, it is still unknown that how does the hydrogenation modify a surface to enhance its optical performance (photocatalytic activity).[102] The drawback of the hydrogenation method is that it requires high temperature and the obtained TiO_2 sample/film are black,[101] which makes the films unable for many optoelectronic applications, such as a transparent electrode in optoelectronic devices. Both the vacuum activation and plasma treatment methods create highly stable Ti 3+ and oxygen vacancies.[97,100]

In vacuum activation method, the sample exhibit higher absorption intensity but it appears brown in color that may render it unable for transparent electrode applications. In case of plasma treatment methods, generally hydrogen gas is used to create Ti^{3+} and oxygen vacancies in TiO_2, but it is avoidable to use such a hazardous and expensive gas. Other than hydrogen there are few reports on the use of argon[103], oxygen[104] and nitrogen plasma[105] for surface modification of TiO_2. It is also known that the implementation of gas in the treatment chamber may be hazardous; therefore, it is always required to avoid the use of hazardous gas, and to implement a simple and low cost approach to meet the requirements.[96] Hence, oxygen insertion pathway is optimised depending on the application.

1.6 TiO_2 Thin films

At the initial stage of the study of photocatalysis, TiO_2 was used in the form of powders. After photocatalytic reaction, a filtration step was needed to separate photocatalysts from slurry. This process adds extra cost to commercial applications. In order to solve the shortcoming of separating TiO_2 particles and avoid the filtration step, TiO_2 thin films were prepared using all types of common liquid and vapor phase deposition methods.[106–109] Photocatalytic results demonstrate that the films are almost as effective as powder TiO_2 catalysts which are used in slurry suspension systems. In the following section, the introduction to synthesis techniques of TiO_2

thin films is briefly discussed.

Among liquid based thin film deposition methods the sol-gel technique is by far the most popular in the preparation of photocatalytic TiO_2 thin films.[110–112] The sol-gel technique is a versatile method offering many possibilities to tune the properties of the thin film. Dopants and other modifying agents can be easily introduced to the starting sol to change the properties of the final film. Typically titanium salts or alkoxides are used as precursors. The precursors are hydrolyzed in a controlled manner thus forming a polymeric network of Ti-O bonds in a solvent. This state is called the sol, because it contains colloidal particles in solution. When the solvent evaporates to the extent that a continuous 3D network of solid material forms, the state has turned into a gel. The gel is dried to remove all the solvent and usually crystallized by annealing at high temperature.

Among other liquid phase methods, low temperature liquid phase preparation is also widely used. This include the direct growth of anatase from TiF_4 solutions and hydrothermal treatment of amorphous TiO_2 where temperatures close to 100 °C are enough to induce crystallization.[113,114]

Other than liquid phase methods, the other method which is used widely is gas phase methods. Gas phase methods generally lead to higher quality thin films than liquid phase methods. Lower impurity contents and higher film densities are usually obtained. Vapor deposited TiO_2 films are often crystalline in as-deposited condition itself and a separate heat treatment is not necessary. TiO_2 thin films prepared by the sol-gel technique typically require annealing temperatures around 400-500 °C to crystallize whereas vapor phase techniques can produce crystalline anatase TiO_2 at much lower temperatures, e.g. close to 200 °C. However, the vacuum equipment makes gas phase methods significantly more expensive as compared to liquid phase methods.

Sputtering is a physical gas phase deposition method where material is removed from a target using high energy ions and then collected on a substrate to grow a film. Argon is typically used as the sputtering gas. Magnetrons are usually used as the sputtering source. The method is principally very straightforward. Ideally, the growing film will have the same composition as the target. In the case of oxides, however, the films tend to become oxygen deficient. For this reason reactive sputtering is often used where a reactive gas like O_2 is introduced simultaneously into the deposition chamber. Doping can be accomplished by adding yet another gas such as N_2.[49]

Evaporation is another physical method used to grow photoactive TiO_2 thin films. In this method the source material is heated either resistively or with an electron beam in high vacuum which causes it to evaporate. The evaporated material is collected on a substrate thus forming a thin film.

CVD has been used in many studies to prepare photocatalytic TiO_2 thin films.[115–118] Typically, a decomposition CVD reaction is used where a titanium alkoxide vapor is led in a controlled manner over the substrate at a temperature where the titanium precursor molecules decompose leading to TiO_2 growth.[116,117] Plasma enhanced CVD (PECVD) has been used to deposit photocatalytic TiO_2 thin films using $Ti(iOPr)_4$ and O_2 plasma.[118] A halide precursor, $TiCl_4$, together with ethyl acetate as the oxygen source has also been used in the CVD of photocatalytic TiO_2 thin films.[115]

1.7 Spray pyrolysis Deposition of TiO_2 Thin films

Among the above mentioned methods for depositing thin films, sol-gel coating is the most cost effective and simple to use. The two mentioned sol-gel techniques, dip and spin coating require repeated dipping/spinning and heat treatment. Spray pyrolysis deposition (SPD) technique is a low cost, easy to manipulate and an easily implementable technique suitable for large surface area coating in a single step. The synthesis of TiO_2 thin films by spray pyrolysis deposition technique have been reported in the literature.[119,120] The spray pyrolysis process consists of atomization of the precursor solution containing the precursor, and transport of the resulting aerosols towards the hot substrate by means of a gas stream.[121,122] Within the hot zone above the substrate, the precursors undergo decomposition in the presence of oxygen resulting in the formation of the oxide films on the substrate by surface reaction.[123] The temperature of the substrate influences the parameters: aerosol transport towards the substrate, solvent evaporation, possibility of the droplets impacting the surface and the dynamics of their spreading and most importantly the mechanistic path way involved in decomposition.[121,124] Therefore, the substrate temperature plays a major role in defining the morphology, composition and adherence of the deposited film. The solvents with lower density and surface tension (such as the alcohol based ones) enable creation of droplets of smaller size. The solvents with lower boiling point vaporize easily and this can have a major consequence for achieving pyrolytic decomposition.[125,126] Highly soluble precursors are generally preferred, and volatile molecules are required as co-product for accelerating pyrolysis based decomposition [126,127]. In most cases, the chemical spray pyrolysis process uses metallo-organic compounds in non-aqueous solvents as precursor.[127] The deposition of films by spray pyrolysis of an aqueous solution has also been reported in literature.[128] Ultrasonic spray pyrolysis deposition technique is akin to a open atmospheric chemical vapor deposition system hence, it is a perfect tool for the preparation of different kinds of undoped and doped TiO_2 films and nanostructures for coating and photocatalytic study in large surface area, in comparison to other physical methods of deposition of thin films like magnetron sputtering, pulsed laser deposition, electron beam evaporation, activated reactive vapor deposition etc. To conclude, anatase TiO_2 is the metastable polymorph of TiO_2. It has always remained a primary concern for the researchers to synthesize single phase anatase TiO_2 and optimise its photo responsive properties. In addition, the wide band gap of anatase has also led the researchers to do band gap engineering by various methods with various dopants such as metals, non-metals, oxygen vacancies etc. Hence, this thesis is primarily focused on synthesis and studying the properties of N-doped and oxygen deficient anatase TiO_2.

1.8 Overview of the thesis

The thesis spans over five chapters. The content of each chapter is described below in brief. Chapter 1 briefly introduces the general properties of TiO_2, necessity of doping, effect of doping with nitrogen, need for studying the oxygen vacancies in the matrix and various methods of introducing oxygen vacancies.

Chapter 2 describes various experimental methods used for synthesizing and characterising N-doped and oxygen deficient anatase thin films. The synthsizing tool includes a custom built spray pyrolysis unit used for synthesis of thin films. In addition, basic principles of various characterising tools such as GIXRD (Grazing Incidence X-ray Diffractometer (Bruker D8 Discover) used for crystallographic measurements, FESEM (Field Emission Scanning Electron Microscope of Carl Zeiss make) used for studying the microstructure, Contact angle set-up used for studying water contact angle, UV-Vis spectrometer used for studying the optical properties, XPS(X-ray Photoelectron Spectrometer)used for studying chemical nature and position of the dopant, XAS (X-ray absorption Spectrometer; Indus-II) used for pinpointing the dopant position and understanding electronic transitions have been briefly discussed. This chapter also briefly discusses the theoretical background behind the X-ray absorption spectroscopy .

Chapter 3 focuses on the synthesis and characterisation of N-doped Anatase TiO_2 thin films. This chapter emphasizes on the optical property, chemical and bonding nature of the nitrogen dopant using XPS and X-ray Absorption studies(XAS) (Indus-2 synchrotron source). This chapter discusses the use of XAS to pinpoint the exact location of nitrogen dopant (Interstitial or substitutional) in TiO_2 matrix.

Chapter 4 describes two types of synthetic methods adopted for deliberate insertion of oxygen vacancies in TiO_2 matrix, characterisation of the films by using GIXRD, FESEM and it's X-ray absorption studies to conclude the insertion of oxygen vacancies in the matrix.

Chapter 5 details the contact angle studies of the N-doped TiO_2 and oxygen deficient TiO_2. The kinetics of the change in contact angle upon photo irradiation and under dark condition is also elucidated in this chapter.

Chapter 6 summarizes the major findings of the studies carried out on spray pyrolysis synthesized anatase TiO_2 and the directions for future work.

Bibliography

[1] Hagfeldt, A. and Gratzel, M. Light-Induced Redox Reactions in Nanocrystalline Systems. *Chem. Rev.* **1995**, *95*, 49.

[2] Hoffmann, M. R.; Martin, S. T.; Choi, W.; Bahnemann, D. W. Environmental Applications of Semiconductor Photocatalysis. *Chem. Rev.* **1995**, *95*, 69.

[3] Linsebigler, A. L.; Lu, G.; Yates, J. T.Photocatalysis on TiO_2 Surfaces: Principles, Mechanisms, and Selected Results. *Chem. ReV.* **1995**, *95*, 735.

[4] Chen X.; Mao, S. S. Titanium Dioxide Nanomaterials: Synthesis, Properties, Modifications, and Applications. *Chem. Rev.* **2007**, *107*, 2891.

[5] Barringer E A and Bowen H K High-Purity, Monodisperse TiO_z Powders by Hydrolysis of Titanium Tetraethoxide. 1. Synthesis and Physical Properties. *Langmuir.* **1985**, *1*, 420.

[6] Jean, J. H.; Ring, T. A. Nucleation and Growth of Monosized TiO_2 Powders from Alcohol Solution. *Langmuir*, **1986**, *2*, 251.

[7] Look, J-L.; Zukoski, C. F. Alkoxide-Derived Titania Particles: Use of Electrolytes to Control Size and Agglomeration levels. *J. Am. Ceram. Soc.* **1992**, *75*, 1587.

[8] Landmann,M. ; Rauls, E. ; Schmidt, W. G. The Electronic Structure and Optical Response of Rutile, Anatase and Brookite TiO_2. *J. Phys.: Condens. Matter.* **2012**, *24*, 195503 (6pp).

[9] Brus, L. E. Electron-electron and electron-hole Interactions in Small Semiconductor Crystallites: The Size Dependence of the Lowest Excited Electronic State. *The Journal of Chemical Physics.* **1984**, *80 (9)*, 4403.

[10] Efros, A. I. L.; Efros, A. L. Interband Absorption of Light in a Semiconductor Sphere. *Sov. Phys. Semicond.* **1982**, *16*, 772.

[11] Zhang, H.; Banfield, J. Understanding Polymorphic Phase Transformation Behavior during Growth of Nanocrystalline Aggregates: Insights from TiO_2. *J. Phys. Chem.B.* **2000**, *104*, 3481.

[12] Naicker, P. K.; Cummings, P. T.; Zhang, H.; Banfield, J. F. Characterization of Titanium Dioxide Nanoparticles Using Molecular Dynamics Simulations. *J. Phys. Chem. B.* **2005**, *109*, 15243.

[13] Zhang, H; Banfield J. Thermodynamic Analysis of Phase Stability of Nanocrystalline Titania. *J. Mater. Chem.* **1998**, *8*, 2073.

[14] Navrotsky A. Energetics of Nanoparticle Oxides: Interplay between Surface Energy and Polymorphism. *Geochem. Trans.* **2003**, *4*, 34.

[15] Cheng, H.; Ma, J.; Zhao, Z.; Qi, L. Hydrothermal Preparation of Uniform Nanosize Rutile and Anatase Particles. *Chem. Mater.* **1995**, *7*, 663.

[16] Yanagisawa, K.; Ovenstone, J. Crystallization of Anatase from Amorphous Titania Using the Hydrothermal Technique: Effects of Starting Material and Temperature. *J. Phys. Chem.B.* **1999**, *103*, 7781.

[17] Li, J-G.; Ishigaki, T.; Sun, X. Anatase, Brookite, and Rutile Nanocrystals via Redox Reactions under Mild Hydrothermal Conditions: Phase-Selective Synthesis and Physicochemical Properties. *J. Phys. Chem. C.* **2007**, *111*, 4969.

[18] Aruna, S. T.; Tirosh, S.; Zaban, A. Nanosize Rutile Titania Particle Synthesis via Hydrothermal Method without Mineralizers. *J. Mater. Chem.* **2000**, *10*, 2388.

[19] Reyes-Coronado,D.; Rodrıguez-Gattorno, G.; Espinosa-Pesqueira, M. E.; Cab, C.; Coss,R de.; Oskam, G. Phase-pure TiO_2 Nanoparticles: Anatase, Brookite and Rutile. *Nanotechnology.* **2008**, *19*, 145605.

[20] Rafieian,D. ; Ogieglo, W.; Savenije, T.; Lammertink, R. G. H. Controlled Formation of Anatase and Rutile TiO_2 Thin Films by Reactive Magnetron Sputtering. *AIP Advances.* **2015**, *5*, 097168.

[21] Zhang, J.; Zhou, P.; Liu, J.; Yu, J. New Understanding of the Difference of Photocatalytic Activity among Anatase, Rutile and Brookite TiO_2. *Phys. Chem. Chem. Phys.* **2014**, *16*, 20382.

[22] Xu, M.; Gao, Y.; Moreno, E.M.; Kunst, M.; Muhler, M.; Wang, Y.; Idriss, H. and Woll, C. Photocatalytic Activity of Bulk TiO_2 Anatase and Rutile Single Crystals using Infrared Absorption Spectroscopy. *Phys. Rev. Lett.* **2011**, *106*, 138302.

[23] Tang, H.; Levy, F.; Berger, H.; Schmid, P. E. Urbach Tail of Anatase TiO_2. *Physical Review B.* **1995**, *52(11)*,7771.

[24] Mo, S.; Ching, W. Electronic and Optical Properties of Three Phases of Titanium Dioxide: Rutile, Anatase, and Brookite. *Phys. Rev. B.* **1995**, *51*, 13023.

[25] Maruska, H.P.; Ghosh, A.K. Photocatalytic Decomposition of Water at Semiconductor Electrodes. *Solar Energy.* **1978**, *20*, 443.

[26] Tanaka, K.; Capule,M. F. V. ; Hasinaga, T. Effect of Crystallinity of TiO_2 on its Photocatalytic Action. *Chem. Phys. Lett.* **1991**, *187*, 73.

[27] Gerischer, H. ; Heller, A.J. Photocatalytic Oxidation of Organic Molecules at TiO_2 Particles by Sunlight in Aerated Water. *Electrochem. Soc.* **1992**, *139*, 113.

[28] Bickley, R.I.; Gonzales-Carreno, T.; Lee, J.L.; Palmisano, L. ; Tilley, R.J.D. A Structural Investigation of Titanium Dioxide Photocatalysts. J. *Solid State Chem.* **1991**, *92*, 178.

[29] Mills, A.; LeHunte, S. An overview of Semiconductor Photocatalysis. *J. Photochem. Photobiol. A.* **1997**, *108*, 1.

[30] Fujishima, A.; Zhang, X. ; Tryk, D.A. TiO_2 Photocatalysis and related Surface Phenomena. *Surf. Sci. Rep.* **2008**, *63*, 515.

[31] Nguyen, N. T.; Zhu, G.; Chua, Y. C.; Phan, V. N.; Tan, S. H. Magneto-wetting and Sliding Motion of a Sessile Ferrofluid Droplet in the Presence of a Permanent Magnet. *Langmuir*, **2010**, *26*, 12553.

[32] Zhou, Q.; Ristenpart, W. D.; Stroeve, P. Magnetically Induced Decrease in Droplet Contact Angle on Nanostructured Surfaces. *Langmuir* **2011**, *27*, 11747.

[33] Chen, L.; Bonaccurso, E. Electrowetting From Statics to Dynamics. *Adv. Colloid Interface Sci.* **2014**, *210*, 2.

[34] de Gennes, P. G. Wetting: Statics and Dynamics. *Rev. Mod. Phys.* **1985**, *57*, 827.

[35] de Gennes, P.-G.; Brochard-Wyart, F.; Quere, D. Capillarity and Wetting Phenomena: Drops, Bubbles, Pearls, Waves; 1st ed.; *Springer Science: New York*, NY, USA, **2010**.

[36] Lee, D.; Rubner, M. F.; Cohen, R. E. All-Nanoparticle Thin-Film Coatings. *Nano Lett.* **2006**, *6*, 2305.

[37] Dettre, R. H.; Johnson Jr., R. E. Contact Angle Hysteresis. II. Contact Angle Measurements on Rough Surfaces. *Adv. Chem. Ser.* **1964**, *43*, 136.

[38] Marmur, A. The Lotus Effect: Superhydrophobicity and Metastability. *Langmuir* **2004**, *20*, 3517.

[39] Liu, H.; Wang, C.; Zou, S.; Wei, Z.; Tong, Z. Simple, Reversible Emulsion System Switched by pH on the Basis of Chitosan Without Any Hydrophobic Modification. *Langmuir* **2012**, *28*, 11017.

[40] Eggers, J.; Stone, H. A. Characteristic Lengths at Moving Contact Lines for a Perfectly Wetting Fluid: The Influence of Speed on the Dynamic Contact Angle. *J. Fluid Mech.* **2004**, *505*, 309.

[41] Puah, L. S.; Sedev, R.; Fornasiero, D.; Ralston, J.; Blake, T. Influence of Surface Charge on Wetting Kinetics. *Langmuir.* **2010**, *26*, 17218.

[42] Ichimura, K. Light-Driven Motion of Liquids on a Photoresponsive Surface. *Science.* **2000**, *288*, 1624.

[43] Wang, J.; Mao, B.; Gole, J. L.; Burda, C. Visible Light Driven Reversible and Switchable Hydrophobic to Hydrophilic Nitrogen-Doped Titania Surfaces: Correlation with Photocatalysis. *Nanoscale.* **2010**, *2*, 2257.

[44] Wang, R.; Hashimoto, K.; Fujishima, A. Light-Induced Amphiphilic Surfaces. *Nature.* **1997**, *388*, 431.

[45] Fujishima, A.; Honda, K. Electrochemical Photolysis of Water at a Semiconductor Electrode. *Nature.* **1972**, *238*, 37.

[46] Serpone, N.; Pelizzetti, E. Photocatalysis: *Fundamentals and Applications; Wiley: New York*, **1989**.

[47] Linsebigler, A. L.; Lu, G.; Yates, J. T. Photocatalysis on TiO_2 Surfaces: Principles, Mechanisms, and Selected Results. *Chem. ReV.* **1995**, *95*, 735.

[48] Burda, C.; Lou, Y.; Chen, X.; Samia, A. C. S.;Stout, J.; Gole, J. L. Enhanced Nitrogen Doping in TiO_2 Nanoparticles. *Nano Lett.* **2003**, *3*, 1049.

[49] Asahi, R.; Morikawa, T.; Ohwaki, T.; Aoki, K.; Taga, Y. Visible Light Photocatalysis in Nitrogen Doped Titanium Oxides. *Science.* **2001**, *293*, 269.

[50] Irie, H.; Wanatabe, Y.; Hashimoto, K. Nitrogen-Concentration Dependence on Photocatalytic Activity of $TiO_{2-x}N_x$ Powders. *J. Phys. Chem. B.* **2003**, *107*, 5483.

[51] Asahi, R.; Taga, Y.; Mannstadt, W.; Freeman, A. Electronic and Optical Properties of Anatase TiO_2 *J. Phys. ReV. B.* **2000**, *61*, 7459.

[52] Wu, Z. Y.; Ouvrared, G.; Gressier, P.; Natoli, C. R. Ti and O K edges for Titanium Oxides by Multiple Scattering Calculations: Comparison to XAS and EELS spectra. *Phys. ReV. B.* **1997**, *55*, 10382.

[53] Brydson, R.; Sauer, H.; Engel, W.; Thomas, J. M.; Zeitler, E.; Kosugi,N.; Kuroda, H. Electron Energy Loss and X-ray Absorption Spectroscopy of Rutile and Anatase: a Test of Structural Sensitivity. *J. Phys.: Condens. Matter.* **1989**, *1*, 797.

[54] Choi, H. C.; Ahn, H. J.; Jung, Y. M.; Lee, M. K.; Shin, H. J.; Kim,S. B.; Sung, Y. E. Characterization of the Structures of Size-Selected TiO_2 Nanoparticles Using X-ray Absorption Spectroscopy. *Appl. Spectrosc.* **2004**, *58*, 598.

[55] Evans, J.E.; Springer, K.W.; Zhang, J.Z. Femtosecond Studies of Interparticle Electron Transfer in a Coupled CdS-TiO_2 colloidal system. *J. Chem. Phys.* **1994**, *101*, 6222.

[56] Vinodgopal, K.; Kamat, P.V. Enhanced Rates of Photocatalytic Degradation of an Azo Dye Using SnO_2/TiO_2 Coupled Semiconductor Thin Films. *Environ. Sci. Technol.* **1995**, *29*, 841.

[57] Amiridis, M.D. ; Solar, J.P. Selective Catalytic Reduction of Nitric Oxide by Ammonia over V_2O_5/TiO_2 , $V_2O_5/TiO_2/SiO_2$, and V_2O_5- WO_3/TiO_2 Catalysts: Effect of Vanadia Content on the Activation Energy *Ind. Eng. Chem. Res.* **1996**, *35*, 978.

[58] Ho, W.K.; Yu, J.C.; Lin, J.; Yu, J.G.; Li, P.S. Preparation and Photocatalytic Behavior of MoS_2 and WS_2 Nanocluster Sensitized TiO_2. *Langmuir.* **2004**, *20*, 5865.

[59] Wang, C.; Bahnemann, D. W.; Dohrmann, J. K. A Novel Preparation of Iron Doped TiO_2 Nanoparticles with Enhanced Photocatalytic Activity. *Chem. Commun.* **2000**, *16*, 1539.

[60] Wang, Y.; Hao, Y.; Cheng, H.; Ma, H.; Xu, B.; Li, W.; Cai, S. The Photoelectrochemistry of Transition Metal Ion Doped TiO_2 Nanocrystalline Electrodes and Higher Solar Cell Conversion Efficiency based on Zn^{2+}-doped TiO_2 electrode. *J. Mater. Sci.* **1999**, *34*, 2773.

[61] Coloma, F.; Marquez, F.; Rochester, C. H.; Anderson, J. A. Determination of the Nature and Reactivity of Copper Sites in Cu-TiO_2 Catalysts. *Phys. Chem. Chem. Phys.* **2000**, *2*, 5320.

[62] Umebayashi, T.; Yamaki, T.; Itoh, H.; Asai, K. Analysis of Electronic Structures of 3*d* Transition Metal Doped TiO_2 Based on Band Calculations. *J. Phys. Chem. Solids.* **2002**, *63*, 1909.

[63] Choi,W.; Termin, A.; Hoffmann, M.R. The Role of Metal Ion Dopants in Quantum-Sized TiO_2: Correlation between Photoreactivity and Charge Carrier Recombination Dynamics. *J. Phys. Chem.* **1994**, *98*, 13669.

[64] Wang, Y.; Cheng, H.; Hao, Y.; Ma, J.; Li, W.; Cai, S. Photoelectrochemical Properties of Metal Ion Doped TiO_2 Nanocrystalline Electrodes. *Thin Solid Films.* **1999**, *349*, 120.

[65] Yamashita, H.; Honda, M.; Harada, M.; Ichihashi, Y.; Anpo, M.; Hirao, T.; Itoh, N.; Iwamoto, N. Preparation of Titanium Oxide Photocatalysts Anchored on Porous Silica Glass by a Metal Ion-Implanttion Method and Their Photocatalytic Reactivities for the Degradation of 2-Propanol Diluted in Water. *J. Phys. Chem. B.* **1998**, *102*, 10707.

[66] Yu, J. C.; Yu, J. G.; Ho, W. K.; Jiang, Z. T.; Zhang, L. Z. Effects of F- Doping on the Photocatalytic Activity and Microstructures of Nanocrystalline TiO_2 Powders. *Chem. Mater.* **2002**, *14*, 3808.

[67] Khan, S. U. M.; Al-Shahry, M.; Ingler, W. B., Jr. Efficient Photochemical Water Splitting by a Chemically Modified N-TiO_2. *Science.* **2002**, *297*, 2243.

[68] Nakamura, I.; Negishi, N.; Kutsuna,S.; Ihara, T.; Sugihara, S.; Takeuchi,K. Role of Oxygen Vacancy in the Plasma-treated TiO_2 Photocatalyst with Visible Light Activity for NO removal. *J. Mol. Catal. A-Chem.* **2000**, *161*, 205.

[69] Justicia,I.; Ordejón,P.; Canto,G.; Mozos,J.L.; Fraxedas, J.; Battiston,G.A.; Gerbasi, R.; Figueras, A. Designed Self-Doped Titanium Oxide Thin Films for Efficient Visible-Light Photocatalysis. *Adv. Mater.* **2002**, *14*, 1399.

[70] Justicia,I.; Garcia,G.; Battiston,G.A.; Gerbasi,R.; Ager,F.; Guerra,M.; Caixach,J.; Pardo,J.A.; Rivera, J.; Figueras, A.Photocatalysis in the Visible Range

of Sub-stoichiometric Anatase Films Prepared by MOCVD. *Electrochimica Acta.* **2005**, 50, 4605.

[71] Kuznetsov,V.N.; Serpone, N. On the Origin of the Spectral Bands in the Visible Absorption Spectra of Visible-Light-Active TiO_2 Specimens Analysis and Assignments. *J. Phys. Chem. C.* **2009**, *113*, 15110.

[72] Di Valentin, C.; Finazzi, E.; Pacchioni, G.; Selloni, A.; Livraghi, S.; Paganini, M. C.; Giamello, E. N-doped TiO_2 : Theory and experiment. *Chemical Physics.* **2007**, *339*, 44.

[73] Sato, S. Photocatalytic Activity of NO_x-doped TiO_2 in the visible light region. *Chem. Phys. Lett.* **1986**, *123*, 126.

[74] Sakthivel, S.; Janczarek, M.; Kisch, H. Visible Light Activity and Photoelectrochemical Properties of Nitrogen-Doped TiO_2. *J. Phys. Chem. B.* **2004**, *108*, 19384.

[75] Diwald, O.; Thompson, T.L.; Zubkov, T.; Goralski, E.G.; Walck, S.D.; Yates Jr. J.T. Photochemical Activity of Nitrogen-Doped Rutile TiO_2 (110) in Visible Light. *J. Phys. Chem. B.* **2004**, *108*, 6004.

[76] Miyauchi, M.; Ikezawa, A.; Tobimatsu, H.; Irie, H.; Hashimoto, K. Zeta potential and photocatalytic activity of nitrogen doped TiO_2 thin films. *Phys. Chem. Chem. Phys.* **2004**, *6*, 865.

[77] Gole, J.L.; Stout, J.D.; Burda, C.; Lou, Y.; Chen, X. Highly Efficient Formation of Visible Light Tunable $TiO_{2-x}N_x$ Photocatalysts and Their Transformation at the Nanoscale. *J. Phys. Chem. B.* **2004**, *108*, 1230.

[78] Thompson, T.L.; Yates Jr., J.T. Surface Science Studies of the Photoactivation of TiO_2 New Photochemical Processes. *Chem. Rev.* **2006**, *106*, 4428.

[79] Yates, H.M.; Nolan, M.G.; Sheel, D.W.; Pemble, M.E. The role of Nitrogen Doping on the Development of Visible Light-induced Photocatalytic Activity in Thin TiO_2 Films Grown on Glass by Chemical Vapour Deposition. *J. Photochem. Photobiol. A.* **2006**, *179*, 213.

[80] Ni, M.; Leung, M.K.H.; Leung, D.Y.C.; Sumathy, K.; A Review and Recent Developments in Photocatalytic Water-splitting using TiO_2 for Hydrogen Production. *Renew. Sustain. Energy Rev.* **2007**, *11*, 401.

[81] Z. Lin, A. Orlov, R.M. Lambert, M.C. Payne, New Insights into the Origin of Visible Light Photocatalytic Activity of Nitrogen-Doped and Oxygen-Deficient Anatase TiO_2. *J. Phys. Chem. B.* **2005**, *109*, 20948.

[82] Sathish, M.; Viswanathan, B.; Viswanath, R.P.; Gopinath, C.S. Synthesis, Characterization, Electronic Structure, and Photocatalytic Activity of Nitrogen-Doped TiO_2 Nanocatalyst. *Chem. Mater.* **2005**, *17*, 6349.

[83] Nosaka, Y.; Matsushita, M.; Nasino, J.; Nosaka, A.Y. Nitrogen-doped Titanium Dioxide Photocatalysts for Visible Response Prepared by using Organic Compounds. *Sci. Technol. Adv. Mat.* **2005**, *6*, 143.

[84] Morikawa, T.; Asahi, R.; Ohwaki, T.; Aoki, K.; Taga, Y. Band-Gap Narrowing of Titanium Dioxide by Nitrogen Doping. *Jpn. J. Appl. Phys.* **2001**, *40*, L561.

[85] Diwald, O.; Thompson, T.L.; Goralski, E.G.; Walck, S.D.; Yates Jr., J.T. The Effect of Nitrogen Ion Implantation on the Photoactivity of TiO_2 Rutile Single Crystals. *J. Phys. Chem. B.* **2004**, *108*, 52.

[86] Batzill, M.; Morales, E.H.; Diebold, U. Influence of Nitrogen Doping on the Defect Formation and Surface Properties of TiO_2 Rutile and Anatase. *Phys. Rev. Lett.* **2006**, *96*, 026103.

[87] Ghicov, A. ; Macak, J.M.; Tsuchiya, H.; Kunze, J.; Haeublein, V.; Frey, L; Schmuki, P. Ion Implantation and Annealing for an Efficient N-Doping of TiO_2 Nanotubes. *Nano Lett.* **2006**, *6*, 1080.

[88] Mwabora, J.M.; Lindgren, T.; Avendano, E.; Jaramillo, T.F.; Lu, J.; Lindquist, S.E.; Granqvist, C.G. Structure, Composition, and Morphology of Photoelectrochemically Active $TiO_{2-x}N_x$ Thin Films Deposited by Reactive DC Magnetron Sputtering. *J. Phys. Chem. B.* **2004**, *108*, 20193.

[89] Y. Nakano, T. Morikawa, T. Ohwaki, Y. Taga, Deep-level Optical Spectroscopy Investigation of N-doped TiO_2 Films. *Appl. Phys. Lett.* **2005**, *86*, 132104.

[90] Valentin,C.D.; Pacchioni, G. ; Selloni, A. Origin of the Different Photoactivity of N-doped Anatase and Rutile TiO_2. *Phys. Rev. B.* **2007**, *70*, 085116.

[91] Chen, X.; Burda, C. Photoelectron Spectroscopic Investigation of Nitrogen-Doped Titania Nanoparticles. *J. Phys. Chem. B.* **2004**, *108*, 15446.

[92] Di Valentin, C.; Pacchioni, G.; Selloni, A.; Livraghi, S.; Giamello, E. Characterization of Paramagnetic Species in N-Doped TiO_2 Powders by EPR Spectroscopy and DFT Calculations. *J. Phys. Chem. B.* **2005**, *109*, 11414.

[93] Mrowetz,M.; Balcerski,W.; Colussi,A.J.; Hoffmann, M.R. Oxidative Power of Nitrogen-Doped TiO_2 Photocatalysts under Visible Illumination. *J. Phys. Chem. B.* **2004**, *108*, 17269.

[94] Yates,H.M.; Nolan,M.G.; Sheel,D.W.; Pemble, M.E. The Role of Nitrogen Doping on the Development of Visible Light-Induced Photocatalytic Activity in Thin TiO_2 Films Grown on Glass by Chemical Vapour Deposition. *J. Photochem. Photobiol. A.* **2006**, 179, 213.

[95] Sakatani, Y.; Nunoshige, J.; Ando, H.; Okusako, K.; Koike, H.; Takata, T.; Kondo, J.N.; Hara, M.; Domen, K. Photocatalytic Decomposition of Acetalde-

hyde under Visible Light Irradiation over La^{3+} and N Co-doped TiO_2. *Chem. Lett.* **2003**, *32*, 1156.

[96] Bharti, B.; Kumar, S.; Lee, H.; Kumar, R. Formation of Oxygen Vacancies and Ti^{3+} State in TiO_2 Thin Film and Enhanced Optical Properties by Air Plasma Treatment. *Scientific Reports.* **2016**, *6*, Article number: 32355

[97] Liu, Y.; Wang, J.; Yang, P.; Matras-Postolek, K. Self-modification of TiO_2 one-Dimensional Nano-materials by Ti^{3+} and Oxygen Vacancy using Ti_2O_3 as Precursor. *RSC Adv.* **2015**, *5*, 61657.

[98] Kuznetsov, V.N.; Serpone, N. On the Origin of the Spectral Bands in the Visible Absorption Spectra of Visible Light Active TiO_2 Specimens Analysis and Assignments. *J. Phys. Chem. C.* **2009**, *113*, 15110.

[99] Lu, X. et al.Hydrogenated TiO_2 Nanotube Arrays for Supercapacitors. *Nano Lett.* **2012**, *12*, 1690.

[100] Konstantakou, M. et al.Influence of Fluorine Plasma Treatment of TiO_2 Films on the Behavior of Dye Solar Cells Employing the Co (II)/(III) Redox Couple. *J. Phys. Chem. C.* **2014**, *118*, 16760.

[101] Lu, H. et al.Safe and Facile Hydrogenation of Commercial Degussa P25 at room Temperature with Enhanced Photocatalytic Activity. *RSC Adv.* **2014**, *4*, 1128.

[102] Zheng, Z.; Huang, B.; Lu, J.; Wang, Z.; Qin, X.; Zhang, X.; Dai, Y.; Whangbo, M. H. Hydrogenated Titania: Synergy of Surface Modification and Morphology Improvement for Enhanced Photocatalytic Activity. *Chem. Commun.* **2012**, *48*, 5733.

[103] Heo, C. H., Lee, S. B.; Boo, J. H. Deposition of TiO_2 thin films using RF magnetron sputtering method and study of their surface characteristics. *Thin Solid Films.* **2005**, *475*, 183.

[104] Li, Y.; Jang, B. W. L. Investigation of Calcination and O_2 Plasma Treatment Effects on TiO_2 Supported Palladium Catalysts. *Ind. Eng. Chem. Res.* **2010**, *49*, 8433.

[105] Yamada, K. et al.Photocatalytic Activity of TiO_2 Thin Films Doped with Nitrogen using a Cathodic Magnetron Plasma Treatment. *Thin Solid Films.* **2008**, *516*,7560.

[106] Guillard, C.; Beaugiraud, B.; Dutriez, C.; Herrmann, J.M.;Jaffrezic, H.; Jaffrezic-Renault, N.; Lacroix, M. Physicochemical Properties and Photocatalytic Activities of TiO_2 Films Prepared by Sol-gel Methods. *Appl. Catal. B.* **2002**, *39*, 331.

[107] Chen, Y.J.; Dionysiou, D.D. Correlation of Structural Properties and Film Thickness to Photocatalytic Activity of Thick TiO_2 Films Coated on Stainless Steel. *Appl. Catal. B.* **2006**, *69*, 24.

[108] H. Choi, E. Stathatos and D.D. Dionysiou, Sol–gel Preparation of Mesoporous Photocatalytic TiO_2 Films and TiO_2/Al_2O_3 Composite Membranes for Environmental Applications. *Appl. Catal. B.* **2006**, *63*, 60.

[109] Tao, J.C.; Shen, Y.; Gu, F.; Zhu, J.Z.; Zhang, J.C. Synthesis and Characterization of Mesoporous Titania Particles and Thin Films. *J. Mater. Sci. Technol.* **2007**, *23*, 513.

[110] Y. Paz and A. Heller, Photo-oxidatively Self-cleaning Transparent Titanium Dioxide Films on Soda lime Glass: the Deleterious Effect of Sodium Contamination and its Prevention. *J. Mater. Res.* **1997**, *12*, 2759.

[111] Yu, J.; Zhao, X.; Zhao, Q. Effect of Surface Structure on Photocatalytic Activity of TiO_2 Thin Films Prepared by Sol-Gel Method. *Thin Solid Films.* **2000**, *379*, 7.

[112] Ghamsari, M. S.; Bahramian, A.R. High Transparent Sol-Gel Derived Nanostructured TiO_2 *Thin Film. Materials Letters.* **2008**, *62*, 361.

[113] Imai, H.; Matsuta, M.; Shimizu, K.; Hirashima, H.; Negishi, N. Morphology Transcription with TiO_2 using Chemical solution Growth and its Application for Photocatalysts. *Solid State Ionics.* **2002**, *151*, 183.

[114] Chen, Q.; Qian, Y.;Chen, Z.; Wu, W.; Chen, Z.; Zhou, G.; Zhang, Y. Hydrothermal Epitaxy of highly Oriented TiO_2 Thin Films on Silicon. *Appl. Phys. Lett.* **1995**, *66*, 1608.

[115] A. Mills, N. Elliott, I.P. Parkin, S.A. O'Neill and R.J. Clark, Novel TiO_2 CVD films for Semiconductor Photocatalysis. *J. Photochem. Photobiol: A.* **2002**, *151*, 171.

[116] Bessergenev, V.G.; Khmelinskii, I.V.; Pereira, R.J.F.; Krisuk, V.V.; Turgambaeva, A.E.; Igumenov, I.K. Preparation of TiO_2 Films by CVD method and its Electrical, Structural and Optical Properties. *Vacuum.* **2002**, *64*, 275.

[117] Bessergenev, V.G.; Pereira, R.J.F.; Mateus, M.C.; Khmelinskii, I.V.; Vasconcelos, D.A.;Nicula, R.;Burkel, E.; do Rego,,A.M. B.; Saprykin, A.I. Study of Physical and Photocatalytic Properties of Titanium Dioxide Thin Films Prepared from Complex Precursors by Chemical Vapour Deposition. *Thin Solid Films.* **2006**, *503*, 29.

[118] Guillard, C.;Debayle, D.; Gagnaire, A.; Jaffrezic, H.; Herrmann, J.M. Physical Properties and Photocatalytic Efficiencies of TiO_2 Films Prepared by PECVD and Sol-Gel Methods. *Mater. Res. Bull.* **2004**, *39*, 1445.

[119] More, A.M.; Gunjkar, J.L.; Lokhande, C.D.; Mane, R.S.; Han, S.H. Systematic interconnected Web-like Architecture Growth of Sprayed TiO_2 films. *Micron.* **2007**, *38*, 500.

[120] Conde-Gallardo, A.; Guerrero, M.; Castillo, N.; Soto, A.B.; Fragoso, R.; CabanasMoreno, J.G. *Thin Solid Films.* **2005**, *473*, 68.

[121] Perednis, D.; Gauckler, L. Thin Film Deposition Using Spray Pyrolysis. *J. Electroceramics.* **2005**, *14*, 103.

[122] Roger, C.; Corbitt,T.; Xu,C.; Zeng, D.; Powell, Q.; Chandler, C.D.; Nyman, M.; Hampden-Smith, M.J.; Kodas, T.T. Principles of Molecular Precursor Selection for Aerosol Synthesis of Materials. *Nanostruct. Mater.* **1994**, *4*, 529.

[123] Schwartz, R.W.; Schneller, T.; Waser, R. Chemical Solution Deposition of Electronic Oxide Films. *Comptes Rendus Chim.* **2004**, *7*, 433.

[124] Bouzidi, A.; Benramdane, N.; Derraz, H.T.; Mathieu, C.; Khelifa, B.; Desfeux, R. Effect of Substrate Temperature on the Structural and Optical Properties of MoO_3 Thin Films Prepared by Spray Pyrolysis Technique. *Mater. Sci. Eng. B.* **2003**, *97*, 5.

[125] Patil, P.S. Versatility of Chemical Spray Pyrolysis Technique. *Mater. Chem. Phys.* **1999**, *59*, 185.

[126] Wang, W.N.; Purwanto, A.; Lenggoro, I. W.; Okuyama, K.; Chang, H.; Jang,H. D. Investigation on the Correlations between Droplet and Particle Size Distribution in Ultrasonic Spray Pyrolysis. *Ind. Eng. Chem. Res.* **2008**, *47*, 1650.

[127] Castaneda, L.; Alonso, J.C.; Ortiz, A.; Andrade, E.; Saniger, J.M.; Banuelos, J.G. Spray Pyrolysis Deposition and Characterization of Titanium Oxide Thin Films. *Mater. Chem. Phys.* **2002**, *77*, 938.

[128] Natarajan, C.; Fukunaga, N. ; Nogami, G. Titanium Dioxide Thin Film Deposited by Spray Pyrolysis of Aqueous Solution. *Thin solid Films.* **1998**, *322*, 6.

Chapter 2

Experimental Methods

2.1 Synthesis Techniques

This chapter elucidates the synthetic route and various characterization and analytical tools adopted to characterize and decipher the properties of thin films. Pristine Titanium dioxide and N-doped Titanium dioxide were synthesized using spray pyrolysis, which is described below in detail.

2.1.1 Spray Pyrolysis

Spray pyrolysis is a synthetic method whose principle is similar to Chemical vapour deposition(CVD). It has several advantages owing to low operational cost, operation at atmospheric pressure, rapid film growth, mass production, reproducibilty and large surface area coverage. In case of spray pyrolysis usually a liquid is used as a precursor as compared to CVD, wherein mostly a solid is used as precursor. The liquid precursor is vapourized and transported to a pre-heated substrate, where it undergoes various physico-chemical processes described herein to form a thin film. During initial days of deciphering the mechanism of spray pyrolysis, substrate temperature, initial droplet size and entrained particle size was considered as a major factors of deposition.Figure 2.1 shows the mechanism with respect to the above factors.

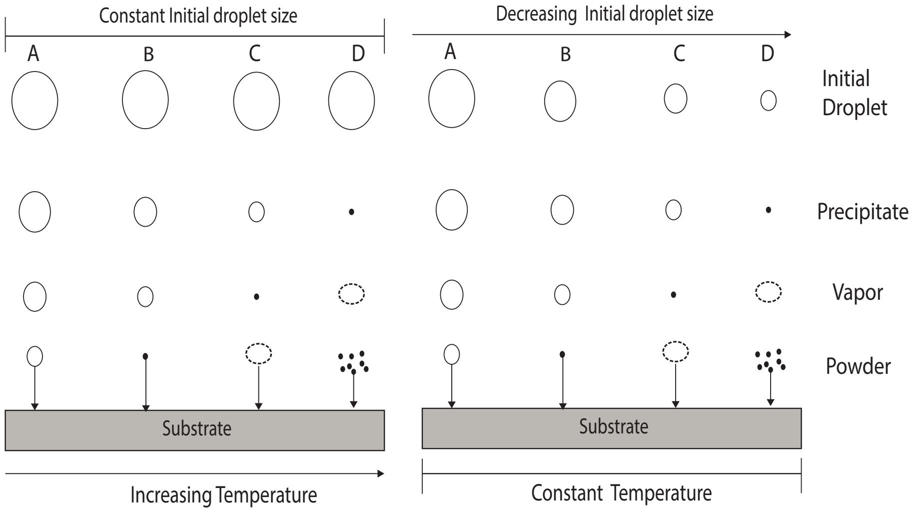

Figure 2.1 – Spray pyrolysis mechanism

The processes are described here in detail.

Process A When the initial droplet size is constant, as the temperature increases; the droplets undergo various processes before forming a film. At low temperatures, the droplets undergo evaporation even before reaching the substrate. As, it approaches the substrate it undergoes precipitation resulting in an amorphous salt, followed by decomposition. At intermediate temperature, the droplets undergo vaporization before reaching the substrate resulting in precipitation. It then sublimes and undergoes reactive decomposition at the substrate resulting in TiO_2 film formation. At high temperatures, all these above phenomena occurs well before reaching the substrate, which induces low adherence to the substrate.

Process B When the temperature Remains constant and the droplet sizes vary; The phenomena of droplet and substrate interaction follows the same trend as described above with respect to temperature. When the droplet size is sufficiently low; evaporation, precipitation, vaporization and condensation, all occur even before reaching the substrate leading to low adherence.

However, these early models did not consider the effect of cooling of the substrate by the liquid, phenomena occurring following particle impingement on the substrate, entrained particle size effects, nature of chemical bonding between thin film and substrate, crystallinity of the thin film, nanostructure and morphology of thin film and annealing effects on the thin film.To deal with the above limitations and complex situations arising out of it, the subsequent models concentrated on the explanation of whether a CVD process can take place or not during spray pyrolysis.

- The temperature of the heated substrate must be similar to the limit of stability of the salt complex, so that the precipitates are able to approach the substrate without decomposing/oxidizing on the substrate or subliming before they reach the substrate; they must sublime at the substrate.

- The particle size of the precipitates should be sufficiently small so that the relatively high surface energy component may facilitate sublimation to the vapor phase at the substrate, where condensation and strong chemisorption can occur.

If the temperature is too low, then the precursor liquid droplets or subsequent precipitates are coarse and have insufficient surface and thermal energy to allow vaporization. If the temperature is too high, then sublimation takes place at a sufficient distance away from the substrate such that oxide particles are formed away from the substrate and subsequently impinge onto the substrate and bond by weak physisorption.

In summary, for the CVD process to occur, several conditions must exist:

1. The substrate temperature must be at least and preferably similar to that of the decomposition temperature of the salt complex. (a) The substrate temperature, speed of droplet delivery, transit path length, and other experimental variables must be such that the temperature is sufficiently high to prevent impingement of entrained liquid droplets or precipitates on the substrate. (b) The substrate temperature, speed of droplet delivery, transit path length, and other experimental variables must be such that the temperature is sufficiently low to prevent sublimation of entrained precipitates before approaching the substrate.

2. The evaporation and precipitation must facilitate a precipitate particle size suitable for sublimation at the substrate, presumably being assisted by the high surface energy associated with fine particles. Since, this model incorporates both processes and outcomes, a practical use for this mechanistic model is that it can serve as a diagnostic tool for assessment of films produced by the spray pyrolysis technique. Hence, it can be concluded that, there has to be an optimum temperature and optimum droplet size, such that sublimation should take place immediately prior to reaching the substrate followed by decomposition resembling to a true CVD process.

Metal Oxide nanoparticles and films can be obtained by thermal decomposition of various inorganic or organometallic precursors. Typical starting materials include metal acetylacetonates[2], metal cupferronates[3], metal alkoxides[4], metal carbonyls[5], and metal halides[6]. These methods in general are of limited synthetic scope for metal oxide synthesis. Among these starting materials, metal acetylacetonates are particularly preferred for its low sublimation temperature, which help the precipitate to evaporate and undergo vapor decomposition at the substrate. The decomposition temperatures of metal acetyl actonates are between 300 to 400 °C. Low decomposition temperature makes it suitable candidate for spray pyrolytic syntheses.[7]

2.2 Characterization Tools

2.2.1 Grazing Incidence X-ray diffraction(GIXRD)

Grazing Incidence X-ray diffraction, originally developed by Marra et al.in 1979.[8] is typically used to characterize surface and thin films without having the effect of substrate. In conventional XRD the incident X-ray beam penetrates deep into the material, while in GIXRD, the incidence angle(θ_i) is either equal to or below the critical angle (θ_c) for total reflection. The low incidence angle make the incident beam evanescent and it penetrates only the top 100 or less into the surface. In addition to the low penetration depth,at $\theta_i \cong \theta_c$the intensity of the X-ray at the surface is 2-4 times higher than the intensities in the bulk.

The GIXRD measurements for the films towards the completion of the work reported in the thesis has been done in the classic reflection geometry, also known as Bragg-Brentano geometry. The instrument used was Bruker D8 Discover. Schematic of a typical GIXRD instrument is given in Fig 2.

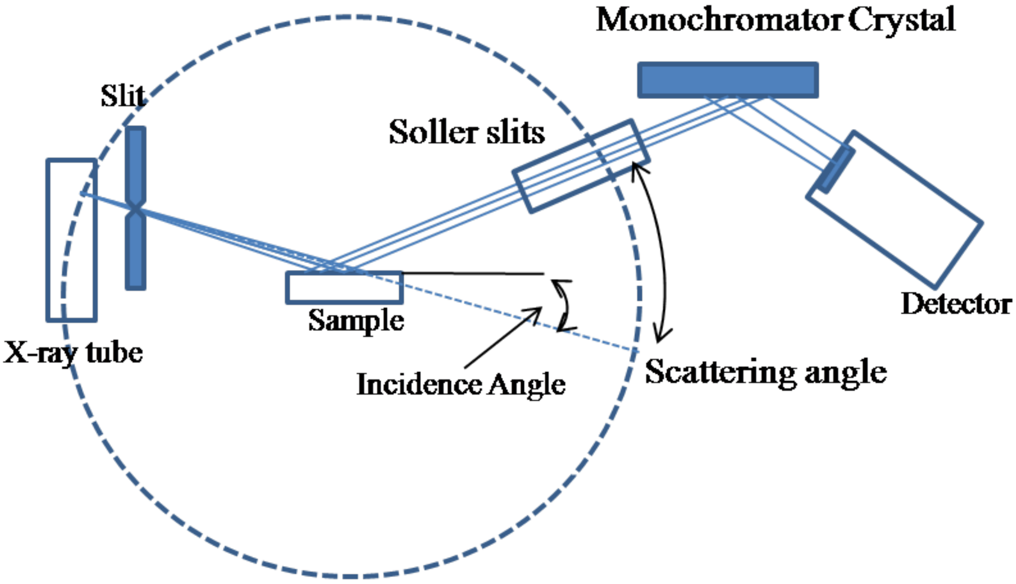

Figure 2.2 – Schematic of GIXRD instrument.

2.2.2 Field Emission Scanning Electron Microscopy(FESEM)

Scanning electron microscope is widely used for microstructural analysis with a spatial resolution of 2 nm. The SEM electron beam is a focused probe of electrons accelerated to moderately high energy and positioned onto the sample by electromagnetic fields. The SEM optical column is utilized to ensure that the incoming electrons are of similar energy and trajectory. Interaction of high energy electron beams with matter can be divided broadly into elastic and inelastic interactions. Elastically scattered electrons are the ones which get recoiled from the atomic nucleus without loosing energy at an angle equal to 90 or more. The electrons which are elastically scattered at an angle of more than 90 are known as backscattered electrons (BSE).

In principle, electrons were extracted from a sharp tip of the filament by applying very high voltages. These emitted electrons get focused by electromagnetic condenser lens to form a sharp electron beam with a narrow energy spread. A schematic representation of FESEM is illustrated in Fig 2.3.. The focused electron beam is used to raster on the material surface to get the morphology. The possible emission characteristics upon interaction of incident electron beam with matter are shown in Fig 2.4. Secondary electrons and back scattered electrons are used to analyze by corresponding detectors for obtaining morphology.[9]

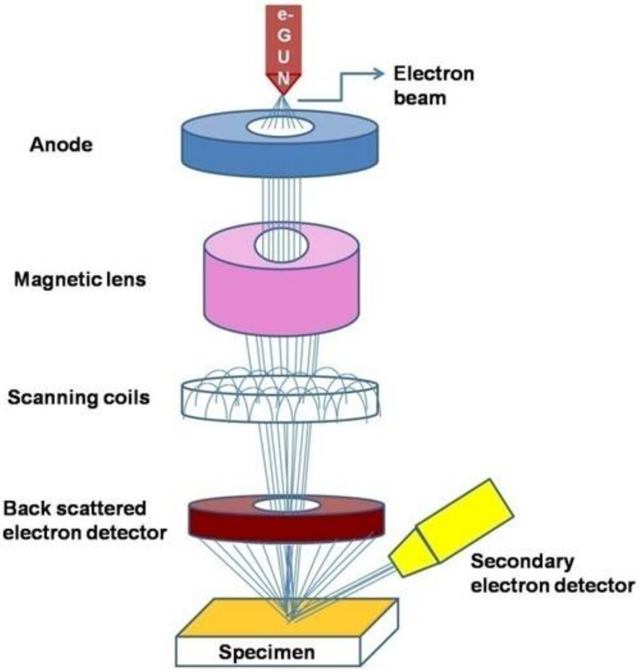

Figure 2.3 – A schematic of Field Emission Scanning Electron Microscopy (FESEM)

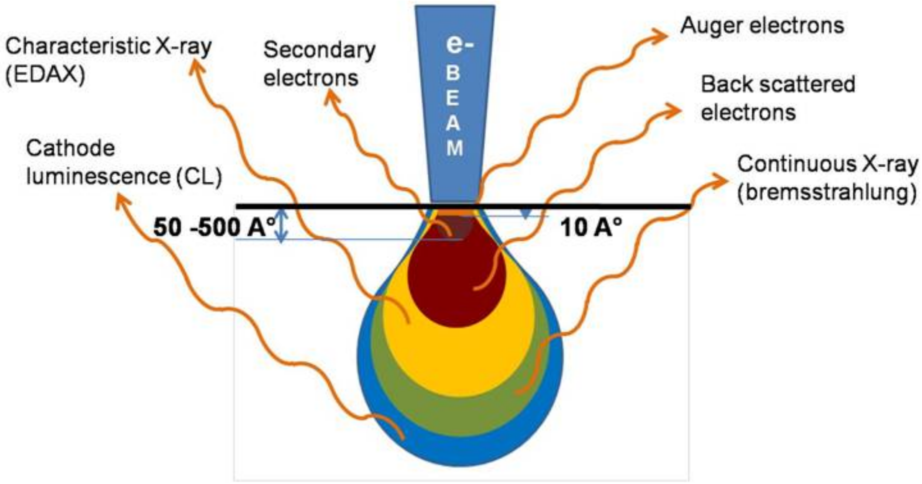

Figure 2.4 – A schematic of Field Emission Scanning Electron Microscopy (FESEM)

FESEM system consists of field emission gun, SE and BSE detectors. In this study we used FESEM (Supra 55, Carl zeiss, Germany) to obtain the morphology of the TiO_2 films.

2.3 Contact Angle Measurement

The water contact angle experiments for the films in this thesis were carried out by using a contact angle meter equipped with a CCD camera (Holmarc, HO-IAD-CAM-01, India). The contact angles were determined by analyzing the high resolution images of the water droplets on the thin films using ImageJ software.A brief overview of the theoretical aspects of contact angle studies is given in the following section.

2.4 Theoretical Background of Wetting Studies.

The ability of a liquid to wet a solid can be quantified by measuring the angle at which the liquid/vapor interface intersects the solid-liquid interfacial plane (Fig 2.5). This angle is referred to as the "contact angle" and the line where the interface contacts the solid is called the three-phase contact line. The relation between the contact angle and the surface tensions/surface energies at the three phase boundaries has been first described by Young in his famous article " An essay on the cohesion of fluids" in 1805.[10] This lead to the famous Young's equation which is the first of its kind equation to describe the relation between contact angle and surface tensions/surface energies and is given below.

$$cos\theta = \frac{\gamma_{SL} - \gamma_{SV}}{\gamma_{LV}} \tag{2.1}$$

There has been debates on whether the representation of interfacial tension/surface tension as a viable term can meaningfully describe the thermodynamics of the whole system. Many researchers have contended in favour of surface tension whereas many have negated it in favour of surface energy.[26,27] However, for the sake of simplicity and since the present study is not exactly on the thermodynamic aspect,the term interfacial energy is used in a broader sense and a simple derivation considering the minimization of free energy is given below.[28,29]

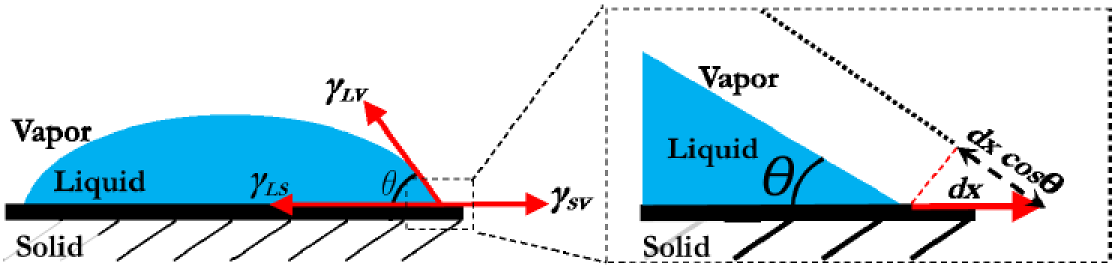

Figure 2.5 – (left) Sketch of a sessile drop on a surface. The contact angle θ is the angle between the liquid vapor interface and solid surface at the contact angle where all three phases meet. Vectors indicate the direction of the forces from interfacial tension that act on the contact line (right). When a sessile drop on a solid surface spreads an infinitesimal amount dx, the area that the drop covers increases in proportion to dx and there is a corresponding decrease in the area of the solid that was previously uncovered. In addition, the area of the liquid-air interface expands in proportion to $dxCos\theta$.

A thermodynamic derivation of the contact angle follows from minimizing the free energy. Imagine displacing the boundary of the sessile drop by an infinitesimal amount (Fig. 2.5). The change in free energy of the overall system in Fig. 2.5 is governed by the change in areas of the three types of interface, solid-liquid, solid-vapor and liquid-vapor with interfacial free energies γ_{SL}, γ_{SV} and γ_{LV}, respectively. The change in free energy per unit length of contact line in Fig. 2.5 is:

$$dG = (\gamma_{SL} - \gamma_{SV})dx + \gamma_{LV}cos(\theta)dx. \tag{2.2}$$

At equilibrium, dG must be zero giving the equation:

$$\gamma_{LV}cos(\theta) = (\gamma_{SL} - \gamma_{SV}) \tag{2.3}$$

$$cos\theta = \frac{\gamma_{SL} - \gamma_{SV}}{\gamma_{LV}} \tag{2.4}$$

This indicates that when $0^\circ \leq \theta < 90^\circ$ the free energy of the solid-vapor system must be higher than the solid-liquid system. The overall system will reach an equilibrium in which the liquid has spread and minimizes the exposed solid to lower the overall free energy. Therefore, systems with contact angles in this range are referred to as "wetting". When $90° < \theta \leq 180°$ the opposite occurs and the liquid will be repelled by the surface in order to minimize the covered surface to lower the overall energy. Systems with contact angles in this range are referred to as "non-wetting".

In the case of water, wetting and non-wetting surfaces are called hydrophilic and hydrophobic.

2.4.1 Wenzel and Cassie-Baxter Wetting

Young's equation can be applied only to a flat surface not to a rough one. Thus, several models describing the contact angle at a rough solid surface has been proposed. Wenzel proposed the first ever model for a rough surface, which is briefly discussed here. Roughness increases the total area of the solid surface that contributes to the interfacial free energy, and thus changes the contact angle. The "roughness factor" – denoted r – is defined as:

$$r = \frac{actual\ surface}{geometric\ surface} \tag{2.5}$$

The difference between these two surfaces is presented verbatim from the original article considering its importance and contribution to the field of contact angle. "Geometric surface is the surface as measured in the plane of the interface. Where perfect smoothness is an acceptable assumption, as at liquid-liquid or liquid-gas interfaces, actual surface and geometric surface are identical, but at the surface of any real solid the actual surface area will be greater than the geometric surface area because of surface roughness."[30] Hence, the contributions of solid free energies in eqn. 2.2 is increased by r, leading to:

$$cos\theta_{app} = rcos\theta_{true} \tag{2.6}$$

where θ_{app} is the expected angle on rough surfaces,θ_{true} the local angle on an equivalent smooth surface and the system will be perfectly wetting (non-wetting) if the right hand side is greater than +1 (less than -1). This equation is often referred to as the Wenzel equation for rough surfaces.[31] Since the true area will always be larger than the smooth area, r will always be greater than one. Therefore, if a smooth surface is wetting, then a rough surface of the same material will wet more readily making the apparent contact angle smaller. By the same reasoning, a surface with a contact angle above 90° will gain a higher contact angle if that surface is roughened.

Cassie Baxter extended the wenzel's analysis to porous structure, wherein the concept of air traps were shown to play a role in determining the contact angle. A brief understanding of the model is briefly discussed here.In a heterogeneous surface with different local wetting properties, the interfacial free energy is assumed to be a weighted average of different types of surface with weight ϕ_i equal to the fraction of the surface that has a local contact angle θ_i. The cosine of the apparent contact angle will just be the weighted average of the cosines for each type of surface and is given by the following equation:

$$cos\theta_{app} = \phi_1 Cos\theta_1 + \phi_2 Cos\theta_2 + \ldots, \tag{2.7}$$

which is known as the Cassie-Baxter equation.[32] A special situation involves the so-called "Lotus effect" where the surface is nanostructured in such a way that spreading water traps air in the nano-sized holes instead of filling the holes with water.[33] This trapped air has an effective contact angle of 180° making the surface superhydrophobic.

2.5 Optical and electronic measurements

2.5.1 Ultraviolet Visible Spectroscopy

Ultraviolet and visible (UV-Vis) absorption spectroscopy deals with the measurement of the attenuation of a beam of light after it passes through a sample or after reflection from a sample surface.[11] The attenuation can result from processes like absorbance, transmittance, reflectance and interference. The measurements are carried out at a single wavelength or over an extended spectral range. The UV-Vis spectral range spans approximately from 190 to 900 nm. The short wavelength limit for simple UV-Vis spectrometers is the absorption of UV wavelengths < 180 nm by the intervening atmospheric gases. The use of UV-Vis spectroscopy in materials research can be divided into two main categories: (1) quantitative measurements of an analyte in the liquid or solid phase and (2) characterization of the optical and electronic properties of a solid state material. The first category is most useful as a diagnostic tool to quantify various constituents of materials or to monitor the concentrations of reactants or products during the course of a chemical reaction. In quantitative applications, it often becomes a necessity to measure the absorbance or reflectivity at a single specified wavelength. A typical UV-Vis experimental setup is shown in the Fig 2.6.

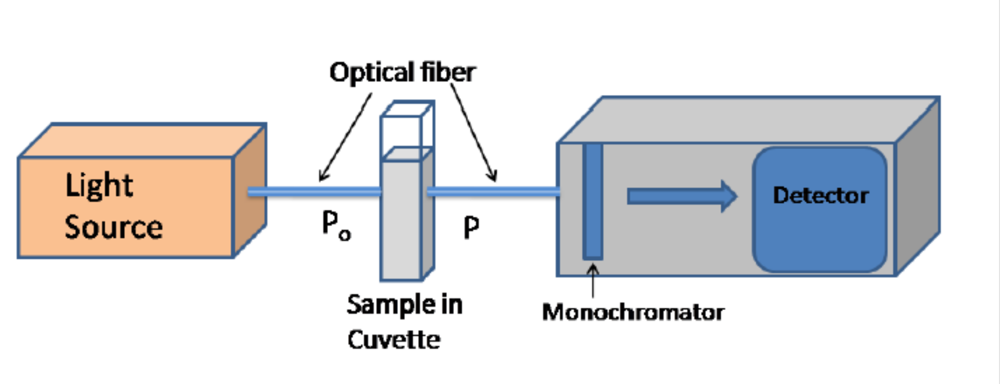

Figure 2.6 – Schematic of UV-Vis experimental set-up

For quantitative analysis, the Beer–Lambert law, which allows accurate concentration measurement of the absorbing species, is given as

$$A = \epsilon cl \tag{2.8}$$

Where A is the absorbance, ϵ the molar absorbance or absorption coefficient, c the concentration of the analyte in the solution (in mg/ml) and l is the path length of light in the sample (in cm). The relationship between absorbance A and the experimentally measured transmittance T is

$$a = -log(T) = -log\frac{P}{P_0} \tag{2.9}$$

Where P is the radiant power (radiant energy on unit area in unit time) after it passes through the sample and P_0 is the initial radiant power (schematically shown in Fig. 2.6), both T and A are unit less. However, the Beer-Lambert Law breaks down for solutions of higher concentration, yielding departure from linear behavior. In the case of solid materials, the UV-Vis spectrum can measure the band gap and identify any localized excitations or impurities. The measurements are carried out either in the transmittance or reflectance mode. In samples, light interacts with the matter by means of different processes such as reflection, refraction and diffraction, and eventually emerges out diffusively (scatters in all directions). For different transition mechanisms, it has been proved that along the sharp absorption edge, the energy of incident photon and the band gap (E_g) of a semiconductor will have the following relation

$$\alpha^n = A(h\nu - E_g) \tag{2.10}$$

$$(\alpha h\nu)^\gamma = A(h\nu - E_g) \tag{2.11}$$

where the value of γ depends on the interband transition mechanism.

Among the various methods, Tauc's plot is widely used to determine the band gap of the materials in which $(\alpha h\nu)^\gamma$ is plotted as a function of $h\nu$ following eqn 2.11. The value of γ is 2 for the direct allowed transition in the case of semiconductors.[11] For indirect band gap materials, the value of γ is 0.5 in the eqn 2.11, ν is the frequency and h is the Planks constant.

Optical absorption properties of the N-TiO_2 were studied with the aid of UV-Vis spectroscopy (Avantes) in the range from 200 to 750 nm.

2.5.2 X-ray Photoelectron Spectroscopy(XPS)

X-ray Photoelectron Spectroscopy(XPS), also known as Electron Spectroscopy for Chemical Analysis (ESCA) is a widely used technique to investigate the chemical composition of conducting and non conducting surfaces. In XPS, a surface is irradiated with X-rays (commonly Al Kα or Mg Kα) in vacuum. When an x-ray photon hits and transfers this energy to a core-level electron, it is emitted from its initial state with a kinetic energy dependent on the incident X-ray and binding energy of the atomic orbital from which it originated and is represented in the following relation.
$E_K = h\nu - E_B$;
where E_K is the kinetic energy of photo-electrons, hν is the incident photon energy and E_B the electron binding energy. This photo-electron is used to deduce the information regarding the surface under study. The photoelectron is characterized by few fundamental properties: its kinetic energy, its direction of emission with respect to specimen and the exciting radiation.[12]

A typical XPS system consists of (i) monochromatic X-ray source (ii) a sample stage (iii) an electron energy analyser combined with a detection system, all enclosed within vacuum chambers. Schematic of a typical XPS instrument is given in Fig 2.7.

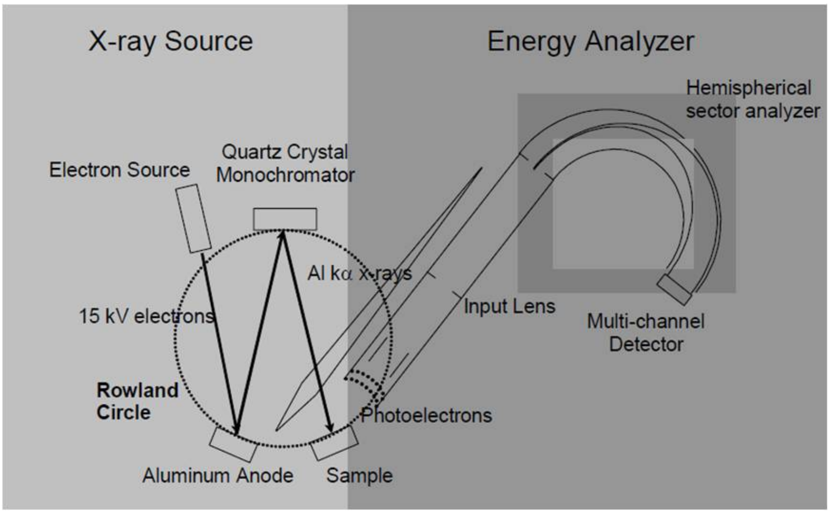

Figure 2.7 – A schematic of X-ray Photoelectron Spectrometer

For the present study of chemical composition the kinetic energy of the photo electrons has been studied using a SPECS make X-ray photo electron spectrometer, having monochromatic Al Kα radiation, at 1486.71 eV.

2.5.3 X-ray Absorption Spectroscopy(XAS)

Synchrotron sources emit intense, bright electromagnetic radiation consisting wide range of the energy spectrum, from infrared to many tens of keV. The radiation have unique directional and polarization properties, which makes it useful in various material characterization techniques. In this work, the focus will be on the application of hard X-ray from synchrotron for X-ray absorption spectroscopy.

X-ray absorption spectroscopy (XAS) generally deals with measurement of absorption coefficient, as a function of X-ray photon energy, around an X-ray absorption edge of an element, in a material. X-ray absorption spectrum consists of two parts: (i) The spectrum near the absorption edge (viz., the X-ray near edge structure or the XANES part) gives information about the external perturbations in the valence states to which electrons make transitions from core levels, upon absorption of X-ray photon energy and hence can yield information regarding hybridization of orbitals in case of molecule or long range order existing in a crystalline sample, apart from the oxidation states of the absorbing atom in the material. (ii) The second part of the spectrum which extends from 50 eV to ∼ 700 eV above the absorption edge, is generally called the Extended X-ray absorption fine structure (EXAFS) part, which is generally characterized by the presence of fine structure oscillations and can give precise information regarding the short range order and local structure around the particular atomic species in the material. This determination is confined to a distance given by the mean free path of the photoelectron in the condensed matter, which is between 5-7 Å radius from the element. The above charatersistic along with the fact that EXAFS is an element specific tool, makes EXAFS a powerful structural local probe. With the advent of modern bright Synchrotron radiation sources, this technique has emerged to be the most powerful local structure determination technique, which can be applied to any type of material viz. amorphous, polycrystalline, polymers, surfaces and solutions. Furthermore, EXAFS does not require any particular experimental conditions, such as high vacuum and hence, samples of various physical forms can be adapted for measurements in the experimental stations. Schematic of a typical X-ray Absorption measurement is given in Fig 2.8.

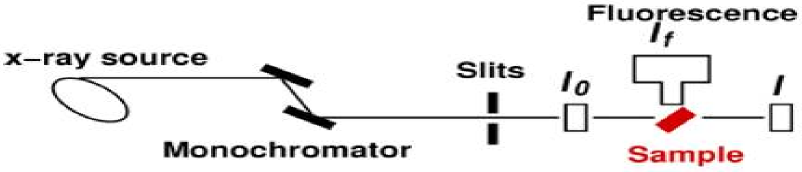

Figure 2.8 – A schematic of X-ray Absorption Spectrometer

2.5.3.1 *Theoretical Background*

The X-ray absorption coefficient for an atom in the photon energy range of 1-100 keV is generally dominated by Photoelectric effect, which is a monotonically decreasing function of energy, with several discontinuities known as absorption edges. These discontinuities occur when the energy of the incident photons equals the binding energy of different core levels of the atom and are classified with capital letters (K,L,M...) according to the principal quantum number of the core level ground state (n = 1, 2, 3...).An incident photon is able to extract a core electron, if its energy is equal to or greater than the edge energy. If the absorbing atom is isolated in space, the photoelectron propagates as an unperturbed isotropic wave, but in a real material since the absorber is surrounded by several neighbouring atoms, photoelectrons get backscattered and the final state of the photoelectron can be described, by the superposition of the original and scattered waves. This leads to an interference phenomenon that modifies the interaction probability between core electrons and incident photons. Constructive interference increases while destructive interference decreases the absorption coefficient of the atom. This interference phenomenon, for a given energy of the photoelectron, depends on the distance between emitting and scattering atoms and their scattering strengths and coordination numbers. Since the oscillations in the absorption spectra are important, the experimentally obtained μ versus E data is first plotted as $\mu(E)$ versus E, where $\mu(E)$ is defined as follows:

$$\chi(E) = \frac{\mu(E) - \mu_0(E)}{\Delta\mu_0(E_0)} \tag{2.12}$$

where E_0 is the absorption edge energy, $\mu(E)$ is the experimentally measured fluorescence, $\Delta\mu_0(E_0)$ is the edge step and $\mu_0(E)$ is a smooth background curve that is fit to the data to remove several extraneous contributions to the data. Data analysis in EXAFS is either done in k-space or in fourier transformed R-space. Hence the absorption co-efficient $\chi(E)$ is converted to k-space($\chi(k)$) using the following relation.

$$k = \sqrt{\frac{2m(E - E_0)}{\hbar^2}} \tag{2.13}$$

where m is the mass of the electron, $\chi(k)$ is often weighted by either k^3/k^2 to amplify oscillations at high/low k. The k-weighted $\chi(k)$ functions are fourier transformed to R- space using ARTEMIS software package to generate the $\chi(R)$ versus R spectra in terms of real distances from the centre of the absorbing atom. $\chi(R)$ versus R (radial distances) plots are then used to derive the co-ordination number and radial distances of the atoms in various co-ordination spheres.

Various physical parameters like, co-ordination number, bond distance etc is derived from EXAFS signal by using the following analytical expression, which is derived using dipole approximation:[13]

$$\chi(k) = \sum \frac{N_j f_j(k) e^{-2k^2\sigma_j^2} e^{-\frac{2R_j}{\lambda}}}{kR_j^2} Sin[2kR_j + \delta_j(k)] \tag{2.14}$$

where, N_j is the number of j th neighbours of the absorbing atom sitting at a distance of R_j, having a scattering amplitude of f_j and creates a phase change of δj as the photoelectron get scattered by its potential. The term σ_j represents the fluctuation at the atomic positions (having both structural as well as thermal effect) and λ is the mean free path which determines the probability of the scattering photoelectron to come back at the absorber, after being backscattered by the neighbour.

Different relevant parameters from the EXAFS signal are determined by fitting the experimental EXAFS spectra with the above theoretical expression. The amplitude, distance, phase and degeneracy of the different contributions corresponding to different interactions (nearest neighbour and further interactions), are used as fitting parameters for fitting the experimental data. Different codes for EXAFS data analysis programme are available among which, IFEFFIT package is most commonly used[14].

For a typical fitting of the spectra, crystallographic inputs of anatase phase is used. The real space fittings are performed between 0.9 to 4Å. Fourier transform are carried out from k = 2 to 8 Å^{-1} with multiple k-weight. It is known that reduced χ^2 is far greater than 1 in case of EXAFS due to poor assessment of the uncertainty in data and due to imperfections in the calculations that go into the model. Hence, the goodness of the fit has been measured by minimizing an alternate statistical parameter; known as R-factor. R-Factor is defined by the equation;

$$R = \frac{\sum_{i=min}^{max}[Re(\chi_d(r_i) - \chi_t(r_i))^2 + Im(\chi_d(r_i) - \chi_t(r_i))^2]}{\sum_{i=min}^{max}[Re(\chi_d(r_i))^2 + Im(\chi_d(r_i))^2]} \tag{2.15}$$

2.5.3.2 *Experimental Details of XAS Measurement*

EXAFS measurements with synchrotron radiation are generally carried out in two different modes viz., scanning and dispersive. Scanning modeis used for the work reported in this thesis.The experimental arrangement in scanning mode (generally called a beamline) uses a Double-Crystal–Monochromator (DCM) to select a particular energy from the incident synchrotron beam, which is then made incident on the sample and the intensity of the transmitted beam passing through the sample, or that of the fluorescence beam emerging out of the sample, is recorded with suitable detectors along with the incident intensity at each energy, by scanning the DCM crystals. Since, all the samples were thin films in the current work, fluorescence mode was used to record the data. The experiments were done at INDUS-2 Synchrotron radiation source a RRCAT, Indore, BL-09,[15] which is a Scanning EXAFS beamline.

2.6 Summary

The experimental techniques utilized for the study of N-TiO_2 thin films reported in this thesis are described briefly with basic principle, major components of the apparatus, and their technical specifications with schematic or block diagrams.

Bibliography

[1] Nakaruk, A.; Sorrell, C. C. Conceptual Model for Spray Pyrolysis Mechanism: Fabrication and Annealing of Titania Thin Films. *J. Coat. Technol. Res.* **2010**, *7*, 665.

[2] Pinna, N.; Garnweitner, G.; Antonietti, M.; Niederberger, M. A General Nonaqueous Route to Binary Metal Oxide Nanocrystals Involving a C-C bond Cleavage. *J. Am. Chem. Soc.* **2005**, *127*, 5608.

[3] Rockenberger, J.; Scher, E. C.; Alivisatos, A. P. A new Nonhydrolytic Single-Precursor Approach to Surfactant-capped Nanocrystals of Transition Metal Oxides. *J. Am. Chem. Soc.* **1999**, *121*, 11595.

[4] O'Brien, S.; Brus, L.; Murray, C. B. Synthesis of Monodisperse Nanoparticles of Barium Titanate: Toward a Generalized Strategy of Oxide Nanoparticle Synthesis. *J. Am. Chem. Soc.* **2001**, *123*, 12085.

[5] Hyeon, T.; Lee, S. S.; Park, J.; Chung,Y.; Na, H. B. Synthesis of Highly Crystalline and Monodisperse Maghemite Nanocrystallites without a Size-selection Process. *J. Am. Chem. Soc.* **2001**, *123*, 12798.

[6] Huang, Q.; Gao, L. A simple Route for the Synthesis of Rutile TiO_2 Nanorods. *Chemistry Letter.* **2003**, *32*, 638.

[7] Hoene, Joan Von; Charles, Robert G.;Hickam, William M. Thermal Decomposition of Metal Acetylacetonates. *J. Phys.Chem.* **1958**, *62*, 1098

[8] Marra, W.C.; Eisenberger P.; Cho, A. Y. X-ray Total External-reflection-Bragg Diffraction: A Structural Study of the GaAs-Al Interface. *J. Appl. Phys.* **1979**, *50*, 6927.

[9] Kaufmann, E.N. Characterization of Materials. *John Wiley and Sons, Inc. Hoboken, New Jersey.* ISBN: **0-471-26882-8**.

[10] Young, T. An Essay on the Cohesion of Fluids. *Philos. Trans. R. Soc. Lond.* **1805**, *95*, 65.

[11] Fuloria, N. K.; Fuloria, S. Spectroscopy: Fundamentals and Data Interpretation, *Studium Press India Pvt. Ltd.* **2013**

[12] Briggs, D.; Seah, M.P. Practical Surface Analysis by Auger and X-ray Photoelectron Spectroscopy, *John Wiley and Sons, New York* **(1985)**; *ISBN 10: 047126279X ISBN 13: 9780471262794*

[13] Konigsberger, D.C. ;Prince, R. X-Ray Absorption: Principles, Applications, Techniques of EXAFS, SEXAFS and XANES, (Wiley, New York, **1988**)

[14] Newville, M.; Ravel, B.; Haskel, D.; Rehr, J.J.; Stern, E.A.; Yacoby, Y. Analysis of Multiple-scattering XAFS Data using Theoretical Standards *Physica B.* **1995**, *154*, 208.

[15] Basu, S.; Nayak, C.; Yadav, A. K.; Agrawal, A.; Poswal, A. K.; Bhattacharyya, D.; Jha, S. N.; Sahoo, N. K. A Comprehensive Facility for EXAFS Measurements at the INDUS-2 Synchrotron Source at RRCAT, Indore, India. *J. Phys.: Conf. Ser.* **2014**, *493*, 012032.

Chapter 3

Doping of TiO_2 with Nitrogen.

3.1 Introduction

Titanium dioxide(TiO_2) is a wide band gap semiconducting oxide which finds application in the field of photo-catalysis,[1] solar cells,[2] gas sensors,[3] hydrophobic -hydrophilic switching coatings,[4] antimicrobial coatings etc.[5] owing to their tunable band structure. The photo-generated conduction band electrons and the valence band holes induce relevant redox surface reactions. However, one of the main issues associated with TiO_2 is the requirement of UV radiation with respect to its photo-activity for generating conduction band electrons and valence band holes. The most abundant source of this UV radiation is solar radiation which constitutes only $\sim 5\%$ of it and has been exploited for the photo-catalytic applications. It is well known that the visible region of solar spectrum is $\sim 50\%$ and the effective utilization of this natural solar energy warrants the proper tapping of this part of spectrum too. Therefore, several methods have been adopted in literature for this purpose. As will be explained in the next section, nitrogen doping of TiO_2 seems to be the most viable method. Narrowing the band gap of earth-abundant wideband gap metal oxide photocatalysts to increase their visible light absorption is crucial in advancing their applications in solar-to-fuel energy conversion.

Doping of TiO_2 by Nitrogen:

Among the various band engineering methods adopted to make visible light active TiO_2 , nitrogen doping has been found to be the most effective, taking into consideration the detrimental effects such as photo-corrosion, generation of electron-hole recombination sites etc.[6–11] The visible light activity in N-doped TiO_2 has been attributed to either reduction of band gap[9,12] or presence of isolated interband states.[13–15] This band gap alteration is dependent on the nature of nitrogen containing chemical species in TiO_2. In this context, it is pertinent to discuss chemical nature of the nitrogen in TiO_2, which in turn affect the band structure. Amongst the various methods for probing the chemical nature of nitrogen, X-ray Photoelectron spectroscopy(XPS) is the widely used technique. Since, XPS utilizes the binding energy of the photo-electrons to understand the surrounding chemical environment at a local level, titanium oxy nitride systems are referred in this article primarily to understand the chemical nature of nitrogen inside TiO_2 matrix.[16,17]. Other aspects of oxy-nitride systems with respect to difficulties in its synthesis are out of the purview of this work. Coming back to the chemical nature of the nitrogen in TiO_2, it is known that when nitrogen is doped in TiO_2, it can either replace the lattice oxygen or sit in the interstitial positions of the lattice, referred as substitutional nitrogen (N_s) and interstitial nitrogen (N_i) respectively. It is known that in case of substitutional nitrogen the band gap is lowered, while interstitial nitrogen introduces interband states.[18] It has been proposed in literature that, doping of TiO_2 under oxygen rich(deficient) atmospheres may lead to interstitial(substitutional) doping respectively.[18] In addition, nitrogen doping also leads to formation of molecular N_2 or NO kind of species in TiO_2 matrix. In the case of nitrogen-doped metal oxides, and oxynitrides, only the actual substitution of O^{2-} with N^{3-} with high N concentrations result in the desired band gap narrowing by elevating the valence band edge.[16,18] Furthermore, the position of nitrogen dopants with respect to the surface has an impact on the photoconversion efficiency.[19,20] Synthesis of N-doped TiO_2 in controlled conditions involves replacing the oxygen in TiO_2

by nitrogen atoms, which leads to creation of oxygen vacancies.[21–23] Theoretical calculations evidence that electronic structure of N-doped TiO_2 strongly depends on concentration of oxygen vacancies.[24] Hence, controlling the number of oxygen vacancies is paramount in obtaining the desired band gap. Details regarding the oxygen vacancies in TiO_2 under similar synthetic conditions as studied in this thesis will be discussed in another chapter. In addition, theoretical calculations revealed that a significant band gap narrowing occurs only under heavy nitrogen doping.[25,26] Thus, for band gap narrowing following conditions should be realized: (i) anionic N → O substitution and minimization of N_2 and NO structural defects, (ii) the optimal concentration of oxygen vacancies and (iii) the high doping level. Though, initially band gap narrowing was considered as the precondition to obtain visible light activity in TiO_2,it can still be obtained by introduction of interband states when nitrogen goes to a non-crystallographic location known as interstitial nitrogen. These interband states consist of N 2p states which lies just above the valence band consisting of O 2p states. The electrons get excited from these states to conduction band at a lower energy than the band gap energy thus making the material visible light active.

As the location (substitutional /interstitial), concentration and chemical state of nitrogen is crucial, it is pertinent to discuss these aspects in detail. Amongst the techniques available to probe the aforementioned properties, XPS (X-ray Photoelectron Spectroscopy) and XAS (X-ray Absorption spectroscopy)are two techniques which are widely used and are used in this thesis. Although, an alternate technique such as electron paramagnetic resonance(EPR) is often used to determine the chemical state, concentration and location of nitrogen vis-a-vis the TiO_2 lattice which can detect very low concentrations of paramagnetic species, it can not discriminate between interstitial and substitutional sites.[18] XPS is a surface analytical technique, which reveals information from surface and subsurface level by adopting in-situ sputtering techniques. The X-ray photo-electron spectrum corresponding to N 1s electron is noisy due to its low nitrogen concentration. Hence, XAS is particularly and routinely employed for the determination of the dopant location in the crystal lattice. Moreover, it also has the advantage of determining the co-ordination sites composed of elements possessing nearly equal X-ray scattering power.

This chapter discusses the synthesis of N-TiO_2 by spray pyrolysis, its structural and morphological charcterisation by GIXRD and FESEM. The optical properties have been studied by UV-Vis spectrometry while chemical nature and the quantitative evaluation of amount of dopant has been deduced using XPS. The electronic transitions, position of the nitrogen dopant and the effect of nitrogen doping on the local structure has been elucidated using XAS studies.

3.2 Synthesis of N:TiO_2 by spray pyrolysis method

Nitrogen doped TiO_2 thin films were synthesized by using a custom made ultrasonic spray pyrolysis set up. The synthesis consists of optimization of; (i)precursor volume; (ii) air column distance between the nebuliser exit and the substrate and(iii)synthesis temperature. The preliminary parameters for optimization were based on the work of Raut et el.[27] For a typical synthesis, 50 ml of 0.035 M titanium oxyacetylacetonate and 20 ml of 0.15 M hexamine solution in alcohol was first ultrasonically atomized using a 1.7 MHz ultrasonic nebulizer. The generated aerosols were expected to have fairly uniform size distribution in the range 0.5-5 μm with a maximum distribution around 3 μm.The aerosols were transported to Si(100) substrates fastened onto a flat heater, through a vertical glass column. These aerosols containing titanium oxyacetylacetonate and hexamine undergo oxidative decomposition at the substrate surface to form the desired Nitrogen doped TiO_2thin films. The substrate temperature T_s for synthesis of N-doped and pristine TiO_2 were varied from 400 to 550°C in steps of 50°C.

3.3 Characterisation of the N:TiO_2 films.

The film thicknesses measured using a surface profilometer (Dektak, USA) for the films synthesized are listed in Table 3.1. The thickness of the films ranged from 250 to 343nm. A pursual of the roughness values indicate that the films are sufficiently smooth and coherent.

Table 3.1 – Thickness and Roughness of N-TiO_2 thin films

Sample id	Film thickness(nm)	Film roughness(nm)
N:$TiO_2$400 °C	313	3.1
N:$TiO_2$450 °C	250	3.0
N:$TiO_2$500 °C	297	2.9
N:$TiO_2$550 °C	343	1.2

3.3.1 Crystallographic Studies

The GIXRD patterns of pristine and N-doped TiO_2 thin films shown in Fig 3.1 revealed formation of anatase phase, as evidenced from JCPDS file number 21- 1272 (space group $I4_1/amd$). The most intense peak corresponds to (101) plane of the anatase phase at a 2θ value of 25.30°. The crystallite size was calculated by using the Scherrer formula and is listed in Table 3.2. A clear increasing trend in crystallite size with synthesis temperature is observed from the table.

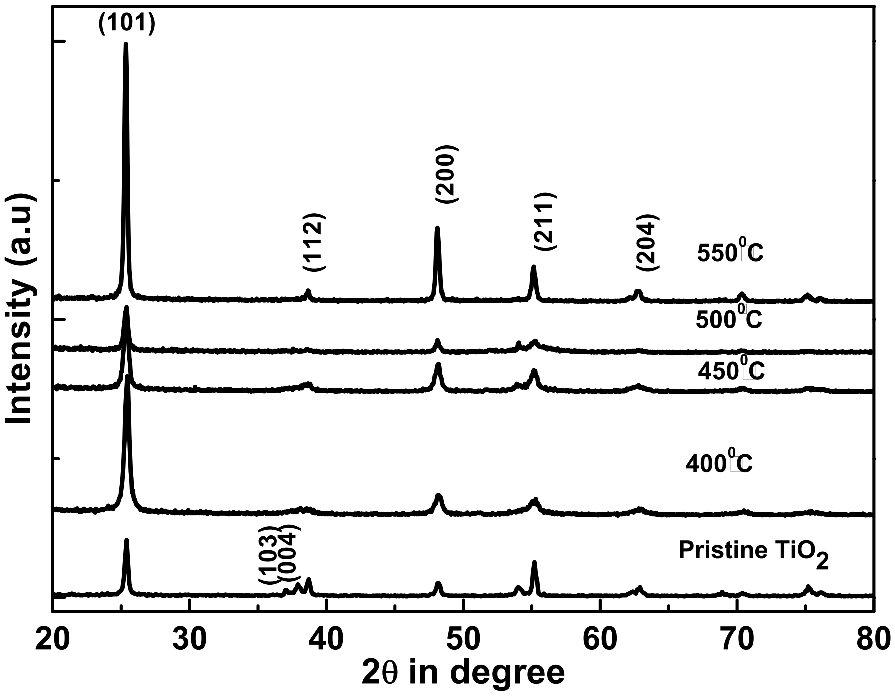

Figure 3.1 – GIXRD of N-doped TiO$_2$ synthesized at 400,450, 500 and 550 °C

Table 3.2 – Crystallite size of N-TiO$_2$ thin films

Sample id	Crystallite size(nm)
N:TiO$_2$400 °C	19± 2
N:TiO$_2$450 °C	27± 2
N:TiO$_2$500 °C	32± 3
N:TiO$_2$550 °C	54± 6

3.3.2 Microstructure

The evolution of microstructure (figure 3.2) of the films as a function of temperature was studied using FESEM. The surface morphology of the films synthesized at T$_s$ = 400 °C, 450 °C appeared smooth and dense indicating early stages of formation of grains. Formation of well defined grains with a width and thickness of 20 nm and 10 nm, respectively were observed for synthesis temperature of 500°C. The films synthesized at 550°C exhibited nano-platelets of 10 nm thickness with triangular and rectangular shapes, along with crystal twinning. The crystal twinning is associated with the increased grain size upon increase in T$_s$. When crystallites grow in size, the film is expected to experience reduced magnitude of strain. This strain relaxation is expected to cause the morphological changes giving rise to shape transition as observed in the FESEM images.[28]

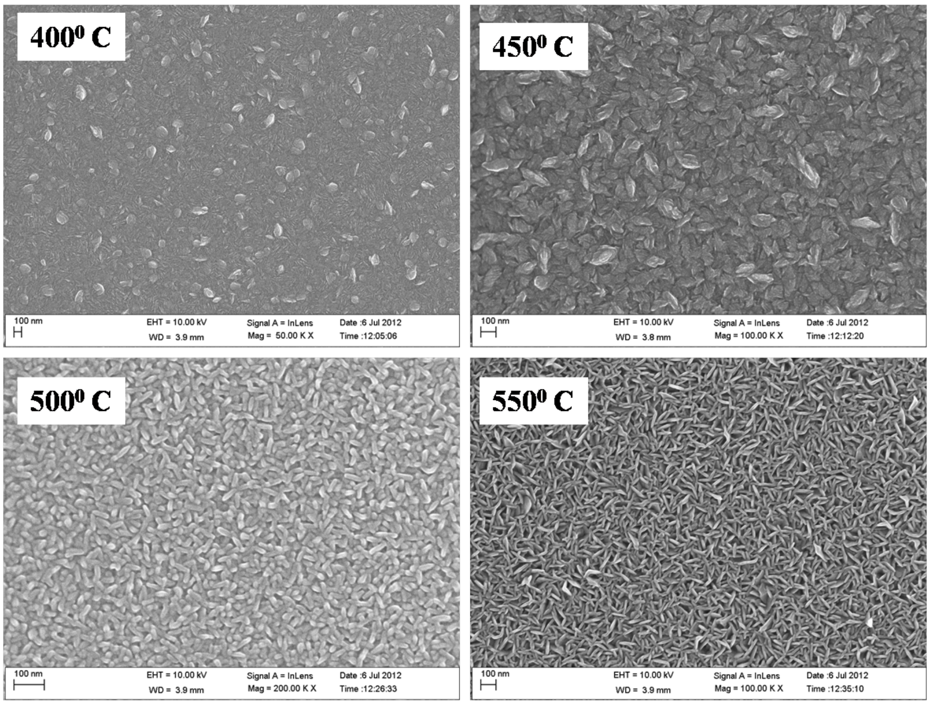

Figure 3.2 – FESEM of N-doped TiO_2 synthesized at 400, 450, 500 and 550 °C

3.4 Nitrogen concentration and nature of Bonding.

Concentration of nitrogen and its nature of bonding in N-doped TiO_2 thin films were calculated using X-ray photoelectron spectra (XPS). The high resolution spectra for N-doped TiO_2 thin films, given in Fig 3.3, 3.4, 3.5 and 3.6, were analyzed using the product of Gaussian and Lorentzian functions with the mixing parameter, 'm' being 30% Lorentzian. Conventional Shirley type fitting was used for background correction. The atom fraction of nitrogen was calculated using the following equation;

$$X_N = \frac{\frac{I_{N-1s}}{S_N}}{\frac{I_{Ti-2p}}{S_{Ti}} + \frac{I_{O-1s}}{S_O} + \frac{I_{N-1s}}{S_N}} \tag{3.1}$$

where I_{N-1s} is the peak area of the N-1s peak corresponding to O-Ti-N (N_O), I_{Ti-2p} is sum of the areas of the Ti_2p deconvoluted peaks and I_{O-1s} is area of the O-1s corresponding to bonded oxygen. The nitrogen concentration in 400°C, 450°C, 500°C and 550°C was found to be 9, 8, 7.5 and 2.6 % respectively.

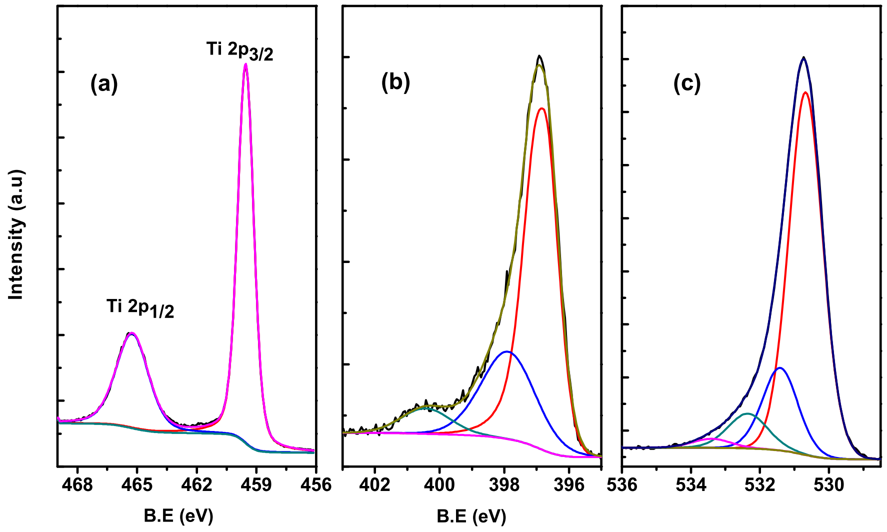

Figure 3.3 – X-ray photoelectron spectra details collected from the N-doped TiO_2 thin film deposited at 400°C (a) Ti $2p_{3/2}$, (b) N 1s and (c) O 1s core levels.

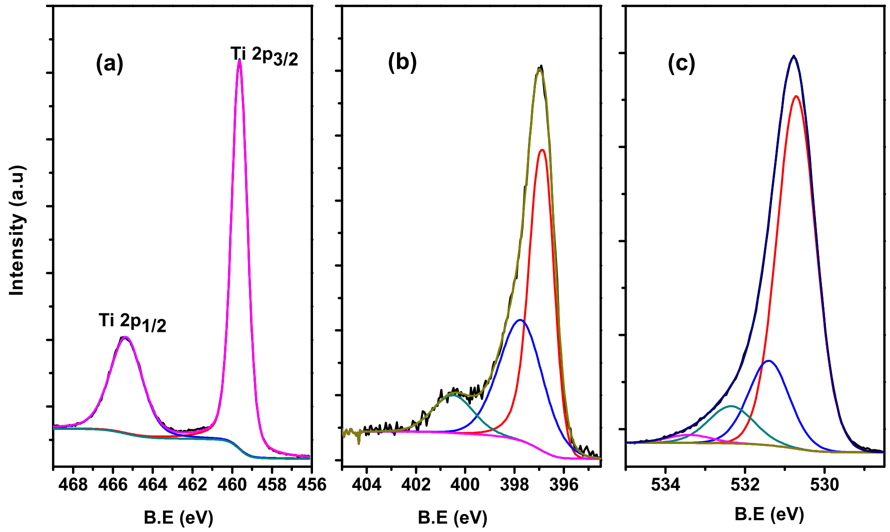

Figure 3.4 – X-ray photoelectron spectra details collected from the N-doped TiO_2 thin film deposited at 450°C (a) Ti $2p_{3/2}$, (b) N 1s and (c) O 1s core levels.

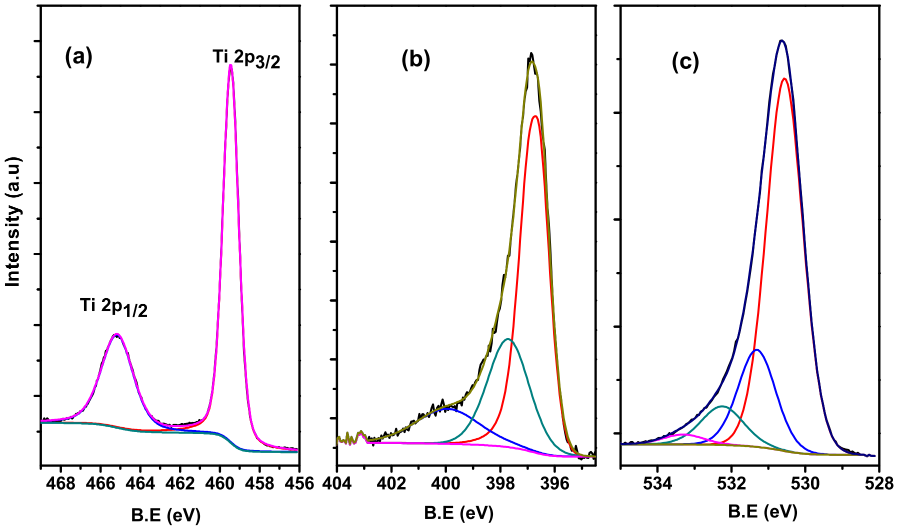

Figure 3.5 – X-ray photoelectron spectra details collected from the N-doped TiO_2 thin film deposited at 500°C (a) Ti $2p_{3/2}$, (b) N 1s and (c) O 1s core levels.

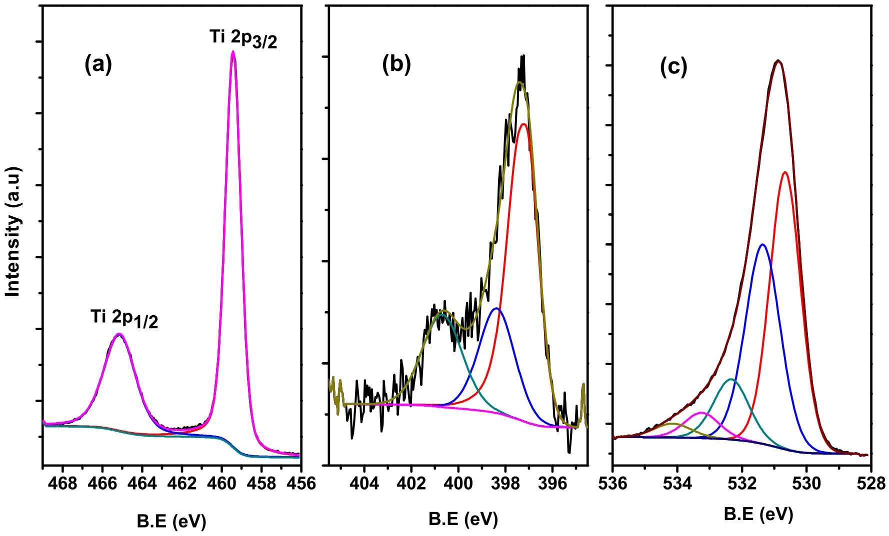

Figure 3.6 – X-ray photoelectron spectra details collected from the N-doped TiO_2 thin film deposited at 550°C (a) Ti $2p_{3/2}$, (b) N 1s and (c) O 1s core levels.

3.5 Optical properties

The optical band gap of the doped thin films are calculated using Tauc Plot (variation of $(\alpha h\nu^{0.5}$ with $h\nu$), obtained from the diffuse reflectance spectra of the films. The Tauc expression is given as;

$$(\alpha h\nu)^{\frac{1}{n}} = A(h\nu - E_g) \tag{3.2}$$

where h is the Planck's constant, ν frequency of vibration, α absorption coefficient, E_g band gap and A the proportionality constant. The value of the exponent 'n' denotes the type of transition. For direct allowed transition n=0.5 and for indirect allowed transition n=2. Since TiO_2 is an indirect band gap material, n = 2. The variation in $(\alpha h\nu^{0.5})$ with $h\nu$, for samples synthesized at T_s= 400, 450, 500 and 550°C, are shown in figure 3.7.

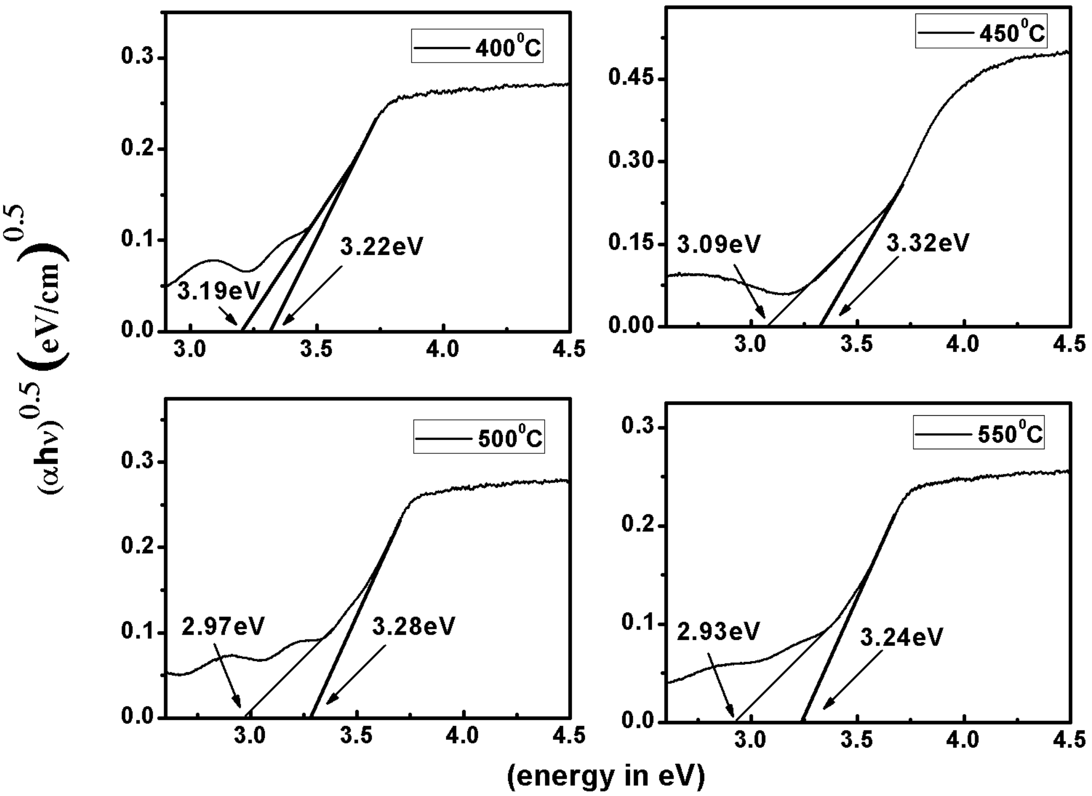

Figure 3.7 – Tauc plot of N-doped TiO_2.

It is seen from the spectra that there are two linear regions. The optical band gap obtained by taking the x-intercept at y=0 was between 3.22 eV - 3.32 eV. The intercept from the smaller linear region show energy states situated at 3.19, 3.09, 2.97 and 2.93 eV for films synthesized at $T_s = 400, 450, 500$ and 550 °C respectively. The additional features in the tail region of the spectra are due to the modified electronic structures although direct one to one correlation is not straight forward.[14] The presence of a linear region corresponding to the energy less than the band gap energy indicates introduction of interband states, as mixing of N-2p states with O-2p states are too weak to produce significant band gap narrowing in absence of a higher amount of N-doping.[13,45,46].These interband states consists of N 2p states with a finite electron density and are situated at a difference of around 0.2 to 0.3 eV. Since, these states lie above the valence band, the electrons from these states are excited to the conduction band at an energy value corresponding to visible region of the spectrum. This is in agreement with the study of Lee et al., whose first principle density-functional calculation has shown that absorption of visible light is due to isolated N-2p states (Interband states) above the valence band maximum.[14]

3.5.1 Nature of Bonding

In this work, hexamine is used as a precursor to introduce nitrogen into the TiO_2 matrix. Decomposition of hexamine yields H_2, NH_3, mono-, di- and trimethylamin etc in the working temperature regime of this work (400- 550 °C).[29,30] These nitrogen containing species when pyrolysed along with titanium oxy-acetyl acetonate in an open atmospheric condition may lead to various species like NO, NH, molecular nitrogen, Ti-N-O and Ti-O-N kind of linkages inside TiO_2 matrix. Hence, to understand the chemical nature of the nitrogen in TiO_2 N-1s apectra obtained from XPS are analysed here.

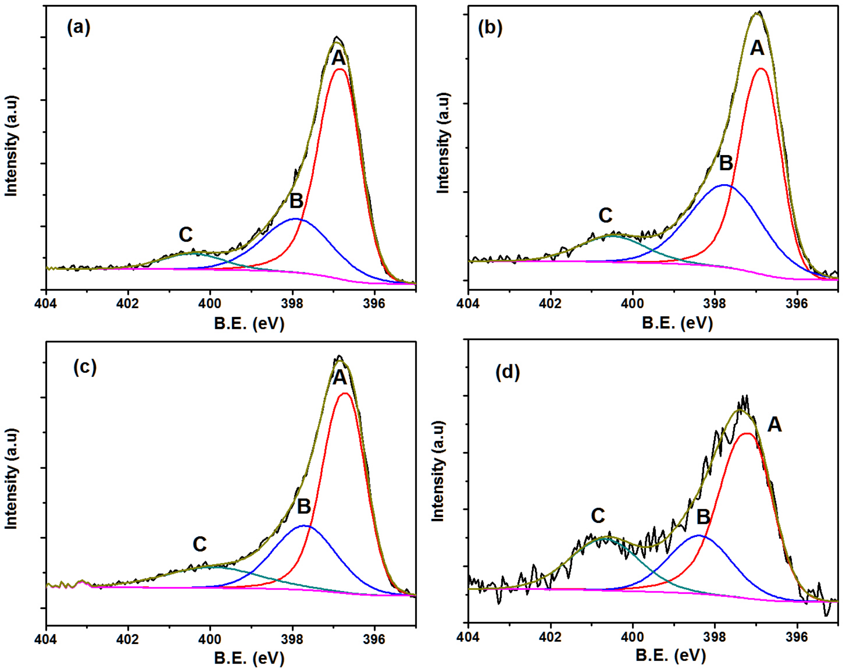

Figure 3.8 – N-1s spectra of N-doped TiO_2, synthesized at (a) 400,(b) 450, (c) 500 and (d) 550 °C at 6 minutes sputter depth.

N-1s spectra of the samples synthesized at 400, 450, 500 and 550°C, obtained after 6 minutes sputtering, are given in figure 3.8. Deconvolution of high resolution N-1s spectra of all the samples show one high intensity peak at 396.6 eV(Peak A) and two low intensity peaks at 397.5(Peak B) and 400.1 eV(Peak C). The different N-1s BE values represent different electron density around nitrogen suggesting various N environments in the lattice, which are enumerated below.

1. Peak A(396.6 eV) of N1s spectrum has been either inferred as substitutional nitrogen or as chemisorbed atomic nitrogen (widely denoted as β-N) which is terminally attached to the matrix at the surface through σ bonding.[13,17,31–35]

2. Peak B (397.5eV) has been either inferred as Ti-O-N kind of linkages of the oxynitrides[17] or chemisorbed N_2, which is attached to the matrix via π bonding. However, since this study employs hexamine as dopant precursor, which undergoes vapor phase decomposition to yield N-doped TiO_2, chemisorbed N_2 is safely ruled out here.[36] Ti-O-N kind of linkages are broadly represented by

the binding energies in the range of 395.6- 397.1 eV. Saha et al. has studied oxynitrides and found that when the nitrides undergo oxidation the peak at 397.1eV experiences a shift in its position depending on the degree of oxidation. Hence, the peak at 397.5 eV can be ascribed to Ti-O-N kind of linkages of the oxynitrides and has been described as an intermediate peak by Saha et al.[17] The variation in binding energy in the range of 395.6- 397.1 eV also depends on the variation in the oxygen to nitrogen ratio.

3. Peaks in the regime of 399–401 eV are ascribed to surface adsorbed NO,[37] bulk interstitial NO^{2-},[38] interstitial N_2 ,[33] and interstitial N.[39–41] In this work, peak C (only a small peak centered at 400 eV) is observed and is attributed to either NO kind of chemical species or interstitial NO^{2-}.[42–44]

Since, the position of nitrogen in a lattice affects the electronic structure of the material, it is prudent to discuss Peak A in detail here, which signifies nitrogen replacing an oxygen from its lattice point in TiO_2 lattice. A careful and detailed literature survey in this aspect revealed that Peak A is broadly referred as substitutional nitrogen owing to the fact that it matches with the binding energy of N1s in Titanium Nitride crystallographic phase and does not necessarily mean that nitrogen replaces an oxygen from the lattice site. It is known that XPS as a technique is capable of measuring the binding energy which in turn is indicative of its oxidation state. However, it does not offer any insight into the crystallographic positions occupied by an atom, which is being probed. Hence, it is safe to say that peak A represents Ti-N kind of linkages without committing to its crystallographic site.

As the crystallographic position can not be deduced from XPS, it can not be committed at this juncture whether the chemical species is NO or interstitial nitrogen sitting at a non lattice point with a Ti-N bond length different from the Ti-N bond distance when 'N' is located at a lattice point. Thus, the XPS data reveal incorporation of nitrogen to the TiO_2 crystal lattice as Ti-N and NO. Three kinds of chemical species which are most likely formed under the synthetic conditions used in this work is represented in Scheme 3.1.

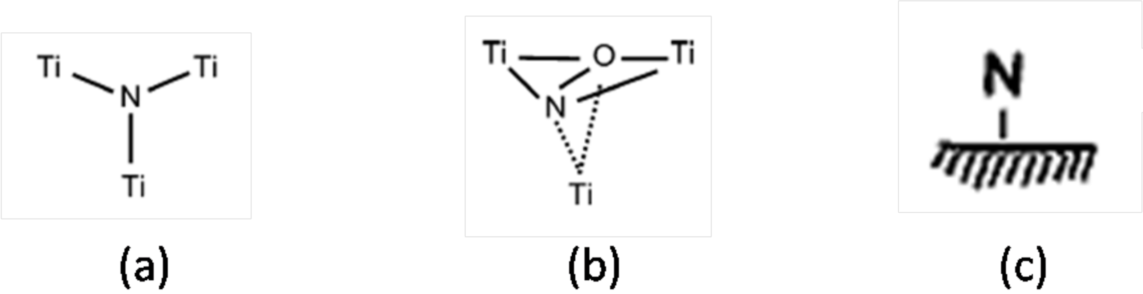

Scheme 3.1 – (a) Substitutional nitrogen (b) Interstitial nitrogen (C) Terminally bonded atomic like Nitrogen(β-N).

Since, XPS as a technique can only distinguish between different chemical environment around a particular element and can not shed light on the crystallographic position occupied by the said atom inside a matrix, X-ray absorption spectroscopy was employed to pinpoint the position of the nitrogen atom inside TiO_2 matrix, which will be discussed in the following section.

3.6 X-ray Absorption studies

As mentioned in the introduction and in the previous section, X-ray Absorption Spectroscopy (XAS) is employed for the determination of the dopant location in the crystal lattice. Moreover, it also has the advantage of determining the co-ordination sites composed of elements possessing nearly equal X-ray scattering power. Since, the location of the nitrogen is of paramount importance in the current study, XAS spectra were analyzed to deduce the location of nitrogen and the resulting change in Ti-N bond distance from the ideal value in TiO_2 matrix. This section discusses, XAS studies of N-doped TiO_2(anatase) thin films synthesized by spray pyrolysis method. X-ray Absorption Spectrum is broadly classified into three regions; Pre-edge, Edge and Post edge region, which is discussed below.

3.6.1 Analysis of the XAS spectrum

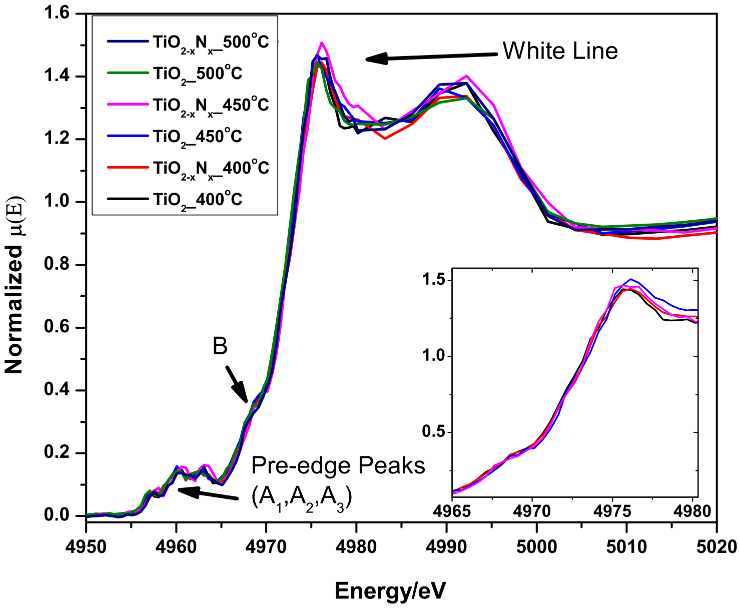

Figure 3.9 – Normalised Ti K-edge Spectra For Pristine and N-doped TiO_2.

X-ray Absorption Spectrum of spray pyrolysis synthesized TiO_2 and N-doped TiO_2 anatase films is given in Figure 3.9. XAS spectra possesses three distinct regions viz. the edge, pre-edge (Peak A_1, A_2 and A_3) and an extended region after the edge. The edge has a white line (Figure 3.9) above the edge in the present study. The white line is characteristic of anatase phase as confirmed from section 3.3.1) and can be attributed to the promotion of a photoelectron to the vacant np orbital of Ti or the anti-bonding orbitals of Ti-O.[47]

In addition to this, XAS spectra is characterized by sharpness of absorption step maxima and the rate at which the absorption spectra tails off, which is a function of sample thickness according to Grunes et al.[48] They observed that thinner samples produce sharp absorption step and a rapidly decaying tail. By comparing the absorption spectra of the doped and pristine TiO_2 thin films, it has been observed that the absorption spectrum tails off rapidly for samples synthesized at T_s= 500°C, which are the thinnest compared to that of those synthesized at T_s= 400, 450°C .[48,50]

The observed thickness is explained on the basis of mechanism of film synthesis. It is known that depending on the synthesis temperature the precursor condensates on the substrate and then undergoes reactive decomposition or the precursor evaporates and the vapor undergoes reactive decomposition on the substrate to form the thin film. At higher temperatures precursor vapor decomposition followed by deposition of the decomposition product (TiO_2) onto the substrate is also possible. At low temperature ($T_s = 400$°C), deposition of precursor followed by decomposition is the preferred path, whereas at the moderate temperature ($T_s = 450$ °C) evaporation of precursor followed by vapor reactive decomposition at the substrate surface is the preferred route. At 500 °C decomposition of precursor vapor before reaching the substrate is expected. In such a situation the film synthesized at T_s= 500 °C will be porous and thinner. The effect of the substrate temperature on the thickness of the samples is corroborated in the present study.[49]

3.6.2 Near edge (Pre-edge) Features

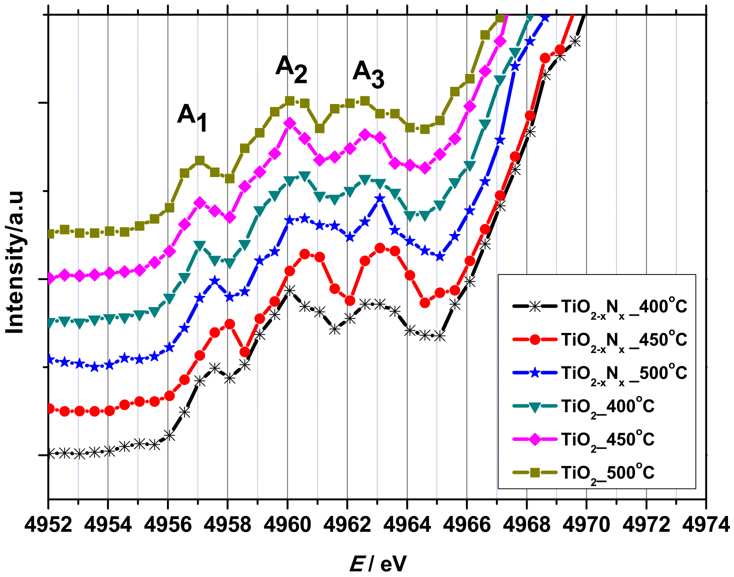

Figure 3.10 – Near edge Features of Ti K-edge for Pristine and N-doped TiO_2

The pre-edge region consists of three pre-edge peaks (A_1, A_2 and A_3 at 4957, 4961 and 4963 eV respectively) is given figure-3.10. Occurrence of these three peaks in the pre-edge region is attributed to lack of centre of inversion symmetry in anatase, which consists of distorted TiO_6 octahedrons. The effect of presence of inversion symmetry on the near edge features has been described by Sandstrom *et al.* They observed that when a system lacks a centre of inversion symmetry the pre-edge features consists of weak dipole forbidden 1s-3d transitions.[52] The effect of lack of inversion symmetry on the XAS spectrum is understood by studying XAS in the frame work of either one electron transition model or many body corrections to the one electron model. In one electron transition model, only one electron is excited to an unfilled state present in initial, unperturbed solid without affecting any other electrons in the atom. Though this model has successfully described the X-ray absorption cross sections of metals, it has failed to explain the absorption cross section of metal oxides, where a few electron volt band gap is present. This happens because the excited electrons are poorly screened by the valence electrons from the core-hole. So, many body corrections like relaxation of valence electrons with respect to core-hole, excited electron-core hole interactions come into play, thus relaxing the symmetry of the final states of the transitions.[48] For metal oxides, Glen *et al.* described the origin of K- edge near edge spectra using one e- molecular orbital theory type transitions whose energies are modified due to presence of core-holes though some features are still unexplained.[51] This in turn leads to dipole forbidden transitions as opposed to the dipole selection rule of XAS, i.e $\Delta l = \pm 1$; $\Delta l = +1$ being the favored transition.

In light of this, the origin of pre-edge peak A_1 is ascribed by Chen et al. to an exciton band or due to 1s to $1t_1g$ transition from possible perturbation due to shake-up and shake-off processes and the origin of A_2 and A_3 is attributed to the 1s-$2t_2g$ and 1s-$3e_g$ transitions in the octahedral field, respectively .[53] Chen et al. observed a systematic increase in the intensity of the A_2 peak with decrease in particle size indicating an increase in TiO_6 octahedron distortion because of the anisotropic environment felt by the Ti atoms on the surface of the nano-particles. No such variation was observed in the present study mainly because, compared to nano-particle powder, the difference in number density of surface TiO_6 octahedra between the thin films, due to the difference in crystallite size, is small.

The reason and explanation for weak near edge peak B (shown in figure 3.9) is less clear cut as compared to Pre-edge peaks A_1, A_2 and A_3. Glenn and Dodd described it as a resultant of monopole 1s-to-4s transitions to the $3a_{1g}$ molecular orbital.[51] However, they have arrived at this conclusion using molecular orbital theory and one electron transitions. Since, TiO_2 is an insulator and has a long range order, a simple molecular orbital approach could not be competent enough to explain the near edge feature B. Hence, it is attributed to 1s to 4p ($4t_1u$) transitions by considering the solid state contributions due to long range order, to describe the final state wave functions.[54–56]

Apart from the occurrence of pre-edge peaks, a comparison among N-doped and undoped samples shows that that the A_1, A_2 and A_3 peaks shift towards higher energy side in the case of N-doped TiO_2 as compared to pristine TiO_2. This is attributed to the higher oxidation state of the core metal atom (Ti), induced by nitrogen in the co-ordination sphere.[48] The presence of nitrogen in the co-ordination sphere is also corroborated from the analysis of extended X-ray absorption spectra which will be discussed below.

3.6.3 EXAFS (Extended X-ray Absorption fine Structure)

The extended region of a XAS spectrum (100-200eV after the edge) is known as extended X-ray Absorption fine Structure (EXAFS). EXAFS reveals information about the bond distance, nature of the dopant (substitutional /interstitial) and co-ordination number of the atom under probe, which is extracted from the extended region of the spectra by fitting the Fourier transformed data in R-space($\chi(R)$ versus R) using ARTEMIS software package as described in Chapter 2. A typical fitting procedure includes (i) theoretically generating a model (using FEFF, whcih is included in Artemis Package) of TiO_2, which generates Ti-O paths with certain initial fit parameters, (ii) Optimising the initial fit parameters so as to obtain the lowest value of R (R is a statistical parameter described in Chapter 2). In the present study, crystallographic inputs of anatase phase was used in FEFF to generate the initial model for fitting of the XAS spectra.

TiO_6 octahedron is a distorted octahedron in case of anatase phase. The real space fittings were performed between 0.9 to 3.8 Å. Fourier transform were carried out from k = 2 to 8 $Å^{-1}$. The Fourier transform have been carried out with multiple k-weight. Four path parameters ($S_0{}^2, \Delta r, \Delta E_0, \sigma^2$) for each path were taken into consideration for the fitting of experimental data with feff generated modeling using ARTEMIS, which has IFEFFIT integrated in it.[57] During the fitting process, the number of free variables were always kept below the upper limit set by Nyquist theorem ($N_{free}= 2\Delta k \Delta r/\pi + 1$). Four paths i.e $(Ti\text{-}O)_{eq}$ and $(Ti\text{-}O)_{ax}$ from the first co-ordination sphere and two Ti-Ti paths from the immediate co-ordination sphere were considered for the fitting of pristine spectra. Only the single scattering paths were included in the analysis, since the rank of multiple scattering paths were very low. The overall value of R-factor was then tried to be minimized to establish the goodness of the fit.

For determining the position of nitrogen, two ways were considered viz; the first method involves replacement of one Ti-O path out of six Ti-O paths with Ti-N , the second method involves taking an independent Ti-N path from titanium nitride apart from six Ti-O path pertaining to TiO_6. In the first case scenario, when oxygen in the anatase structure was replaced with a nitrogen to build a theoretical model of titanium dioxide with substitutional nitrogen and the resultant paths were optimized to fit the experimental data, the R value was very high. However, when Ti-N path from a different feff calculation of only TiN was used along with paths from anatase phase, R value improved drastically. While generating the theoretical model of TiN, it was kept in mind that the TiN phase of a cubic space group i.e $Fm\bar{3}m$ is used , in which Ti atom had the same site symmetry as that of Ti in TiO_2 anatase. The change in co-ordination number incurred due to nitrogen insertion was accommodated in amplitude (${S_0}^2$) of the fit parameters. The ${S_0}^2$ of Ti-N path was set to be x and both $(\text{Ti-O})_{eq}$ and$(\text{Ti-O})_{ax}$ paths were set as 1-x. The fitted curves in R-space is given in fig 3.11 and that of k- space is given as fig 3.12.

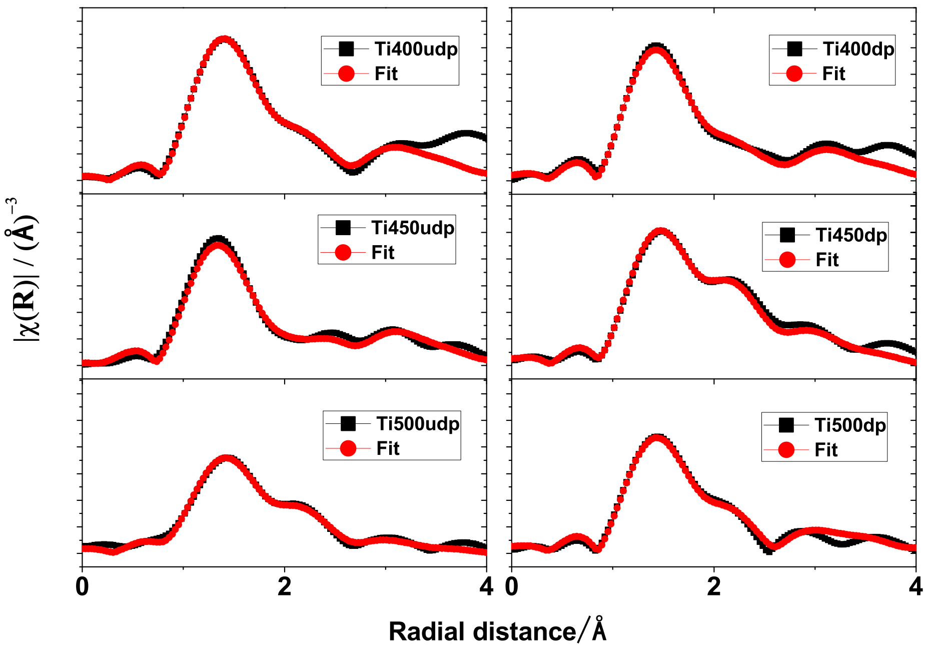

Figure 3.11 – Extended Region fitting using ARTEMIS in R-space.

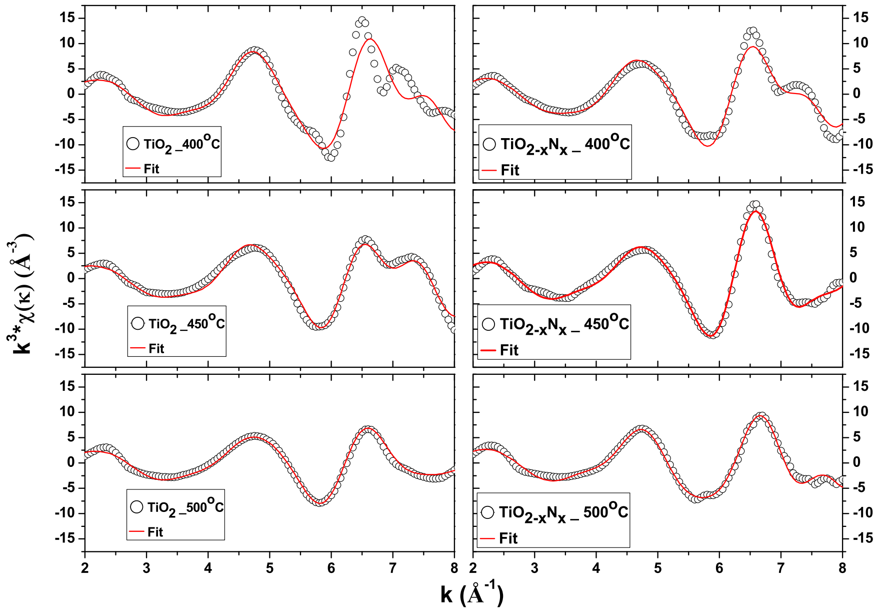

Figure 3.12 – Fitted magnitude of k^3-weighted Ti K-edge EXAFS spectra For Pristine and N-doped TiO_2.

Table 3.3 – Fitted path parameters for the pristine TiO_2 thin films

Sample id	Paths	Bond length (Å)	C.N($N * S_0{}^2$)	σ^2 (Å)^2	R
$TiO_2$400 °C	Ti-O	1.913(1)	4.00(1)	0.0012(1)	0.03
	Ti-O	1.915(5)	0.866(2)	0.0011(5)	
$TiO_2$450 °C	Ti-O	1.910(1)	4.80(1)	0.0010(5)	0.02
	Ti-O	2.184(2)	1.468(04)	0.0010(2)	
$TiO_2$500 °C	Ti-O	1.960(1)	3.204(3)	0.0010(1)	0.005
	Ti-O	1.824(03)	1.298(6)	0.0010(2)	

Table 3.4 – Fitted path parameters for the N-doped TiO_2 thin films

Sample id	Paths	Bond length (Å)	C.N($N * S_0{}^2$)	σ^2 (Å)^2	R
$TiO_{2-x}N_x$400 °C	Ti-O	1.952(1)	3.072(7)	0.0010(5)	0.01
	Ti-O	1.953(1)	1.536(7)	0.0010(4)	
	Ti-N	2.326(2)	1.344(7)	0.0010(5)	
$TiO_{2-x}N_x$450 °C	Ti-O	1.949(1)	3.292(3)	0.0017(2)	0.01
	Ti-O	1.984(3)	1.646(3)	0.0010(2)	
	Ti-N	2.334(1)	1.056(3)	0.004(3)	
$TiO_{2-x}N_x$500 °C	Ti-O	1.954(3)	2.920(03)	0.0017(1)	0.02
	Ti-O	1.984(2)	1.460(04)	0.0010(3)	
	Ti-N	2.371(02)	1.614(03)	0.0010(03)	

The Ti-O distances and the co-ordination numbers corresponding to each path, obtained from the EXAFS, for the pristine and N-doped TiO_2 anatase samples are shown in Table 3.3 and 3.4.

3.6.3.1 Discussion on Co-ordination Number.

The co-ordination number of Ti in the first co-ordination sphere for the undoped TiO_2 (table 3.3) synthesized at T_s = 400, 450 and 500 °C is 4.8, 6.2 and 4.4 respectively. The films obtained at T_s = 450 °C is found to be stoichiometric compared to those obtained at T_s = 400 and 500 °C. The substoichiometry of the films obtained at T_s = 400 and 500 °C is attributed to the thin film formation pathways followed at the respective synthesis temperatures. In the present study, the thin film formation pathway can be described as solvent evaporation followed by reactive decomposition of the precursor (Titanium oxyacetyl acetonate) at or near substrate surface. From the surface morphologies of the films obtained at 400, 450 and 500 °C, it is inferred that at T_s = 400 °C, the precursor undergoes reactive decomposition at the substrate immediately after solvent evaporation, resulting in TiO_2 films without well defined grains.[49] Whereas at T_s = 450 °C, the precursor undergoes vaporization after the solvent evaporation and the vapors undergo reactive decomposition at the substrate to give TiO_2 films of well defined grains. At T_s = 500 °C, the precursor vapors decompose to TiO_2 before reaching the substrate and the nascent TiO_2 deposit onto the surface giving rise to porous TiO_2 coating. Thus, in the present experimental condition, 450 °C is found to be the ideal substrate temperature for synthesis of stoichiometric TiO_2 thin films.

The co-ordination number of Ti with respect to oxygen atoms in the first co-ordination sphere in the N-doped TiO_2 (table 3.4) synthesized at T_s = 400, 450 and 500 °C is 4.6, 4.9 and 4.3 respectively. A look at the co-ordination number of Ti-O atoms in the first co-ordination sphere for doped samples reveal that, when nitrogen is introduced at a bond distance of ≈2.33 Å, the number of oxygen atoms in the first co-ordination sphere decreases. It is clearly seen that N-doped TiO_2 follows the similar trend in stoichiometry as that of TiO_2. The co-ordination number of Nitrogen in the Ti with respect to doped nitrogen is 1.35, 1.06 and 1.62 in the case of films synthesized at T_s = 400, 450 and 500 °C respectively.

3.6.3.2 Discussion on Bond lengths.

The $(Ti\text{-}O)_{ax}$ and $(Ti\text{-}O)_{eq}$ distances obtained in the present study are compared with the PAW-DFT calculated values from ref[59] and is given in Table-3.5.

Table 3.5 – Comparision of Ti-O bond distances for pristine TiO_2 obtained from DFT calculation[59] and EXAFS [present study]

Bond distance	Stoichiometric TiO_2	$V_o(eq)$(i)	$V_o(ax)$(i)	400°C(ii)	450°C(ii)	500°C(ii)
$(Ti\text{-}O)_{eq}$	1.94/1.95	1.81/1.92/1.91	1.86	1.913(1)	1.910(1)	1.960(1)
$(Ti\text{-}O)_{ax}$	2.00/1.98	1.92/1.96	1.93/1.92/1.90	1.915(5)	2.184(2)	1.824(0)

i) Calculated values from DFT by Ceotto et al.(From Table 1 and 2 of reference[59])
ii)Values from the present EXAFS study.

It is observed from table 3.3 that $(Ti\text{-}O)_{eq}$ remains almost same for pristine samples synthesized at T_s = 400 °C (1.913(1) Å) and 450 °C (1.910(1) Å), whereas for the films synthesised at T_s = 500 °C, it is 0.05 Å higher (1.960(1) Å). $(Ti\text{-}O)_{ax}$ bond distances vary in the following order;

$(Ti\text{-}O)_{ax\ (500)}$ 1.824(0) Å< $(Ti\text{-}O)_{ax\ (400)}$ 1.915(5) Å< $(Ti\text{-}O)_{ax\ (450)}$2.184(2) Å.

The trend in axial bond distances is in agreement with the earlier reports.[59] The $(Ti\text{-}O)_{ax}$ (2.18 Å) and $(Ti\text{-}O)_{eq}$(1.91 Å) obtained for the stoichiometric film made at 450 °C is close to the PAW-DFT calculated value of 2.0 and 1.94 Å respectively, obtained by Ceotto *et al.*[59] In the case of the sub-stoichiometric samples oxygen vacancies can be in the axial or equatorial positions, and the $(Ti\text{-}O)_{ax}$ and $(Ti\text{-}O)_{eq}$ distances depend on the oxygen vacancy position. The PAW-DFT calculated $(Ti\text{-}O)_{ax}$ and $(Ti\text{-}O)_{eq}$ distances in the presence of axial / equatorial oxygen vacancies are given in Table-2 of the paper by Ceotto *et al.*[59] The PAW-DFT calculated $(Ti\text{-}O)_{ax}$ and $(Ti\text{-}O)_{eq}$ distances in the presence of axial oxygen vacancies are 1.86 Å and 1.90/1.92/1.93 Å respectively. The value matches with those of the samples synthesized at 500 °C ((Ti-O)$_{ax}$ = 1.824 Å and (Ti-O)$_{eq}$ = 1.96 Å). The calculated (Ti-O)$_{ax}$ and (Ti-O)$_{eq}$ distances in the presence of equatorial oxygen vacancies are 1.92/1.96 and 1.81/1.92/1.91 Å respectively. The values are in reasonable agreement with those of samples synthesized at T$_s$ = 400 °C ((Ti-O)$_{ax}$ = 1.915 Å and (Ti-O)$_{eq}$ = 1.913 Å). From a careful comparison of the calculated values with the EXAFS values obtained in the present study it can be discerned that for the sub-stoichiometric samples, oxygen vacancies are present at both axial and equatorial positions.

Similarly, a clear trend in (Ti-O)$_{ax}$ as well as the Ti-N bond distances are observed for the N-doped TiO$_2$ thin films synthesized at T$_s$ = 400, 450 and 500 °C from table 3.4. The (Ti-O)$_{eq}$ remains nearly constant in all the three samples. (Ti-O)$_{ax}$ has a value of 1.953(1) Å at 400 °C and 1.984(3) Å at 450 °C and 1.984(2) Å at 500 °C. To have a better understanding of variation in the bond length in undoped and N-doped TiO$_2$ films with respect to temperature; bond length vs Synthesis temperature is plotted and shown in Figure 3.13.

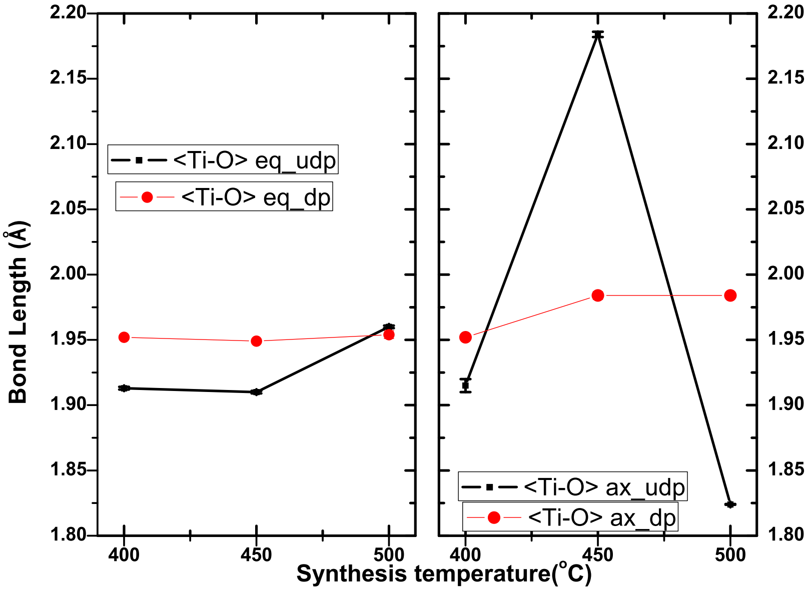

Figure 3.13 – Bond length vs synthesis temperature

Assuming the (oxygen vacancy) / Ti ratio to be same as that of N/Ti (a rough estimate) the weighted average of the PAW-DFT calculated Ti-N bond distance is found to be 2.2 Å which is close to the EXAFS value obtained in the present study (2.3 Å).

When a certain amount of nitrogen is introduced into the thin film, it either replaces a lattice point oxygen known as substitutional (N_s) or goes to non lattice point locations widely known as interstitial (N_i) nitrogens and creates four kinds of Ti-centered octahedrons viz. octahedron having one nitrogen (TiO_5N), octahedron having nitrogen as well as an oxygen vacancy ($TiO_4N\ V_o$), octahedron having only an oxygen vacancy (TiO_5V_o) and pristine TiO_6 octahedrons. In the present study, only the nitrogens at non-lattice points (henceforth referred as (N_i)) are considered, since substitutional nitrogen could not yield a decent fit with discernible parameters. The Ti-O bond distances derived from EXAFS is an average of all the bond distances. So, to gain a holistic view of how these bond distances vary with different amount of nitrogen concentrations, the EXAFS derived bond distances are compared with the bond distances derived from DFT calculations done by Ceotto et al.[59]

Table 3.6 – Comparision of Ti-O bond distances obtained from DFT calculation[59] and EXAFS [present study]

Synthesis Temp.	N/Ti (Atom Ratio)	$(Ti\text{-}O)_{eq}$ (i)[59]	$(Ti\text{-}O)_{eq}$ (ii)(dp)	$(Ti\text{-}O)_{eq}$ (ii)(udp)	$(Ti\text{-}O)_{ax}$ (i)[59]	$(Ti\text{-}O)_{ax}$ (ii)(dp)	$(Ti\text{-}O)_{ax}$ (ii)(udp)
400°C	0.282	1.94	1.952(1)	1.913(1)	1.98	1.953(1)	1.915(5)
450°C	0.237	1.94	1.949(1)	1.910(1)	1.98	1.984(3)	2.184(2)
500°C	0.24	1.94	1.954(3)	1.960(1)	1.98	1.984(2)	1.824(03)

i) Calculated values by considering the N/Ti atom ratio along with the values from DFT by Ceotto et al. ii)Values from the present EXAFS study;dp-doped;udp-undoped.

Knowing the fraction of each type of octahedron present, one can theoretically calculate the average $(Ti\text{-}O)_{ax}$ and $(Ti\text{-}O)_{eq}$ bond distances of interstitially N-doped TiO_2. So, to evaluate the average $(Ti\text{-}O)_{ax}$ and $(Ti\text{-}O)_{eq}$ bond distances from the DFT, average $(Ti\text{-}O)_{ax}$ and $(Ti\text{-}O)_{eq}$ of TiO_5N_i, $TiO_5\ N_i\ V_o$ and $TiO_5\ V_o$ were calculated. The axial and equatorial distances corresponding to each case is obtained from column 5, 6 of Table 1 and column 6, 7 of table 2 ref [59].[59]. For a given N/Ti fraction "x", there will be x number of ocathedrons, which are affected by nitrogen(i.e. TiO_5N_i, TiO_5 N_i V_o and TiO_5 V_o) and 1-x number of pristine octahedrons (TiO_6). The average $(Ti\text{-}O)_{ax}$ is then given by the summation of x fraction of $(Ti\text{-}O)_{ax}$(DFT N-doped) and (1-x) fraction of $(Ti\text{-}O)_{ax}$(DFT Pristine). Similar method is followed for the bond distance of $(Ti\text{-}O)_{eq}$. The value of $(Ti\text{-}O)_{ax}$(DFT Pristine) or $(Ti\text{-}O)_{eq}$(DFT Pristine) is obtained from column 2 of table 1 of ref [59].[59] The final calculated average Ti-O distance for interstitially doped N-TiO_2 corresponding to different N-concentrations of the present study is given in Table 3.6 and is compared with the Ti-O distances obtained from the present EXAFS results. There is very good agreement between the DFT calculated values and those obtained from EXAFS study for samples synthesized at 450 and 500°C. The agreement for samples made at 400 °C is reasonable.

In addition, it is observed that there is an overall increase in $(Ti\text{-}O)_{eq}$ and $(Ti\text{-}O)_{ax}$ bond distances in doped samples with respect to pristine sample, which can be attributed to the dominant effect of nitrogen occupying the interstitial position. Ceotto et al. have shown that, when the nitrogen goes to interstitial position the axial bond lengths elongate as observed in the present study, corroborating the claim that the nitrogen prefers interstitial position over substitutional.

3.7 Conclusion

Nano-structured pristine and N-doped TiO_2 thin films were synthesized using a cost effective and environmental friendly spray pyrolysis technique at 400, 450, 500 and 550 °C. Morphological and crystallographic studies of the films confirmed formation of well defined crystalline grains of anatase phase. Nitrogen concentration of the films were calculated from X-ray photoelectron spectra. It was observed that the maximum nitrogen concentration that we could obtain is 9%. However, this did not lead to any band gap narrowing as observed from UV-Vis spectroscopy. The location of the nitrogen dopant was deduced using two complimentary techniques such as XPS and XAS. In addition, the exact location of nitrogen in the TiO_2 host lattice in the thin films was found to be at non lattice point from the extended x-ray absorption fine structure. The average Ti-O axial and Ti-O equatorial distances in pristine TiO_2 and their changes on N-doping, corresponding to different nitrogen concentrations, were calculated from the EXAFS results. The Ti-O bond distances for the films synthesized at 450 and 500 °C are in good agreement with those evaluated using the DFT calculated Ti-O bond distances, for various configurations, given in the literature. The relatively small disparity in case of 400 °C needs further investigations to be made. The effect of reduced dimensionality in case of thin films was elucidated by analysing the near edge features. The change in transition probability due to particle size leading to increase in intensity of A_2 peak is not pronounced in the thin films. The effect of film thickness was evident from the rapidly decaying tail and the sharp absorption step for the thin films synthesized at 500 °C.

Bibliography

[1] Shaham-Waldmann, N.; Paz, Y. Modified Photocatalysts, Photocatalysis and Water Purification. *Wiley-VCH Verlag GmbH & Co. KGaA*, **2013**, 103.

[2] Richards, B. S. Comparison of TiO_2 and other Dielectric Coatings for Buried-contact Solar Cells: a Review. *Progress in Photovoltaics: Research and Applications.* **2004**, *12*, 253.

[3] Panjawi, N.; Naik, A.; Warwick, M. E. A.; Hyett, G.; Binions, R. The Preparation of Titanium Dioxide Gas Sensors by the Electric Field Assisted Aerosol CVD Reaction of Titanium Isopropoxide in Toluene. *Chem. Vap. Deposition.* **2012**, *18*, 102.

[4] Miyauchi,M.;Kieda,N.;Hishita,S.; Mitsuhashi,T.; Nakajimam,A.; Watanabe,T.; Hashimoto,K. Reversible Wettability Control of TiO_2 Surface by Light Irradiation. *Surface Science.* **2002**, *511*, 401.

[5] Muranyi, P.; Schraml, C.; Wunderlich, J. Antimicrobial Efficiency of Titanium Dioxide-Coated Surfaces. *J. Appl. Microbiol.* **2010**, *108*, 1966.

[6] Serpone, N. Is The Band Gap of Pristine TiO_2 Narrowed by Anion- and Cation-Doping of Titanium Dioxide in Second-Generation Photocatalysts? *J. Phys. Chem. B.* **2006**, *110*, 24287.

[7] Sathish, M.; Viswanathan, B.; Viswanath, R. P.; Gopinath, C. S. Synthesis, Characterization, Electronic Structure, and Photocatalytic Activity of Nitrogen-Doped TiO_2 Nanocatalyst. *Chem. Mater.* **2005**, *17*, 6349.

[8] Mrowetz, M.; Balcerski, W.; Colussi, A. J.; Hoffmann, M. R. Oxidative Power of Nitrogen-Doped TiO_2 Photocatalysts under Visible Illumination. *J. Phys. Chem. B.* **2004**, *108*, 17269.

[9] Cong, Y.; Zhang, J.; Chen, F.; Anpo, M. Synthesis and Characterization of Nitrogen-Doped TiO_2 Nanophotocatalyst with High Visible Light Activity. *J. Phys. Chem. C.* **2007**, *111*, 6976.

[10] Tian, H.; Hu, L.; Zhang, C.; Liu, W.; Huang, Y.; Mo, L.; Guo, L.; Sheng, J.; Dai, S. Retarded Charge Recombination in Dye-Sensitized Nitrogen-Doped TiO_2 Solar Cells. *J. Phys. Chem. C.* **2010**, *114*, 1627.

[11] Raut, N. C.; Mathews, T.; Ajikumar, P. K.; George, R. P.; Dash, S.; Tyagi, A. K.Sunlight Active Antibacterial Nanostructured N-doped TiO_2 Thin Films Synthesized by an Ultrasonic Spray Pyrolysis Technique. *RSC Adv.* **2012**, *2*, 10639.

[12] Sreemany, M.; Sen, S. A Simple Spectrophotometric Method for Determination of the Optical Constants and Band Gap Energy of Multiple Layer TiO_2 Thin Films. *Materials Chemistry and Physics.* **2004**, *83*, 169.

[13] Asahi, R.; Morikawa, 322 T.; Ohwaki, T.; Aoki, K.; Taga, Y. Visible-Light Photocatalysis in Nitrogen-Doped Titanium Oxides. *Science.* **2001**, *293*, 269.

[14] Lee, J.-Y.; Park, J.; Cho, J.-H. Electronic Properties of N- and C-Doped TiO_2. *Appl. Phys.Lett.* **2005**, *87*, 011904(1).

[15] Chen, X.; Burda, C. The Electronic Origin of the Visible-Light Absorption Properties of C-, N- and S-Doped TiO_2 Nanomaterials. *J. Am. Chem. Soc.* **2008**, *130*, 5018.

[16] Wu, Y.; Lazic, P.; Hautier,G.; Perssonb, K. ; Ceder, G. First Principles High Throughput Screening of Oxynitrides for Water-Splitting Photocatalysts, *Energy Environ. Sci.* **2013**, *6*, 157.

[17] Saha, N. C.; Tompkins, H. G. Titanium Nitride Oxidation Chemistry: An X-ray Photoelectron Spectroscopy Study. *J. Appl. Phys.* **1992**, *72*, 3072.

[18] Di Valentin, C.; Finazzi, E.; Pacchioni, G.; Selloni, A.; Livraghi, S.; Paganini, M. C.; Gi-amello, E., N-Doped TiO_2: Theory and Experiment. *Chem. Phys.* **2007**, *339*, 44.

[19] Cao, J.; Zhang, Y.; Tong, H.; Li, P.; Kako, T.; Ye, J. Selective Local Nitrogen Doping in a TiO_2 Electrode for Enhancing Photoelectrochemical Water Splitting. *Chem. Commun.* **2012**, *48*,8649.

[20] Zhao, Z.; Li, Z.; Zou, Z. Water Adsorption and Decomposition on N/V-Doped Anatase TiO_2 (101) Surfaces. *J. Phys. Chem. C.* **2013**, *117*, 6172.

[21] Rumaiz,A. K.; Woicik,J.C.; Cockayne,E.; Lin, H.Y.; Jaffari,G.H.; Shah, S.I. Oxygen Vacancies in N doped Anatase TiO_2: Experiment and First-principles Calculations. *Appl. Phys. Lett.* **2009**, *95*, 262111.

[22] Korotin, M.A.; Zainullina, V.M. Investigation of the Influence of Nonstoichiometry and Doping with Carbon and Nitrogen on the Electronic Spectrum of Rutile by the Coherent Potential Method. *Phys. Solid State.* **2013**, *55*, 952.

[23] Wu, H.C.; Lin, Y.S.; Lin, S.W. Calculations mechanisms of visible light photocatalysis in N-doped anatase TiO_2 with Oxygen Vacancies from GGA + U Calculations, *Int. J. Photoenergy.* **2013**, *2013*, 289328.

[24] Esaka,F.; Fuuya, K.; Shimada,H.; Imamura,M.; Matsubayashi,N.; Sato,H.; Nishijima,A.; Kawana, A.; Ichimura, H.; Kikuchi, T. A Comparison of Surface Oxidation of Titanium Nitride and Chromium Nitride Films Studied by X-ray Absorption and Photoelectron Spectroscopy. *J. Vac. Sci. Technol.* **1997**, *15*, 2521.

[25] Rodriguez,J.A.; Jirsak,T.; Liu,G.; Hrbek,J.; Dvorak,J.; Maiti, A. Chemistry of NO_2 on Oxide Surfaces: Formation of NO_3 on TiO_2(1 1 0) and $NO_2 \leftrightarrow$ O Vacancy Interactions. *J. Am. Chem. Soc.* **2001**, *123*, 9597.

[26] Petala, A.; Tsikritzis,D.; Kollia,M.; Ladas, S.; Kennou, S.; Kondarides, D.I. Synthesis and Characterization of N-doped TiO_2 Photocatalysts with Tunable Response to Solar Radiation (original). *Appl. Surf. Sci.* **2014**, *305*, 281.

[27] Raut, N. C.; Mathews,T.; Ajikumar,P. K.; George, R. P.; Dash, S.; Tyagi,A. K. Sunlight Active Antibacterial Nanostructured N-doped TiO_2 Thin Films Synthesized by an Ultrasonic Spray Pyrolysis Technique. *RSC Advances.* **2012**, *2*, 10639.

[28] Tersof, I.; Tromp, R. M. Shape Transition in Growth of Strained Islands: Spontaneous Formation of Quantum Wires. *Phys. Rev. Lett.* **1993**, *70*, 2782.

[29] Gusev, E. A.; Delidovich,S. V.; Kraaovskeya, L. I.Investigation of Urotropine Thermal Decomposition Reaction in Self Generated Atmosphere by Means of Thermal Analysis method. *Thermochimica Acta.* **1985**, *93*, 21.

[30] Dreyfors, J. M.; Jones, S. B.; Sayed, Y. Hexamethylenetetramine: A Review. *J. Am. Ind. Hyg. Assoc.* **1989**, *50(11)*, 579.

[31] Chambers, S. A.; Cheung, S. H.; Shutthanandan, V.; Thevuthasan, S.; Bowman, M. K.; Joly, A. G. Properties of Structurally Excellent N-doped TiO_2 Rutile. *Chem. Phys.* **2007**, *339*, 27.

[32] Diwald, O.; Thompson, T. L.; Zubkov, T.; Goralski, E. G.; Walck, S. D.; Yates, J. T. Photochemical Activity of Nitrogen-Doped Rutile TiO_2(110) in Visible Light. *J. Phys. Chem. B.* **2004**, *108*, 6004.

[33] Cheung,S. H.; Nachimuthu,P.; Joly, A. G.; Engelhard,M. H.; Bowman, M. K.; Chambers,S. A. N Incorporation and Electronic Structure in N-doped TiO_2(110) Rutile. *Surf. Sci.* **2007**, *601*, 1754.

[34] Cheung, S. H.; Nachimuthu, P.; Engelhard, M. H.; Wang, C. M.; Chambers,S. A. N incorporation, composition and electronic structure in N-doped TiO_2(001) anatase epitaxial films grown on $LaAlO_3$(001) *Surf. Sci.*, **2008**, *602*, 133.

[35] Ohsawa,T.; Lyubinetsky,I.; Du, Y.; Henderson, M. A.; Shutthanandan,V.; Chambers, S. A. Crystallographic Dependence of Visible-Light Photoactivity in Epitaxial $TiO_{2-x}N_x$ Anatase and Rutile. *Phys. Rev. B: Condens. Matter.* **2009**, *79*, 085401.

[36] Shinn, N. D.; Tsang, K.-L. Strain-induced surface reactivity: Low Temperature Cr /W(ll 0) Nitridation. *J. Vac. Sci. Technol. A.* **1991**, *9 (3)*, 1558.

[37] Chen, H. Y.; Nambu, A.; Wen, W.; Graciani, J.; Zhong,Z.; Hanson, J. C.; Fujita, E.; Rodriguez, J. A. Reaction of NH_3 with Titania: N-Doping of the Oxide and TiN Formation. *J. Phys. Chem. C.* **2007**, *111*, 1366.

[38] Che,M.; Naccache, C. Nature Of Paramagnetic Species Produced by Oxygen Treatment of Titanium Dioxide. *Chem. Phys. Lett.* **1971**, *8*, 45.

[39] Mi,L.; Xu, P.; Wang, P. N. Experimental study on the bandgap narrowings of TiO_2 films calcined under N_2 or NH_3 atmosphere. *Appl. Surf. Sci.* **2008**, *255*, 2574.

[40] Valentin, C. Di; Pacchioni,G.; Selloni,A.; Livraghi, S.; Giamello, E. Characterization of Paramagnetic Species in N-Doped TiO_2 Powders by EPR Spectroscopy and DFT Calculations. *J. Phys. Chem. B.* **2005**, *109*, 11414.

[41] Graciani,J.; Alvarez, L. J.; Rodriguez ,J. A.; Sanz, J. F. N-Doping of Rutile TiO_2 (110) Surface. A Theoretical DFT Study. *J. Phys. Chem. C.* **2008**, *112*, 2624.

[42] Palgrave, R. G.; Payne, D. J.; Egdell, R. G. Nitrogen Diffusion in Doped TiO_2 (110) Single crystals: a Combined XPS and SIMS Study. *J. Mater. Chem.* **2009**, *19*, 8418.

[43] Oropeza, F. E.; Harmer, J.; Egdell, R. G.; Palgrave, R. G. A Critical Evaluation of the Mode of Incorporation of Nitrogen in Doped Anatase Photocatalysts. *Phys. Chem. Chem. Phys.* **2010**, *12*, 960.

[44] Takahashi, I.; Payne, D. J.; Palgrave, R. G.; Egdell, R. G. High Resolution X-ray Photoemission Study of Nitrogen Doped TiO_2 Rutile Single Crystals *Chem. Phys. Lett.* **2008**, *454*, 314.

[45] Wang, J.; Tafen, D. N.; Lewis, J. P.; Hong, Z.; Manivannan, A.; Zhi, M.; Li, M.; Wu, N. Origin of Photocatalytic Activity of Nitrogen-Doped TiO_2 Nanobelts. *J. Am. Chem. Soc.* **2009**, *131*, 12290.

[46] Nakamura, R.; Tanaka, T.; Nakato, Y. Mechanism for Visible Light Responses in Anodic Photocurrents at N-Doped TiO_2 Film Electrodes. *J. Phys. Chem. B.* **2004**, 108, 10617.

[47] Zubavichus, Y. V.; Slovokhotov, Y. L.; Nazeeruddin, M. K.; Zakeeruddin, S. M.; Grtzel, M.; Shklover, V. Structural Characterization of Solar Cell Prototypes Based on Nanocrystalline TiO_2 Anatase Sensitized with Ru Complexes. X-ray Diffraction, XPS, and XAFS Spectroscopy Study. *Chem. Mater.* **2002**, *14*, 3556.

[48] Grunes, L. A. Study of the K Edges of $3d$ Transition Metals in Pure and Oxide Form by X-ray-Absorption Spectroscopy. *Phys. Rev. B.* **1983**, *27*, 2111.

[49] Sahoo, M.; Mathews, T.; Antony, R. P.; Krishna, D. N.; Dash, S.; Tyagi, A. K. Physico-Chemical Processes and Kinetics of Sunlight-Induced Hydrophobic - Superhydrophilic Switching of Transparent N-Doped TiO_2 Thin Films. *ACS Appl. Mater. Interfaces.* **2013**, *5*, 3967.

[50] Pease, D. M. The Thickness Effect in X-ray Absorption Edges of Metals and Alloys. *Appl. Spectrosc.* **1976**, *30*, 405.

[51] Glen, G. L.; Dodd, C. G. Use of Molecular Orbital Theory to Interpret X-Ray K-Absorption Spectral Data. *J. Appl. Phys.* **1968**, *39*, 5372.

[52] Sandstrom, D. R.; Filby, R. H.; Lytle, F. W.; Greegor, R. B. Study of Ti in Solvent-Refined Coal by X-ray Absorption Spectroscopy. *Fuel.* **1982**, *61*, 195.

[53] Chen, L. X.; Rajh, T.; Wang, Z.; Thurnauer, M. C. XAFS Studies of Surface Structures of TiO_2 Nanoparticles and Photocatalytic Reduction of Metal Ions. *J. Phys. Chem. B.* **1997**, *101*, 10688.

[54] Tsutsumi, K.; Aita, O.; Ichikawa, K. X-ray Ti K Spectra and Band Structures of Oxides of Titanium. *Phys. Rev. B.* **1977**, *15*, 4638.

[55] Belli, M.; Scafati, A.; Bianconi, A.; Mobilio, S.; Palladino, L.; Reale, A.; Burattini, E. X-ray Absorption Near Edge Structures (XANES) in Simple and Complex Mn Compounds. *Solid State Commun.* **1980**, *35*, 355.

[56] Bair, R. A.; Goddard, W. A. *Ab initio* Studies of the X-ray Absorption Edge in Copper Complexes. I. Atomic Cu^{2+} and Cu(ii)Cl_2. Phys. Rev. B 1980, 22, 2767-2776.

[57] Newville, M.; Ravel, B.; Haskel, D.; Rehr, J.; Stern, E.; Yacoby, Y. Analysis of Multiple-Scattering {XAFS} Data using Theoretical Standards. *Phys. B.* **1995**, *208-209*, 154.

[58] Belver, C.; Bellod, R.; Stewart, S.; Requejo, F.; Fernandez-Garcia, M. Nitrogen-Containing TiO_2 Photocatalysts: Part 2. Photocatalytic Behavior under Sunlight Excitation. *Appl. Catal. B.* **2006**, *65*, 309.

[59] Ceotto, M.; Lo Presti, L.; Cappelletti, G.; Meroni, D.; Spadavecchia, F.; Zecca, R.; Leoni, M.; Scardi, P.; Bianchi, C. L.; Ardizzone, S., About the Nitrogen Location in Nanocrystalline N-Doped TiO_2: Combined DFT and EXAFS Approach, *J. Phys. Chem. C.* **2012**, *116*, 1764.

Chapter 4

Synthesis and Structural Studies of Oxygen deficient TiO_2(TiO_{2-x}).

4.1 Introduction

It is well known that introduction of an anion in titanium dioxide lattice results in creation of oxygen vacancy so as to maintain charge neutrality. In particular, in the case of nitrogen doped TiO_2, three oxygen atoms are replaced for every two nitrogen atoms, thereby creating one oxygen vacancy per formula unit. In addition to the above, intrinsic oxygen vacancies are known to be present in oxide materials. Since, creation of oxygen vacancy is concurrent effect, it is pertinent to assess the effect of oxygen vacancy on the structural and electronic properties of TiO_2 comprehensively when oxygen vacancies are introduced in a controlled manner. In addition, a possible disadvantage of N-doping is that at high level of N-doping, the charge carrier recombination rate also increases.[1] hence, it is advantageous to make TiO_2 visible light active by creating oxygen vacancies without external doping. In the light of this, researchers in the last decade have focused mainly on the effect of oxygen vacancies on electronic, optical, adsorption and photocatalytic properties of TiO_2, with little attention to the effect on local structure of TiO_2. This chapter focuses on the synthesis of oxygen deficient TiO_2 thin films and the effect of oxygen vacancy on the local structure by using X-ray absorption spectroscopy (XAS). Among other techniques for detection of oxygen vacancies, Raman Spectroscopy,[2] X-ray Photo electron Spectroscopy(XPS),[3,4] Electron Spin Resonance Spectroscopy,[5] and Transmission Electron Microscopy have been widely used. Inherent methodology used for data acquisition and sample handling using these tools, limit their use in pin pointing the location and local structure around oxygen vacancies. Moreover, the scope of these techniques also act as an impediment to probe beyond the presence of oxygen vacancies. In addition to the techniques spelt above, several indirect methods, such as temperature programmed desorption have also been employed to detect oxygen vacancies. For example, in ref.[6], CO_2 has been used as a probe molecule to study the extent of oxidation/reduction of surface from adsorption/desorption behaviour of CO_2.[6] Although several direct and indirect techniques address the issue of oxygen vacancy, the associated changes introduced in local structure with the creation of oxygen vacancies is best addressed by XAS. The added advantage of XAS is that the samples can be used in all the physical forms, viz., powder, thin films and liquids. The measurements in the present study were carried out in ambient condition.

Synthesis of Oxygen Deficient Anatase TiO_2 :

In general, oxygen deficient TiO_2 is synthesized by utilizing one of the following methods as described in literature viz. thermal treatment, annealing under high vacuum and high temperature conditions, high energy particle bombardment, thermal treatment under oxygen depleted condition, doping with metal or nonmetal ions and oxygen vacancy generation under reaction condition.[7] All methods mentioned above have their own pros and cons.

It is shown by Pan *et al.* that in the case of high energy particle bombardment with electrons, oxygen vacancies are generated at the surface. However, it is a reversible process, where oxygen deficient surfaces restructure to the pristine sample at a very low temperature. Alternatively, when argon ions are bombarded on the surfaces, it effectively generates permanent and irreversible oxygen vacancies. However, this method is known to create bombardment related surface damages. Methods such as doping with metal/nonmetal ions or reactive conditions for creation of oxygen vacancy inserts unintended dopants and chemical contaminants in the lattice.

Hence, a simple method of vacuum annealing/annealing under hydrogen atmosphere was chosen in the present study for creating oxygen vacancies.[6,8]

An important fact that needs to be borne in mind while choosing the method of synthesizing oxygen deficient TiO_2 is its phase purity. This is an essential prerequisite for a credible XAS analysis, owing to the restrictions on number of free variables (Nyquist theorem limits the number of free variables) during the fitting of extended X-ray absorption spectra.[9,10] However, it has been shown conclusively in Chapter 3 that the custom made spray pyrolysis unit used in the present study indeed yields phase pure anatase films. Therefore, phase pure anatase TiO_2 films that were synthesized by spray pyrolysis technique are annealed in vacuum/H_2 environment to create oxygen deficient TiO_2 films. Owing to difficulties in annealing under hydrogen environments (extensive safety precautions are needed to handle H_2), most of the oxygen deficient TiO_2 are synthesized by annealing in vacuum. However, for the sake of completeness, XAS studies of few samples synthesized in H_2 environment are also included in this chapter.

It has been found in Chapter 3 that TiO_2 thin films synthesized by the custom made spray pyrolysis unit at T_s = 450 and 500 °C are crystalline, phase pure and nearly stoichiometric. Hence, in this work TiO_2 films synthesized at T_s = 450 and 500 °C are considered and synthesized for delineating the role of synthesis temperature on the creation of oxygen vacancies. The above synthesized films were then annealed in vacuum (at $T = T_s$ of the respective film)/ under hydrogen flow in a CVD chamber.

The base pressure of the chamber was kept at 10^{-3} mbar for the vacuum annealed films. The vacuum annealing of the films were carried out for t = 2, 4, 6 and 8 hours. When the films were annealed under hydrogen flow, the pressure of the chamber was kept at 10^{-1} mbar.

4.2 Crystallographic studies

It is known from the literature that high temperature annealing under reductive atmosphere (vacuum as well as under H_2 gas flow) may lead to phase transformation from anatase to rutile.[11] Hence, crystallographic studies were carried out to ascertain the phase purity of the films after annealing in vaccum/under H_2 flow. The GIXRD patterns of these films are given in figure 4.1 and only peaks pertaining to anatase phase are observed. No peaks pertaining to rutile could be discerned, thus confirming the phase purity of the films.

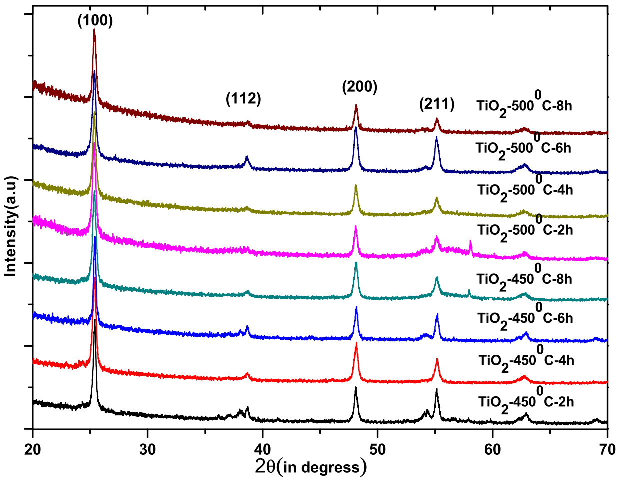

Figure 4.1 – GIXRD pattern of TiO_{2-x} thin films synthesized at 450 °C and 500 °C subsequently annealed for 2, 4, 6 and 8 hours respectively in vacuum.

The stability of anatase phase is attributed to various factors in the literature. The factors affecting the crystal structure of TiO_2 includes the preparation method, crystallite size and synthesis temperature.[12] The following factors are responsible for the stabilisation of anatase phase in the present case; (a) synthesis temperature (T_s), i.e., 450 and 500°C, which is below the critical temperature described in the literature, (b) the nano-sized crystallites which are nearly 50 nm (c) the reduced dimension in vertical direction as all the films have thickness between 100 to 150 nm and (d) use of Si (100) substrate.

4.2.1 Microstructure

The evolution of microstructure of vacuum annealed films with annealing hours is given in figure 4.2 and figure 4.3. It is seen from figure 2 that the films annealed at T_s = 450 °C undergo surface morphological changes as the annealing time is increased from 2h to 8h. The films annealed for 2h has hazy leafy grains, which becomes well defined and dense upon annealing for more hours. In case of the films annealed at T_s = 500 °C (Fig 3), there is no change in the grain shape, though change in grain density is observed for the films annealed at 6 and 8 hours.

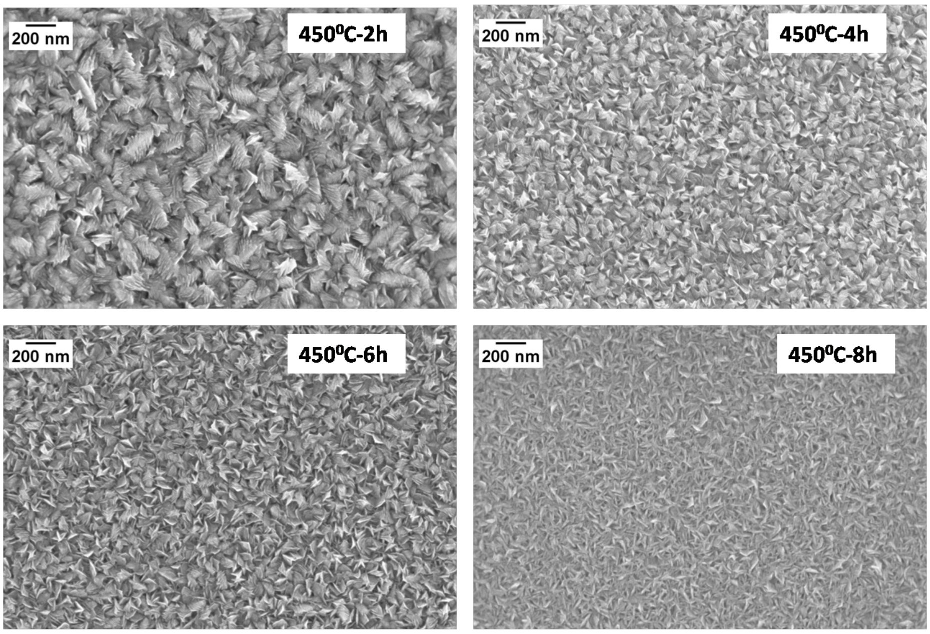

Figure 4.2 – FESEM Micrograph of TiO_{2-x} thin films synthesized at 450 °C and subsequently annealed for 2h, 4h, 6h and 8h in vacuum.

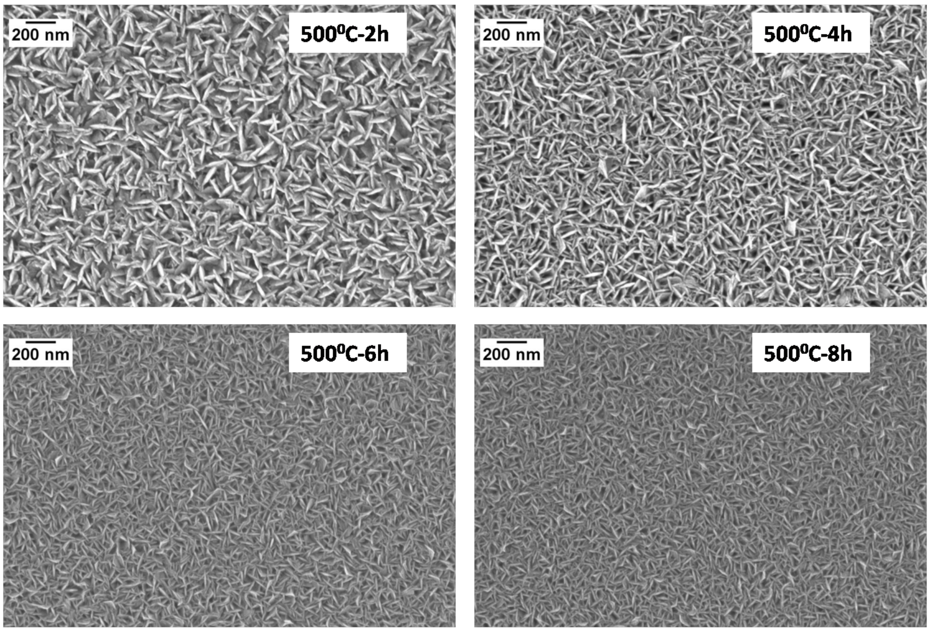

Figure 4.3 – FESEM Micrograph of TiO_{2-x} thin films synthesized at 500 °C and subsequently annealed for 2h, 4h, 6h and 8h in vacuum.

4.3 XAS studies of vacuum annealed anatase TiO_2 films

Extended region of the XAS spectra are analysed using the methodology described in Chapter 2. Since anatase phase consists of distorted TiO_6 octahedra, oxygens of TiO_6 octahedra are divided into two types of oxygen, i.e., 4 equatorial oxygens ($(\text{Ti-O})_{eq}$ represented as Ti-O1), 2 axial oxygens ($(\text{Ti-O})_{ax}$ represented as Ti-O2). A schematic of a TiO_6 octahedron differentiating between Ti-O1 and Ti-O2 bonds is shown in figure 4.4. Four paths spanning over two co-ordination spheres, viz. Ti-O1, Ti-O2 paths from first co-ordination sphere and two Ti-Ti paths from the immediate co-ordination sphere are considered for fitting the experimental data with FEFF generated model(from ARTEMIS).[13] Presence of carbon dopant owing to the decomposition of Titanium oxyacetylacetonate is delineated by using an additional Ti-C path while fitting the experimental data. Each path have four path parameters $({S_0}^2, \Delta r, \Delta E_0, \sigma^2)$ and only the single scattering paths are included in the analysis, since the rank of multiple scattering paths are very low. The number of free variables are always kept below the upper limit set by Nyquist theorem ($N_{free} = 2\Delta k \Delta r/\pi + 1$) by assuming the same E_0 and ${S_0}^2$ parameters for all paths. The goodness of the fit is measured by minimizing a statistical parameter R factor described in Chapter 2.

The fit results of Ti-C path is not reported in the tables for the following reason. It is known that TiC crystallises only in cubic phase, which mandates that a Ti-C path from a cubic space group is considered for generation of Ti-C scattering path for fitting purpose. Hence, Ti-C path generated by using fm-3m space group in FEFF is used for fitting. The position of this Ti-C path lies in the the first coordination shell (at 2.16 Å) of the anatase and is shown in figure 4.5 along with the two Ti-O paths of anatase TiO_2 structure. Since, the position of Ti-C path is at the first coordination shell, the fitting is done along with Ti-O paths by considering weighted average of both Ti-O paths and Ti-C path. Contribution of Ti-O path is taken as x and Ti-C path as 1-x during fitting. The initial value of x is taken as 0.5 with the assumption that 50% contribution comes from each structure. The value of x is found out to be 0.9996, which indicates zero contribution of Ti-C path to the first coordination shell. The fitting contributions of Ti-C path and Ti-O paths in the first coordination shell is given in figure 4.6, which confirms the absence of carbon dopant in the films.

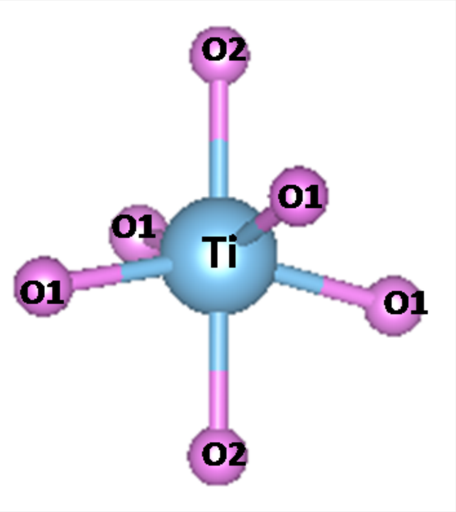

Figure 4.4 – Schematic of TiO_6 octahedron showing Ti-O1 and Ti-O2 bonds.

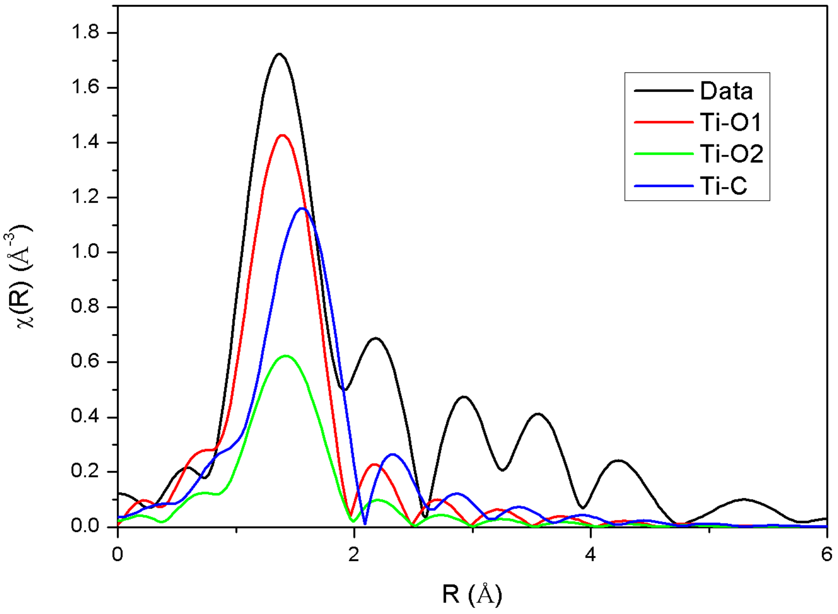

Figure 4.5 – Ti-O and Ti-C paths along with the spectra of oxygen deficient TiO_2 thin film in R-space .

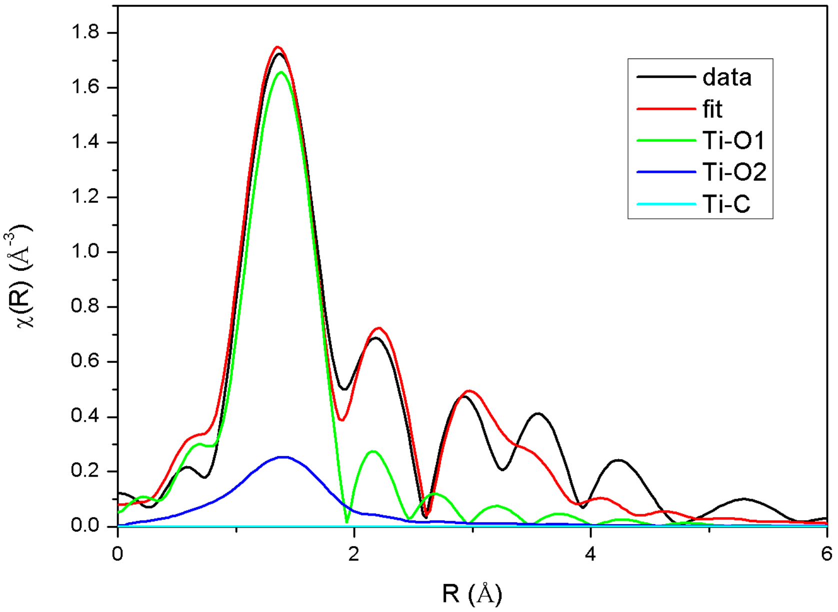

Figure 4.6 – Extended region fitting of Ti-O and Ti-C paths with the spectra of oxygen deficient TiO_2 thin film in R-space .

4.3.1 EXAFS Analysis

The fitted curves excluding Ti-C path for the films synthesized at T_s = 450, 500 °C in R-space/k-space is given in (figure 4.7, figure 4.9) / (figure 4.8, figure 4.10), respectively. The results of the fitting are given in table 4.1 and 4.2.

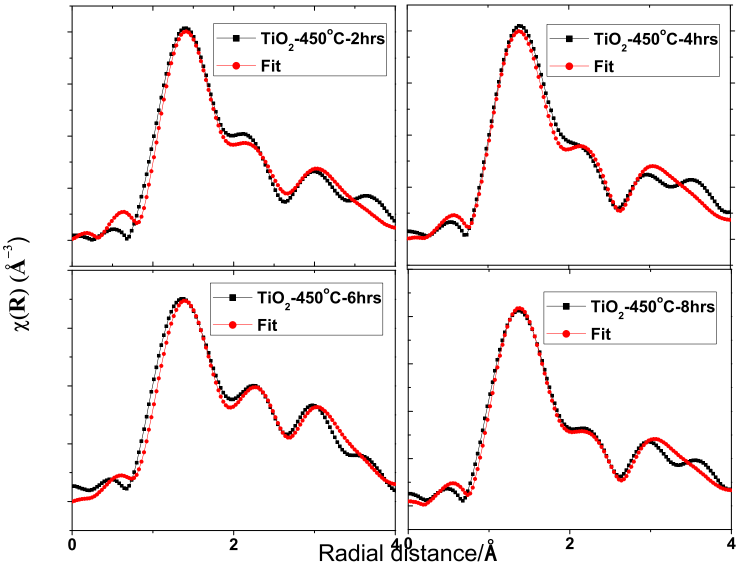

Figure 4.7 – Extended Region fitting of oxygen deficient TiO_2 450 °C thin films in R-space.

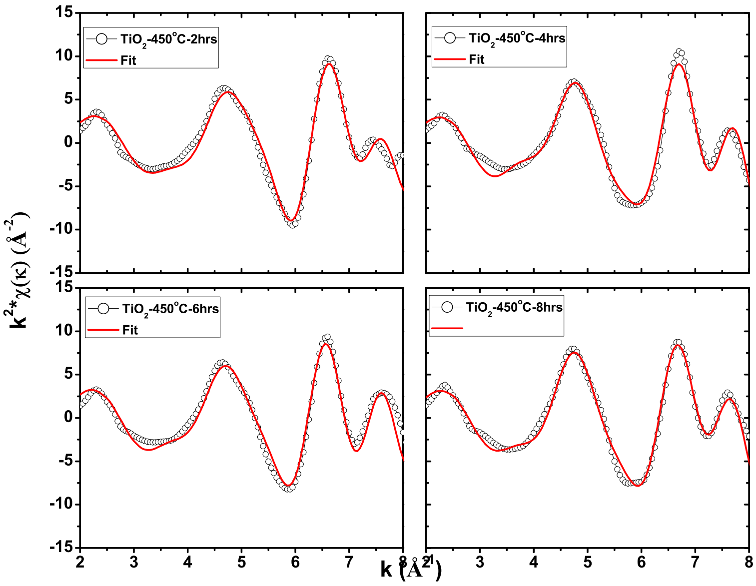

Figure 4.8 – Extended Region fitting of oxygen deficient TiO_2 450 °C thin films in k-space.

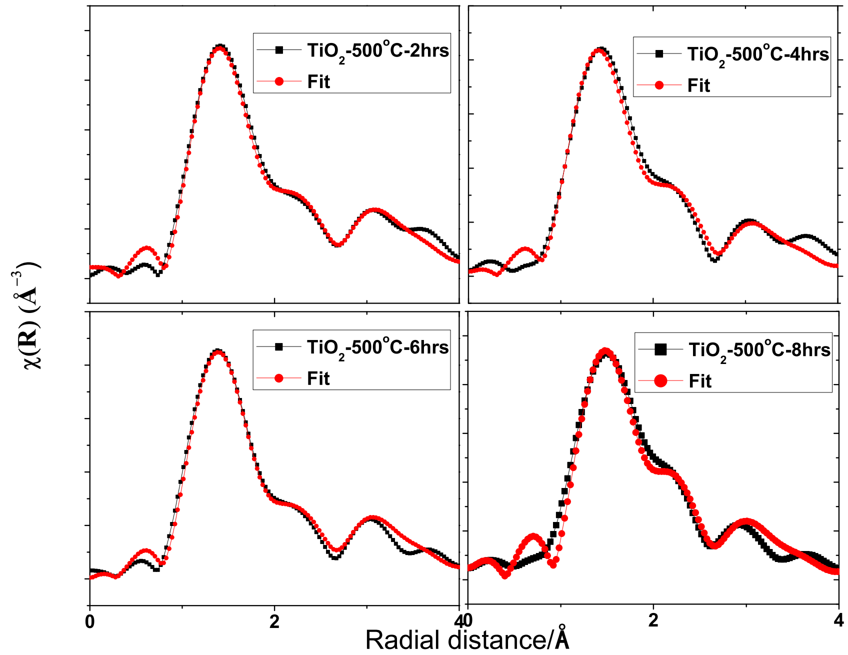

Figure 4.9 – Extended Region fitting of oxygen deficient TiO_2 500 °C thin films in R-space.

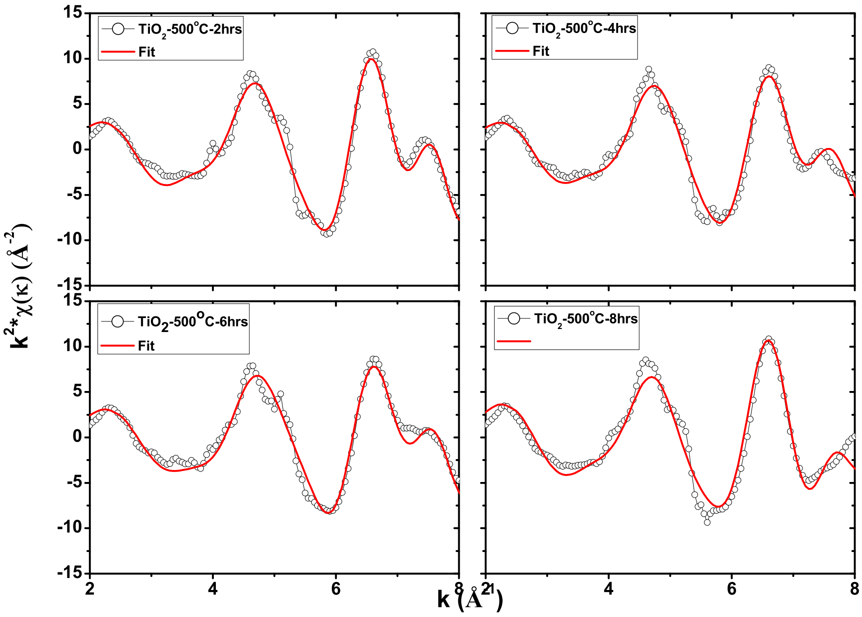

Figure 4.10 – Extended Region fitting of oxygen deficient TiO_2 500 °C thin films in k-space.

Table 4.1 – Fitted path parameters for the TiO_2 450 °C thin films

Sample id	Paths	Bond length (Å)	C.N($N * {S_0}^2$)	σ^2 (Å)^2	R
$TiO_2$450 °C-2h	Ti-O1	1.92(1)	3.32(1)	0.001(1)	0.02
	Ti-O2	1.86(1)	1.56(2)	0.02(5)	
	Ti-Ti	2.94(3)	4.0(7)	0.008(2)	
	Ti-Ti	3.77(2)	4.0(1)	0.005(3)	
$TiO_2$450 °C-4h	Ti-O1	1.92(1)	3.26(1)	0.0010(5)	0.02
	Ti-O2	1.98(2)	1.480(4)	0.02(2)	
	Ti-Ti	2.9(3)	3.21(2)	0.007(3)	
	Ti-Ti	3.72(1)	3.02(8)	0.001(1)	
$TiO_2$450 °C-6h	Ti-O1	1.91(1)	3.05(3)	0.006(1)	0.02
	Ti-O2	1.920(3)	1.66(6)	0.03(2)	
	Ti-Ti	2.96(4)	3.60(4)	0.0060(3)	
	Ti-Ti	3.78(5)	4.0(1)	0.0040(2)	
$TiO_2$450 °C-8h	Ti-O1	1.87(1)	2.84(3)	0.001(1)	0.01
	Ti-O2	1.980(3)	1.80(6)	0.001(2)	
	Ti-Ti	2.950(2)	2.88(4)	0.0060(3)	
	Ti-Ti	3.74(1)	4.0(1)	0.0040(2)	

Table 4.2 – Fitted path parameters for the TiO_2 500 °C thin films.

Sample id	Paths	Bond length (Å)	C.N($N * {S_0}^2$)	σ^2 (Å)^2	R
$TiO_2$500 °C-2h	Ti-O1	1.92(1)	2.88(1)	0.001(1)	0.02
	Ti-O2	1.98(5)	1.72(2)	0.001(5)	
	Ti-Ti	2.98(3)	4.38(7)	0.009(2)	
	Ti-Ti	3.79(2)	3.53(1)	0.003(3)	
$TiO_2$500 °C-4h	Ti-O1	1.95(1)	2.91(1)	0.001(5)	0.01
	Ti-O2	1.88(2)	1.56(4)	0.003(2)	
	Ti-Ti	2.97(3)	3.09(2)	0.005(3)	
	Ti-Ti	3.76(1)	4.8(8)	0.011(1)	
$TiO_2$500 °C-6h	Ti-O1	1.92(1)	3.24(3)	0.001(1)	0.01
	Ti-O2	1.93(3)	1.8(6)	0.02(2)	
	Ti-Ti	2.960(2)	3.01(4)	0.0070(3)	
	Ti-Ti	3.780(4)	4.4(1)	0.0080(2)	
$TiO_2$500 °C-8h	Ti-O1	1.96(1)	3.88(3)	0.001(1)	0.01
	Ti-O2	1.76(1)	1.85(4)	0.013(2)	
	Ti-Ti	2.94(2)	2.94(1)	0.004(3)	
	Ti-Ti	3.75(4)	4.92(1)	0.009(2)	

From table 4.1 (and table 4.2) it is observed that the Ti-O co-ordination number for films synthesized at T_s = 450 °C (500 °C) and annealed for t = 2 to 8 hours varies as 4.88, 4.74, 4.71, 4.64 (4.6, 4.5, 5.04, 5.73), respectively, which are less than the ideal value of 6. It is also observed that the Ti-O co-ordination number decreased linearly (4.88 to 4.64) with increasing vacuum annealing time (from 2 to 8 hours) for the films synthesized at $T_s = 450$ °C. This matches with the findings of Salari *et al.*[11] However, for films synthesized at $T_s = 500$ °C, though the overall co-ordination number is less than the ideal value of 6, it increases as the annealing hours increase from 4 to 8 hours (4.6, 4.5, 5.04, 5.73 as seen in table 4.2). This is attributed to the porous microstructure of the films synthesized at $T_s = 500$°C (figure 4.3), which become dense when annealed for a longer period such as 6 and 8 hours. Hence, it is proposed that longer annealing hours facilitate rearrangement of the dangling bonds with oxygen at the surface, leading to a minute increase in the co-ordination number for films annealed for 6 and 8 hours, respectively. In addition, it is known that oxygen absorption and desorption is a reversible process during thermal treatment.[7] Krivtsov *et al.* proposed that presence of oxygen vacancy in the matrix can cause charge imbalance in the TiO_2 cell, which tend to be compensated by several mechanisms, such as by reduction of Ti^{4+} to Ti^{3+}, Ti^{2+} or by trapping of oxygen species from the environment.[14] In the present study, the observed co-ordination number increase for films annealed at 6h and 8h point towards absorption of desorbed oxygen species available near the surface.[14]

The formation of oxygen vacancy upon vacuum annealing is also confirmed by comparing the co-ordination numbers obtained from table 4.1 and 4.2 with the co-ordination number calculated by using Frenkel formula, which utilises the crystallite size of the films.[15] Frenkel *et al.* have studied the effect of structural disorder and structural/compositional heterogeneity in nanoparticles on the co-ordination number and deduced a formula for calculating the co-ordination number in nanoparticles, which is given in the following equation:[15,16]

$$n_{nano} = [1 - \frac{3}{4}(\frac{r}{R}) + \frac{1}{16}(\frac{r}{R})^3]n_{bulk} \tag{4.1}$$

where, r is the distance between the nearest-neighbor atoms and R is the crystallite size, n_{bulk} is the ideal co-ordination number for TiO_6 octahedron. Crystallite size of the films studied in this study are calculated using Scherrer formula and ranges from 29 to 91 nm (given in table 4.3).The co-ordination number for the particular crystallites calculated using equation 4.1 is given in table 4.3.

Table 4.3 – Crystallographic parameters and calculated co-ordination number.

Sample id	Crystallite Size (in nm)	Calculated Co-ordination number	Crystallographic cell parameter	Volume($\mathring{A}^3$)
$TiO_2$450 °C-2h	29	5.94	a=3.7842(2)	
			c=9.4907(9)	135.9093(6)
$TiO_2$450 °C-4h	57	5.96	a=3.7801(0)	
			c=9.5263(1)	136.1231(1)
$TiO_2$450 °C-6h	42	5.95	a=3.7827(4)	
			c=9.4795(9)	135.6452(9)
$TiO_2$450 °C-8h	30	5.94	a=3.7794(2)	
			c=9.4651(8)	135.0648(6)
$TiO_2$500 °C-2h	55	5.96	a=3.7775(1)	
			c=9.4657(9)	135.0735(7)
$TiO_2$500 °C-4h	26	5.93	a=3.7789(3)	
			c=9.4670(0)	135.1922(7)
$TiO_2$500 °C-6h	91	5.98	a=3.7806(3)	
			c=9.5077(4)	135.8959(6)
$TiO_2$500 °C-8h	62	5.98	a=3.7809(7)	
			c=9.5001(8)	135.8120(7)

It is observed from table 4.3 that the co-ordination number should be ∼ 5.9 for the films studied in the present study. Hence, the co-ordination number observed in Table 4.1 and Table 4.2, which is less than 5.9, is indicative of the oxygen deficiency induced in the TiO_2 thin films due to vacuum annealing and is not due to nano sized crystallites.

Furthermore, to ascertain the presence of oxygen vacancy, crystallographic parameters (a and c) and cell volume has been calculated from the GIXRD spectra by using PCW and is listed in table 4.3.

Presti *et al.* have calculated the cell parameters (a and c) and cell volume by using PAW, LCGTF and different potentials (table S4 of Presti *et al.*).[17] The cell volume of ideal TiO_2 cell calculated by them using different methods are found out to be 144.3, 137.1, 138.2 ,140.8 $\mathring{A}^3$ and oxygen deficient TiO_2 cell are found out to be 144.0, 136.0, 138.1, 140.0 Å^3. The calculated cell volumes i.e. $\sim$ 136.0 Å^3 for the films in the present study matches with the cell volume of oxygen deficient TiO_2 calculated by Presti *et al.* This corroborates the finding from EXAFS analysis regarding the formation of oxygen vacancies.

Moreover, Ceotto *et al.* have calculated the Ti-O bond distances for oxygen defected octahedron. They considered axial, equatorial oxygen vacancy and calculated the bond distances for other Ti-O bonds using PAW-DFT. The PAW-DFT calculated bond distances of oxygen defected octahedron (from the table 2 of Ceotto *et al.*[9]) varies like V_O/1.86/1.93/1.92/1.90/1.90 Å and 1.92/1.96/V_O/1.81/1.92/1.91 Å for axial and equatorial oxygen vacancy respectively. The PAW-DFT calculated Ti-O1 and Ti-O2 bonds have average values of 1.86Å , 1.91Å and 1.94Å , 1.88Å for octahedra with axial and equatorial vacancy, respectively.[9] Since, XAS gives the average value of several defected octahedra, the bond lengths(Ti-O1 and Ti-O2) represented in Table 4.1 and 4.2 matches with the PAW-DFT calculated values.[9]

4.4 Analysis of X-ray Absorption Near Edge Spectra (XANES)

In this section the near edge features which is 20 eV below the Ti K-edge is discussed. Near edge features contain information regarding the electronic transitions in a system. In the present work TiO_{2-x} thin films have been synthesized, wherein oxygen vacancies have been deliberately introduced into the matrix to study it's effect on the local co-ordination and electronic properties. Introduction of oxygen vacancy into the matrix of TiO_2 lead to many changes like change of Ti^{4+} oxidation state to Ti^{3+}[18] and distortion in the local TiO_6 co-ordination. Distortion in TiO_6 octahedron could be due to elongation or shortening of Ti-O bond lengths. Change in Ti-O bond length leads to change in Ti 3d and O 2p density of states(DOS). This alters the titanium-oxygen orbital overlap, thus affecting the total DOS and its corresponding electronic transitions are reflected in the pre-edge features. The effect of oxygen vacancy on the co-ordination number is already explained in the previous section by analysing the extended X-ray absorption fine structure, in this section the effect of oxygen vacancy on the near edge-spectral features is discussed.

Theoretical background of XANES and it's application to the distorted octahedra of anatase (TiO_{2-x} Films)

The number of pre-edge peaks and its broad features i.e. occurence of A_1, A_2, A_3 peaks and B peaks are similar in both rutile and anatase phase of TiO_2 as shown by Grunes *et al.* and Sandstrom *et al.*[19,20] Since, symmetry of TiO_6 octahedron is reduced from O_h due to distortion in both rutile and anatase, it can be safely presumed that the effect of the distortion on the pre-edge features will also follow the same trend and can be compared with each other.[21] Hence, in this section the pre-edge features pertaining to anatase TiO_2 is compared with the literature of rutile phase.[24,25] In addition, FEFF calculation for pristine anatase and oxygen deficient anatase phase is also discussed.

It is known that x-ray absorption near edge structures(XANES) are signature of the co-ordination around central metal atom. The pre-edge features are traditionally described by using Molecular orbital theory or solid state band theory. According to Molecular orbital theory(MOT), XANES arises due to electronic transitions in the molecular orbitals.[19] MOT is inherently symmetry dependent. In case of TiO_2 anatase, the pre-edge peaks are due to weak quadrupole $1s \rightarrow 3d$ transitions. Though this interpretation is still used widely, sophisticated solid state band theory indicates that these transitions arises due to O $2p$ - Ti $3d$ mixing rather than the dipole forbidden $1s$-$3d$ transitions. Since, p-d mixing is dependent on the orientation of orbitals, symmetry around the central metal atom plays a crucial role while explaining the pre-edge peaks. It has been amply proven in the literature that p-orbitals offer necessary symmetry and energetic adequacy to undergo p-d mixing when the symmetry of the octahedral centres break down to lower symmetry.

In case of anatase TiO_2, Ti is located at the center of a distorted oxygen octahedron. As a result the O_h symmetry around Ti breaks down to lower symmetry, resulting in breaking down of degeneracy of *d*-orbitals leading to effective *p*-*d* mixing.[21] The reduction in point group symmetry in the distorted octahedron allows off-diagonal matrix elements (i.e overlapping elements between different states) to become non zero, which were zero in the higher symmetry. In addition, it is known that dipole forbidden features(transitions involving *s* to orbitals with *d*-character) are angle dependent while dipole allowed (transitions involving s to orbitals arising out of p-d mixing) features are not. However, this ambiguity regarding origin of pre-edge peaks does not affect the qualitative inference about the Ti co-ordination from these pre-edge features. Moreover, since the experimental results here are compared with dipole allowed FEFF calculations, the pre-edge features will be looked from dipole allowed or dipole forbidden point of view in the present study. Hence, the origin of A_2 and A_3 peak in the pre-edge region is attributed to dipole allowed 1s-$2t_2g$ and 1s-$3e_g$ transitions in the octahedral field, respectively. The origin of A_1 peak has been ascribed to an exciton band or due to 1s to $1t_1g$ quadrupolar transition from possible perturbation due to shake-up and shake-off processes.[22]

4.4.0.1 Comparision of FEFF generated spectra with the experimentally observed spectra

XANES calculations of anatase TiO_2 is performed using the FEFF 9.6. code to study the influence of oxygen vacancies on the pre-edge features.[23] FEFF simulated X-ray absorption spectra have been generated for pure anatase, and oxygen deficient anatase by removing either an equatorial oxygen or axial oxygen from the TiO_6octahedron. The input parameters for these calculations were generated using the Atoms code provided in Artemis software of the Demeter package. The convergence of the calculation was achieved for the cluster of 80 atoms for each model. The cluster radius was decided such that adding the next coordination shells did not change the fine structure.[26] The total scattering potentials including a fully relaxed core hole were obtained iteratively by successive calculations of the potential until self consistency was reached. Based on these scattering potential, the final state of the excited photoelectron were calculated. The close match between the simulated and experimental spectra was obtained by using Hedin-Lundqvist model of exchange potential. The theoretically simulated XANES spectra is given in figure 4.11.

It is observed that FEFF (multi scattering method) calculation, which is a dipole allowed calculation reproduces two pre-edge peaks for anatase as compared to three pre-edge peaks in the experimental spectrum(A_1, A_2, A_3). This result can be attributed to the inherent failure of the multi scattering method in predicting the A_1 peak. This matches with the results of various other researchers, who could not reproduce the A_1 peak for rutile phase by using dipole allowed calculations and have attributed this peak to s - d quadrupolar transition.[24,27,28] The FEFF calculated spectrum for the structure where axial oxygen is removed, a small hump is seen on lower energy side of the A_2 peak, which matches with the isomorphous Ti-compounds with square pyramidal polyhedron(considered as the most distorted octahedron) with Ti at the center.[24]. In addition, it is observed from the FEFF calculation that all three A_1, A_2, A_3 peaks are obtained when oxygen is removed from equatorial position. This matches with the experimental spectrum in the present study as shown in figure 4.12. This is attributed to the distortion in the TiO_6 octahedron.

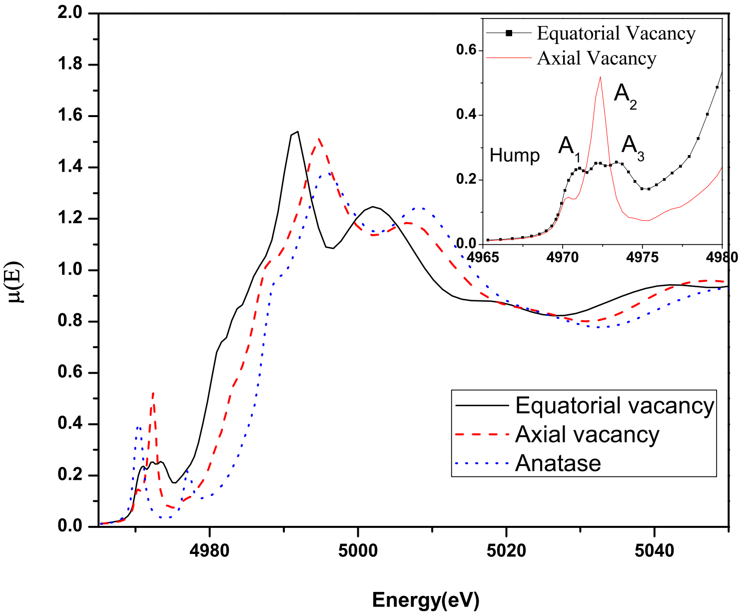

Figure 4.11 – FEFF calculated spectra of Anatase and oxygen deficient anatase with equatorial and axial vacancy.

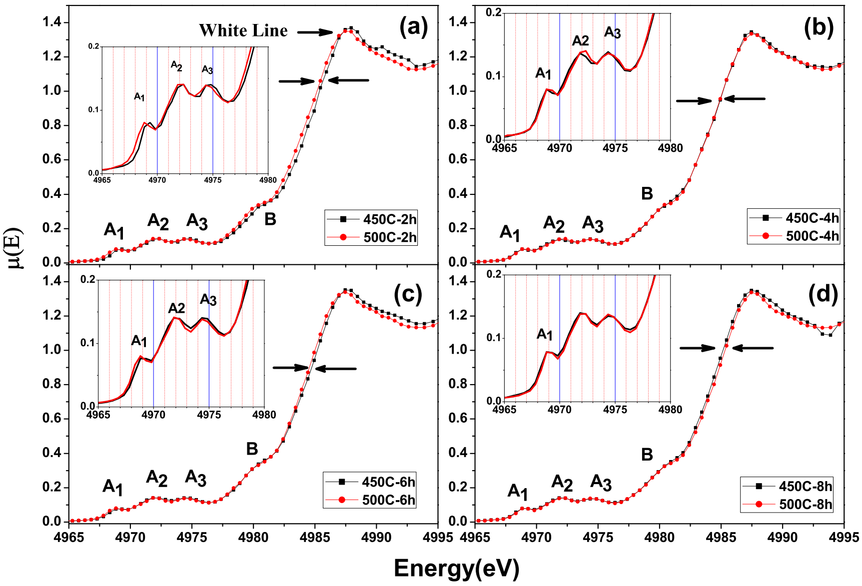

Figure 4.12 – Near edge Feature of oxygen deficient TiO_2 450 °C and TiO_2 500 °C thin films.

N.Jiang *et al.* have carried out theoretical analysis of Ti XANES for delineating the dependence of pre-edge peaks on various geometrical parameters; viz. co-ordination, symmetry, Ti-O bond length and bond angle.[24] They considered both density functional theory and real space multiple scattering (MS) method using FEFF8 program to simulate the pre-edge peaks. To understand the effect of distortion, Jiang *et al.* considered various kinds of distortion such as; i. shortening of $(\mathrm{TiO})_{ax}$ bond length (Type-I); ii. tilting the axial oxygen atom away from the axis(Type-II); iii. tilting one axial and one equatorial oxygen atom simultaneously (Type-III) and iv. Type-III + Type-I. They extended the results of the above considered distortion to rutile TiO_2 and concluded that the resultant pre-edge features appeared predominantly due to bond length variation upon introduction of a defect. Since, the p-d mixing is dependent on orbital overlapping, the bond length variation plays a major role than the bond angle variation. Hence, it is concluded that the concurrence in the pre-edge features of FEFF generated spectrum (with equatorial oxygen vacancy as shown in the inset of figure 4.11) and the experimental spectrum as shown in figure 4.12 is due to bond length distortion owing to oxygen vacancies, which is described in the following paragraph. Glen A. Waychunas has elucidated the relation between the bond length and the pre-edge peaks. He has elucidated that when the mean Ti-O bond length is higher the peak position of the pre-edge as well as the white line is shifted towards lower energy.[29] Hence,the mean bond lengths calculated from EXAFS results(table 4.1 and table 4.2) and normalised height of A_2 obtained from fitting of near-edge features of thin films in Athena is given in Table 4.4. It is seen from Table 4.4 that $TiO_2$450 °C-2h film has a lower mean bond length (1.89Å) compared to $TiO_2$500 °C-2h film (1.95Å). The effect of the bond length is reflected in the pre-edge features of both the films (figure 4.12 (a)), which shows the pre-edge features shifting towards higher energy for $TiO_2$450 °C-2h compared to $TiO_2$500 °C-2h.

Similarly,thin films annealed for 6 hours follow the same trend as that of thin films annealed for 2h as shown in figure 4.12(c). It is observed from the Table 4.4 that the films annealed for 8hours follow the reverse trend with respect to bond length i.e. $TiO_2$450 °C-8h has a mean Ti-O bond length of 1.93Å, which is higher compared to the mean Ti-O bond length (1.86 Å) of $TiO_2$500 °C-8h. This is also reflected in the figure 4.12(d), wherein the pre-edge features as well as the white line is shifted towards higher energy for $TiO_2$500 °C-8h film as compared to $TiO_2$450 °C-8h film. This observation is similar to that reported by Glenn A. Waychunas.[29] Since mean bond lengths for thin films annealed for 4h remains almost similar for both $TiO_2$450 °C and $TiO_2$500 °C, the energy shift is also negligible as seen in figure 4.12 (b).

Table 4.4 – Mean Ti-O bond length(tabulated from table 4.1 and 4.2) and integrated intensity(After fitting the pre-edge peaks of experimental spectra) of A_2 peak of $TiO_2$450 °C and $TiO_2$500 °C thin films .

Sample id	Bond length (Å)	Normalised Height(A_2)	Sample id	Bond length (Å)	Normalised Height(A_2)
$TiO_2$450 °C-2h	1.89	0.31	$TiO_2$500 °C-2h	1.95	0.31
$TiO_2$450 °C-4h	1.95	0.30	$TiO_2$500 °C-4h	1.92	0.30
$TiO_2$450 °C-6h	1.91	0.27	$TiO_2$500 °C-6h	1.93	0.29
$TiO_2$450 °C-8h	1.93	0.26	$TiO_2$500 °C-8h	1.86	0.29

Correlation of peak height and peak position.

Numerous researchers have elucidated the relation between pre-edge peak height with the Ti co-ordination number.[25,29–32] Amongst them Farges *et al.* have highlighted the influence of co-ordination and disorder on XANES quantitatively.[25] They provided a comprehensive way of understanding the pre-edge peak features using both the peak height and peak position by using FEFF 6 and FEFF 7. In particular, they have studied disordered structures containing Ti centers with varied geometries such as four, five and six co-ordinated Ti species. They adequately accommodated the disorderness in various co-ordination geometries such as short range tetrahedral, square pyramidal and octahedral symmetries by considering high order multi-scattering in small clusters, with the small cluster embedded in an appropriately chosen larger cluster needed to accurately describe the potential. Hence, their results can be suitably compared with the present study, which involves defected TiO_6 octahedra due to oxygen vacancies.

The XANES region of the X-ray absorption spectra of vaccuum annealed $TiO_2$450 °C and $TiO_2$500 °C thin films were fitted using peak fitting feature of Athena with three Gaussian peaks. The peak parameters for A_2 peak is given in the table 4.4. The edge part was simulated with arctan function.[29] Farges et al have studied mixture of four, five and sixfold co-ordinated Ti compounds and have illuciadted that peak height alone cannot be conclusively used for determination of Ti- cordination. However use of both peak height and peak position can conclusively tell about the co-ordination number (Fig 6 of Ref-23). It is observed that the A_2 pre-edge peak position is $\sim$ 4971 eV for all the TiO_{2-x} thin films and their normalised peak intensity ranges from 0.26 to 0.31. Hence, it is concluded that films consist of both six fold and few five fold co-ordinated Ti centers taking both peak position and peak height into consideration. This is evident from the co-ordination numbers calculated from the EXAFS analysis described in section 4.4.1. Since, EXAFS gives an average value of several co-ordination spheres, the co-ordination number for the films in the present study varies between 4 to 6 as seen from the EXAFS analysis. Hence, from XANES and EXAFS, it is concluded that vacuum annealing of spray pyrolysis synthesized TiO_2 films results in oxygen deficient thin films without any phase transition of the thin films. In addition to the co-ordination number, the disorderness in the TiO_6 octahedra also affect the pre-edge intensity, which is described below.

4.4.1 Discussion on pre-edge Intensity

In this section the effect of disorderness in the TiO_6 octahedra on the pre-edge intensity is discussed. It is known that the integrated intensity is a function of degree of p-d mixing, which is a result of distortion in TiO_6 octahedra in anatase TiO_2. In particular, Waychunas and Jiang et. al. observed that the effect of distortion is more pronounced in the second pre-edge peak intensity (A_2).[29,24] To understand the above effect, peak fitting results of A_2 given in Table 4.4 are analysed. The peak intensity of A_2 (in table 4.4) reveals that TiO_{2-x} thin films (for both the set of films i.e films with T_s 450 and 550 °C) annealed for 2 hours has the highest integrated intensity compared to those annealed for longer hours (4, 6 and 8 hours). This indicates decrease in disorderness with increase in annealing time. This is in accordance with the fact that grain size and crystallinity increases with increase in annealing time as seen in the literature.

In addition, it is observed from the table 4.4 that the integrated intensity of $TiO_2$450 °C thin films annealed for 6 and 8 hours is lower than their corresponding $TiO_2$500 °C thin films. This is attributed to the synthesis temperature and mechanism of the film formation, which have been described in chapter-3.[10] It is known from chapter-3 that thin films synthesized at T_s = 450 °C are stoichiometric compared to the films synthesized at T_s = 500 °C. Hence, it is concluded that the disorderness in the $TiO_2$500 °C thin films is higher owing to it's non-stoichiometry as compared to $TiO_2$450 °C thin films. This result matches with the result of the study by Jiang *et al.*, who studied several Ti-O systems and observed that integrated peak intensity increases with increasing disorderness.

4.5 XAS studies of Films reduced under Hydrogen atmosphere

As discussed in the introduction, a set of TiO_2 films were annealed under hydrogen atmosphere to understand the creation of oxygen vacancies in reducing atmosphere. Since, the experiments involved diligent care and attention for handling hydrogen gas only a few films has been synthesized and presented here for the sake of completeness. The result of the EXAFS analysis for the films reduced in hydrogen atmosphere is tabulated in Table 4.5 and the fitted plots in the R-space is shown in Fig 4.13. The first peak at 1.75 Åin fourier transform spectrum in figure 4.13 is contribution of Ti-O coordination and the second peak at 2.50 Åis contribution of Ti-Ti coordination. It is observed from the Table 4.3 that with increase in reduction time, amount of oxygen vacancies increase. The co-ordination number in the first co-ordination sphere is drastically less with just a value of 3.44 for $TiO_{2-x} - H_2 - 8hr$ compared to a value of 4.5 and 5 for the films reduced under hydrogen for 6hr and 4 hr respectively. It also reveals that the bond lengths of the Ti-O1 remains constant for $TiO_{2-x} - H_2 - 6hr$ and $TiO_{2-x} - H_2 - 4hr$ films, whereas it gets compressed to 1.91 Åfor $TiO_{2-x} - H_2 - 8hr$ films. Thus, it is concluded that maximum number of oxygen vacancies and a subsequent bond length compression is observed for $TiO_{2-x} - H_2 - 8hr$ films.

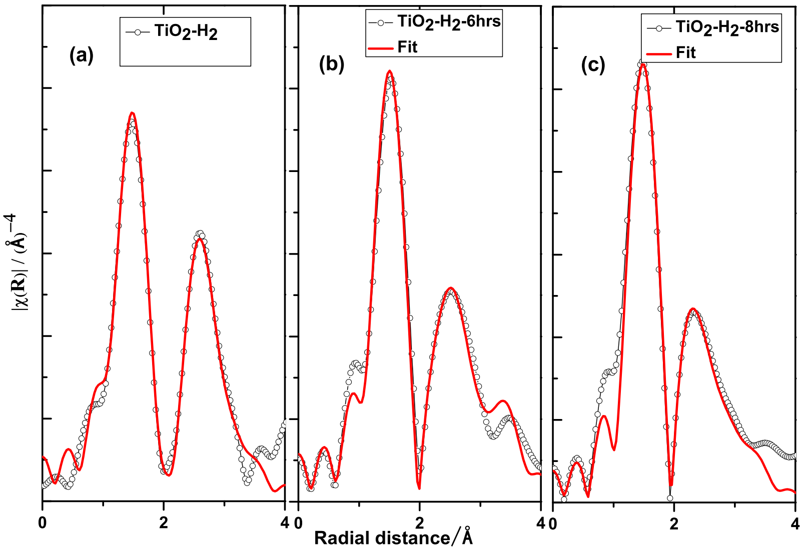

Figure 4.13 – Extended Region fitting of $TiO_{2-x} - H_2$ and $TiO_{2-x}N_x - H_2$ films.

Table 4.5 – Fitted path parameters for $TiO_{2-x} - H_2$ films

Sample id	Paths	Bond length (Å)	C.N($N * {S_0}^2$)	σ^2 (Å)^2	R
$TiO_{2-x} - H_2 - 8hr$	Ti-O1	1.91(1)	3.4(1)	0.001(1)	0.02
	Ti-O2	-	0	-	
$TiO_{2-x} - H_2 - 6hr$	Ti-O1	1.96(1)	3.3(1)	0.001(5)	0.03
	Ti-O2	1.84(2)	1.2(1)	0.003(2)	
$TiO_{2-x} - H_2\breve{\ }4hr$	Ti-O1	1.95(1)	3.6(3)	0.001(1)	0.02
	Ti-O2	1.82(3)	1.4(2)	0.001(2)	

EXAFS analysis(See figure 4.13 and table 4.5) of the films reduced under hydrogen atmosphere reveals creation of oxygen vacancies, which is reflected in the reduced co-ordination number in the first co-ordination sphere, which in turn can have pronounced effect on the local symmetry resulting in more distorted TiO_6 octahedra. The effect of the reduced co-ordination number is observed in the intensity of the pre-edge peaks. Farges *et al.* and Yamamoto *et al.* have elucidated that as the co-ordination number increases; the intensity goes down, which is also observed in the present study.[33,34] It is observed from figure 4.14 that intensity of A$_1$, A$_2$ and A$_3$ for $TiO_{2-x} - H_2 - 6hr$ and $TiO_{2-x} - H_2 - 4hr$ film is lower than $TiO_{2-x} - H_2 - 8hr$ film.

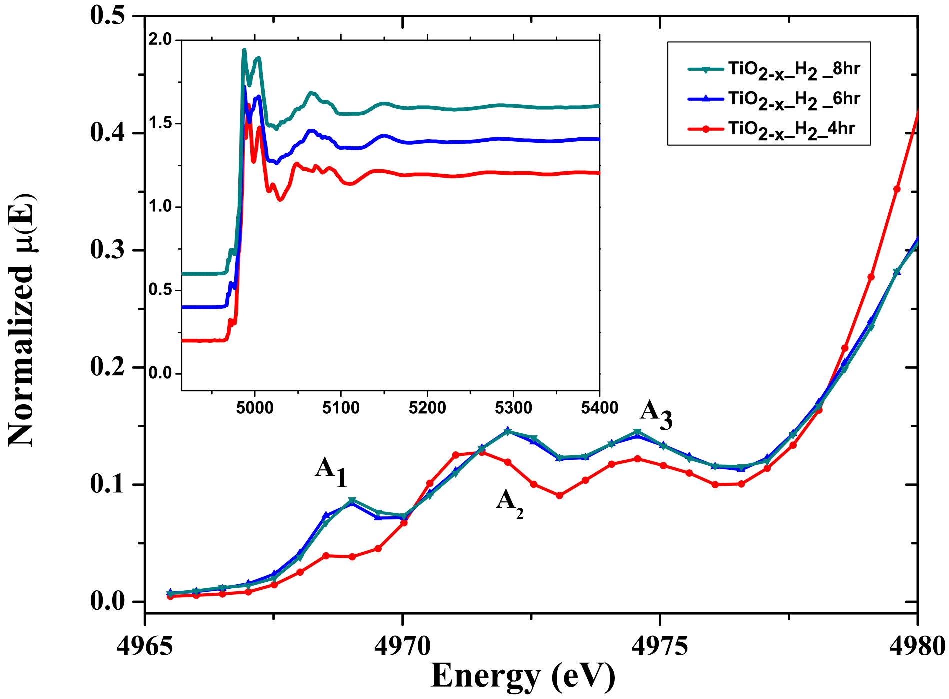

Figure 4.14 – Near edge spectra of Fourier transformed EXAFS spectra of TiO_{2-x} films synthesized by reducing under hydrogen atmosphere for a)4hr a) 6hr, b) 8hr; c) (Inset) $\mu(E)$ Vs E plot

4.6 Conclusion

In this work, a direct approach to analyze oxygen vacancies using X-ray absorption spectroscopy is illustrated. Phase pure oxygen deficient anatase thin films were synthesized using a simple two step process i.e spray pyrolysis followed by annealing in vacuum or under hydrogen atmosphere. Extended X-ray absorption features quantitatively defined the amount of oxygen vacancies and the effect of these vacancies on the bond length was suitably deduced from the XANES. The x-ray absorption near edge(XANES) features revealed qualitative information regarding the electronic transitions of these oxygen deficient TiO_2 thin films.

Bibliography

[1] Wang, J.; Tapio, K.; Habert, A.; Sorgues, S.; Colbeau-Justin, C.; Ratier, B.; Scarisoreanu, M.; Toppari, J.; Herlin-Boime, N.; Boucle, J. Influence of Nitrogen Doping on Device Operation for TiO_2 Based Solid State Dye Sensitized Solar Cells: Photo-Physics from Materials to Devices. *Nanomaterials.* **2016**, *6*, 35.

[2] Guo, M.; Lu, J. Q.; Wu, Y. N.; Wang, Y. J.; Luo, M. F. UV and Visible Raman Studies of Oxygen Vacancies in Rare-Earth-Doped Ceria. *Langmuir.* **2011**, *27*, 3872.

[3] Chen, Q. L.; Gabaly, F. E.; Akgul, F. A.; Liu, Z.; Mun, B. S.; Yamaguchi, S.; Braun, A. Observation of Oxygen Vacancy Filling under Water Vapor in Ceramic Proton Conductors in Situ with Ambient Pressure XPS. *Chem. Mater.* **2013**, *25*, 4690.

[4] Gordon, T. R.; Cargnello, M.; Paik, T.; Mangolini, F.; Weber, R. T.; Fornasiero, P.; Murray, C. B. Nonaqueous Synthesis of TiO_2 Nanocrystals Using TiF4 to Engineer Morphology, Oxygen Vacancy Concentration, and Photocatalytic Activity. *J. Am. Chem. Soc.* **2012**, *134*, 6751.

[5] Ji, W. W.; Lee, M. H.; Hao, L. Y.; Xu, X.; Agathopoulos, S.; Zheng, D. W.; Fang, C. H. Role of Oxygen Vacancy on the Photoluminescence of $BaMgSiO_4$:Eu Phosphors: Experimental and Theoretical Analysis *Inorg. Chem.* **2015**, *54*, 1556.

[6] Thompson,T. L.; Yates, J. T. Jr. TiO_2-based photocatalysis: surface defects, oxygen and charge transfer. *Topics in Catalysis.* **2005**, *35*, 197.

[7] Pan, X.; Yang, M. Q.; Fu,X.; Zhang, N.; Xu, Y. J. Defective TiO_2 with oxygen vacancies: synthesis, properties and photocatalytic applications. *Nanoscale.* **2013**, *5*, 3601.

[8] Liu, L.; Zhao,C.; Li, Y. Spontaneous Dissociation of CO_2 to CO on Defective Surface of Cu(I)/ TiO_{2-x} Nanoparticles at Room Temperature. *J. Phys. Chem. C.* **2012**, *116*, 7904.

[9] Ceotto, M.; Lo Presti, L.; Cappelletti, G.; Meroni, D.; Spadavecchia, F.; Zecca, R.; Leoni, M.; Scardi, P.; Bianchi, C. L.; Ardizzone, S., About the Nitrogen Location in Nanocrystalline N-Doped TiO_2: Combined DFT and EXAFS Approach, *J. Phys. Chem. C.* **2012**, *116*, 1764.

[10] Sahoo, M.; Yadav, A. K.; Jha, S. N.; Bhattacharyya, D.; Mathews,T.; Sahoo, N. K.; Dash, S.; Tyagi, A. K. Nitrogen Location and Ti-O Bond Distances in Pristine and N-doped TiO_2 anatase Thin Films by X-ray Absorption Studies. *J. Phys. Chem. C.* **2015**, *119*, 17640.

[11] M. Salari, K. Konstantinov ; Liu, H. K. Enhancement of the capacitance in $TiO2$ nanotubes through controlled introduction of oxygen vacancies *J.Mater.Chem.* **2011**, *21*, 5128.

[12] Chen, X.; Mao, S. S. Titanium Dioxide Nanomaterials: Synthesis, Properties, Modifications, and Applications. *Chem. Rev.***2007**, *107*, 2891.

[13] Newville, M.; Ravel, B.; Haskel, D.; Rehr, J.; Stern, E.; Yacoby, Y. Analysis of Multiple-Scattering {XAFS} Data using Theoretical Standards. *Phys. B.* **1995**, *208-209*, 154.

[14] Krivtsov,I.; Ilkaeva, M.; Salas-Colera, E.; Amghouz, Z.; Garcia,J. R.; Diaz, E.; Ordonez, S.;Villar-Rodil, S. Consequences of Nitrogen-Doping and Oxygen Enrichment on Titanium Local Order and Photocatalytic Performance of TiO_2 Anatase. *J.Phys. Chem. C.* **2017**, *121*, 6770.

[15] Frenkel,A. I.; Yevick, A.; Cooper, C.; Vasic,R. Modeling the Structure and Composition of Nanoparticles by Extended X-Ray Absorption Fine-Structure Spectroscopy. *Annu. Rev. Anal. Chem.* **2011**, *4*, 23.

[16] Calvin, S.; Miller, M. M.; Goswami, R.; Cheng, S. F.; Mulvaney, S. P. ; Whitman, L. J.; Harris, V. G. Determination of crystallite size in a magnetic nanocomposite using extended X-ray absorption fine structure.*J. Appl. Phys.* **2003**, *94*, 778.

[17] Presti,L. L.; Ceotto,M.; Spadavecchia, F.;Cappelletti, G.; Meroni, D.; Acres, R. G.; Ardizzone,S. Role of the Nitrogen Source in Determining Structure and Morphology of N-Doped Nanocrystalline TiO_2. *J. Phys. Chem. C.***2014**, *118*, 4797.

[18] Bharti,B; Kumar, S;Lee , Heung-No; Kumar, R; Formation of oxygen vacancies and Ti3+ state in TiO2 thin film and enhanced optical properties by air plasma treatment.*Scientific Reports* **2016**, *6*, Article number: 32355.

[19] Grunes, L. A. Study of the K Edges of $3d$ Transition Metals in Pure and Oxide Form by X-ray-Absorption Spectroscopy. *Phys. Rev. B.* **1983**, *27*, 2111.

[20] Sandstrom, D. R.; Filby, R. H.; Lytle, F. W.; Greegor, R. B. Study of Ti in Solvent-Refined Coal by X-ray Absorption Spectroscopy. *Fuel* **1982**, *61*, 195.

[21] Landmann, M.; Rauls, E.; Schmidt,W. G. The electronic structure and optical response of rutile, anatase and brookite TiO_2 *J. Phys.: Condens. Matter.* **2012**, *24* 195503.

[22] Chen, L. X.; Rajh, T.; Wang, Z.; Thurnauer, M. C. XAFS Studies of Surface Structures of TiO_2 Nanoparticles and Photocatalytic Reduction of Metal Ions. *J. Phys. Chem. B.* **1997**, *101*, 10688.

[23] Rehr, J.J.; Kas,J.J.;Vila, F.D.; Prange, M.P.; Jorissen, K. Parameter-free calculations of X-ray spectra with FEFF9. *Phys. Chem. Chem. Phys.***2010**, *12*,5503.

[24] Jiang, N.; Su, D.; Spence, J. C. H. Determination of Ti coordination from pre-edge peaks in Ti K-edge XANES. *Physical Review B.* **2007**, *76*, 214117(1)-214117(9)

[25] Farges,F.; Brown,G. E.; Jr.; Rehr, J. J. TiK-edge XANES studies of Ti coordination and disorder in oxide compounds: Comparison between theory and experiment. *Phys. Rev. B.* **1997**, *56*, 1809.

[26] Demenchenko,I. N.; Denlinger, J. D.; Chernyshova, M.; Yu, K. M.; Speaks, D. T.; Olalde-Velasco, P.; Hemmers, O.; Walukiewicz, W.; Derkachova, A.; Lawniczak-Jablonska, K. Full multiple scattering analysis XANES at the Cd L_3 and O K edges in CdO films combined with a soft X-ray emission investigation. *Physical Review B*, **2010**, *82*, 075107.

[27] Fronzoni, G.; De Francesco, R.; Stener, M.; Causa, M. X-ray Absorption Spectroscopy of Titanium Oxide by Time Dependent Density Functional Calculations. *J. Phys. Chem. B*,**2006**, *110*,9899.

[28] Chaboy,J. ;Nakajima, N.; Tezuka,Y. Ab initio x-ray absorption near-edge structure study of Ti K-edge in rutile. *J. Phys.: Condens. Matter* ,**2007**,*19*, 266206.

[29] Waychunas, G. A. Synchrotron radiation XANES spectroscopy of Ti in minerals: Effects of Ti bonding distances, Ti valence, and site geometry on absorption edge structure. *American Mineralogist.***1987**, *72*,89.

[30] Greegor R. B.; Lytle. W. F.;Sandstrom, D. R.; Wong, J.; Schultz, P. Investigation of TiO_2-SiO_2 glasses by X-ray Absorption Spectroscopy. *Journal of Non-Crystalline Solids.* **1983**, *55*, 27.

[31] Yarker C. A.;Johnson P.A.V.;Wright A.C. Neutron diffraction and EXAFS evidence for TiO_5 units in Vitreous K_{20}-TiO_2-$2\,SiO_2$. *J. Non-Cryst. Solids.* **1986**, *79*, 117.

[32] Farges,F.; Brown,G. E.; Jr.; Rehr, J. J. Coordination chemistry of Ti (IV) in silicate glasses and melts: I. XAFS study of titanium coordination in oxide model compounds. *Geochim. Cosmochim. Acta* **1996**, *60*, 3023.

[33] Farges,F.; Brown, G. E. Jr.; Rehr, J. J. Ti K-edge XANES studies of Ti coordination and disorder in oxide compounds: Comparison between theory and experiment *J. Phys. Chem. C.* **1997**, *111*, 1809.

[34] Yamamoto, T. Assignment of pre-edge peaks in K-edge X-ray absorption spectra of 3d transition metal compounds: electric dipole or quadrupole? *X-Ray Spectrom.* **2008**, *37*, 572.

[35] Paula C. Angelome et al. Mesoporous Anatase TiO_2 Films: Use of Ti K XANES for the Quantification of the Nanocrystalline Character and Substrate Effects in the Photocatalysis Behavior, *Physical Review B* **2007**, *111*, 10886.

Chapter 5

Photo-induced Wetting Studies on N-doped TiO_2 Films

5.1 Introduction

In chapter 3, XPS and detailed EXAFS studies on N-doped TiO_2 confirms the doping of nitrogen in the interstitial position of TiO_2matrix. Optical absorption studies on these films signaled the formation of interband states viz. N 2p states lying above the valence band. These interband states are known to facilitate absorption in the visible region, by exciting electrons from N $2p$ states to conduction band and thereby increasing the number of electrons and holes[1–4] as compared to pristine TiO_2. These photo-generated charge carriers can then be utilized in various surface redox reactions, which in turn make the material self cleaning and anti-fogging. Anti-fogging property of a material is studied from its wetting-dewetting behaviour. Wetting behaviour of TiO_2 surfaces is explained on the basis of two mechanisms, which are briefly discussed here. The first mechanism (shown in Scheme 5.1) is redox reactions at surfaces, wherein electrons reduce Ti^{4+} is to Ti^{3+} and holes oxidize the O^{2-} anions. This results in ejection of oxygen atoms thereby creating oxygen vacancies. The water molecules occupy the oxygen vacancies, producing adsorbed OH groups, which tend to make the surface hydrophilic.[5] The second mechanism is destruction of surface adsorbed organics via photocatalytic process, wherein, the photo generated electrons and holes dissociate the organic molecules.[6]

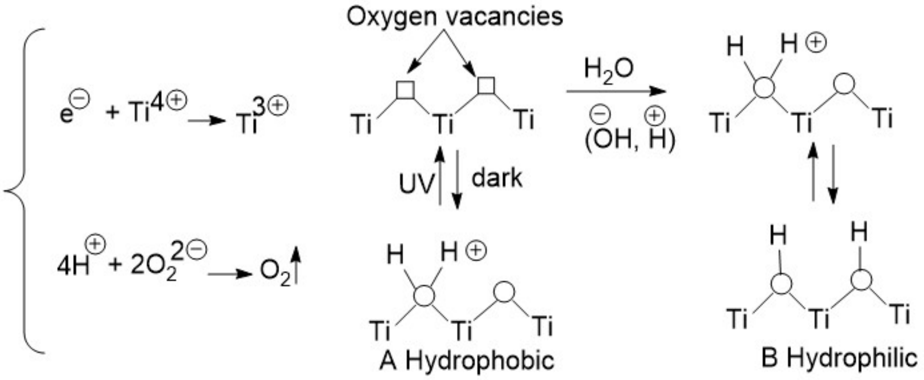

Scheme 5.1: Surface reconstruction via redox reactions.[22]

Apart from being known for the conversion of hydrophobic to hydrophilic surface, TiO_2 is also known for the its photo induced hydrophobic – hydrophilic reversibility.[6] Reversibility of wetting is of technological importance and therefore, it is prudent to examine the wetting - dewetting behavior in detail.

The wetting - dewetting properties of TiO_2 thin films were first reported by Wang and co-workers, who showed that under UV light irradiation, the wetting contact angle of a polycrystalline TiO_2 thin film changes from partially hydrophobic to super-hydrophilic and reverts to its initial hydrophobic state upon keeping under visible light or under dark.[7] The commonly accepted physico-chemical processes, responsible for this switching behaviour, though is in debate ever since Wang's report, are photo-induced reconstruction of TiO_2 surfaces due to hydroxylation[7] and removal of surface adsorbed organic species responsible for hydrophobicity.[8] However, since TiO_2 is only active to UV radiation, subsequently N-doped TiO_2 samples, which are visible light active, were also examined for its wetting dewetting behaviour. The wetting - dewetting properties of N-doped TiO_2 surfaces have been studied by few groups in the recent past.[9–12] All the studies report reduction in contact angles in the hydrophilic regime ($\theta \sim$ 15-25°) to ($\theta \sim 3-9°$)[9–11] and ($\theta \sim 80°$) to ($\theta \sim$ 55 and 30°).[12] A recent study by Wang et al.[7] on visible-light-driven reversible hydrophobic to hydrophilic transition of N-doped TiO_2 powders dispersed on a wafer surface reports water contact angle reduction from 135±5° to 0° in 6 hours of visible light irradiation. However, the authors did not report the results with respect to nature of N-doping. The reports regarding the reversibility were also scant. In addition, although the mechanism of sunlight or visible light induced hydrophobic to hydrophilic conversion of N-doped TiO_2 surfaces were proposed (hydroxylation and removal of surface adsorbed organic species), experimental evidences for the same are lacking. In addition, the kinetics which is an important aspect of investigation for technological application of reversible hydrophobic ↔ superhydrophilic conversion has not received enough attention.

The focus of this chapter is on reporting the photo-induced superhydrophilicity in case of N-doped TiO_2 and delineating the mechanism behind superhydrophilicity. In addition, the reversibility in wetting behaviour and the kinetics of reversibility of these films are also discussed.

5.2 Roughness and microstructure

Roughness plays a major role in determining the wetting behaviour of the material. Hence, roughness of the samples were measured using a surface profilometer (Dektak, USA) and are listed in Table 5.1.

Table 5.1 – Thickness and Roughness of N-TiO_2 thin films

Sample id	Film roughness(nm)
$TiO_2$400 °C	3.6
$TiO_2$450 °C	3.1
$TiO_2$500 °C	3.0
$TiO_2$550 °C	1.7
N:$TiO_2$400 °C	3.1
N:$TiO_2$450 °C	3.0
N:$TiO_2$500 °C	2.9
N:$TiO_2$550 °C	1.2

5.3 Wetting Studies

The wetting characteristics of the N-doped samples were evaluated by water contact angle (CA) measurements. Figure 5.1 and 5.2 shows the time evolution of the water contact angle of pristine TiO_2 and N-doped TiO_2 synthesized at different substrate temperatures (T_s = 400, 450,500, 550 °C) after sunlight irradiation of $\sim$10 mW cm^{-2} intensity for a duration of 40 minutes. The intensity of sunlight was measured throughout the course of the experiment to ascertain constant irradiation intensity. As seen from the figures (5.1 and 5.2), all the samples showed CA in the range of 88 to 105 ° prior to irradiation (at t=0) and therefore exhibit hydrophobicity. The difference in the initial wetting contact angle (WCA) is attributed to the difference in surface roughness (as shown in Table 5.1). According to Cassie and Baxter[32,35] the WCA increases with roughness due to the cushioning effect from trapped air. In particular, the samples synthesized at T_s , 400, 450 and 500 °C have roughness around 3 nm and have wetting contact angle around 105 °. The sample synthesized at 550°C has the least surface roughness (1.2 nm) and therefore has the lowest WCA (88°). The observation in the present experiment is in agreement with the WCA of a smooth polycrystalline anatase TiO_2 surface (free of OH-Ti) of WCA 82 as estimated by Borras and Gonzalez-Elipe.[36,37] A comparative look at fig 5.1 and 5.2 reveals that although the pristine films synthesized at 500 and 550 °C attained hydrophilicity with contact angle value $\sim$ 17° at t= 40mins, it did not attain superhydrophilicity. Whereas N-doped TiO_2 samples showed superhydrophilicity with a contact angle value of $\sim$ 7°. This decresse in WCA between doped and unoped TiO_2 for identical conditions of exposure to sunlight indicates the visible light induced hydrophobic → super-hydrophilic conversion in N-doped TiO_2 samples. In order to examine the reversibility in wetting behavior, the most super-hydrophilic N-doped sample (T_s=550 °C) with the lowest WCA (7 °)was selected and was subjected to alternate exposure to sunlight and dark. The reversibility was tested for several such dark-sunlight illuminated cycles and reversibility for typical 4 cycles is shown in fig 5.3. The results of this experiment show that the N-TiO_2 sample reverted to the initial hydrophobic state when kept in dark for ∼5 days and attained super-hydrophilicity in 30-40 minutes upon sunlight irradiation, which confirmed the switching behavior.

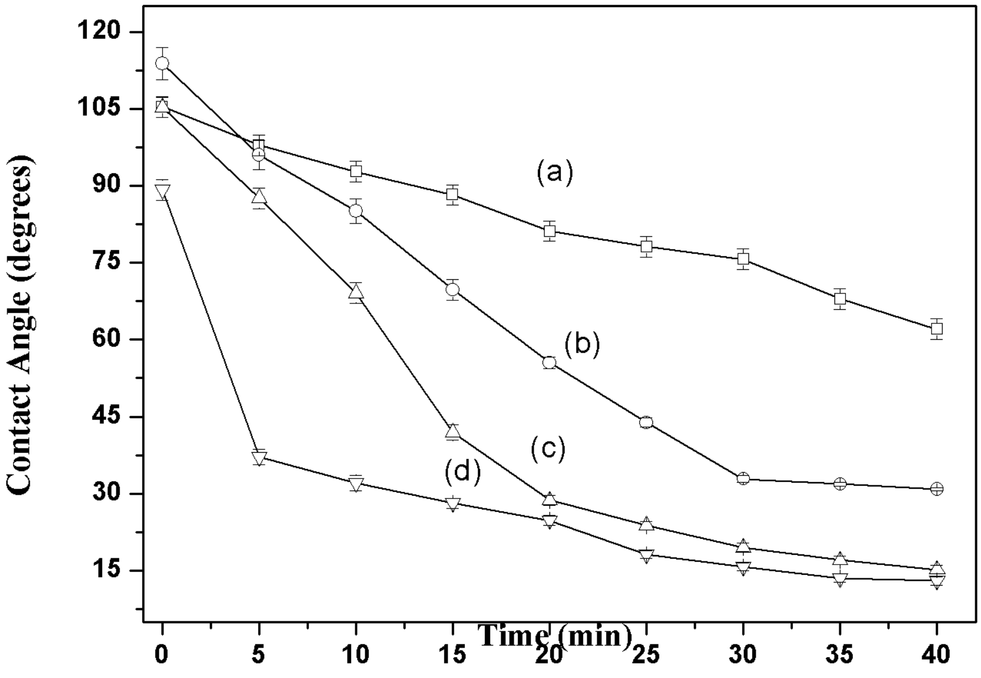

Figure 5.1 – Variation in contact angle with irradiation time for TiO_2 films synthesized at (a) 400, (b) 450, (c) 500, and (d) 550 °C

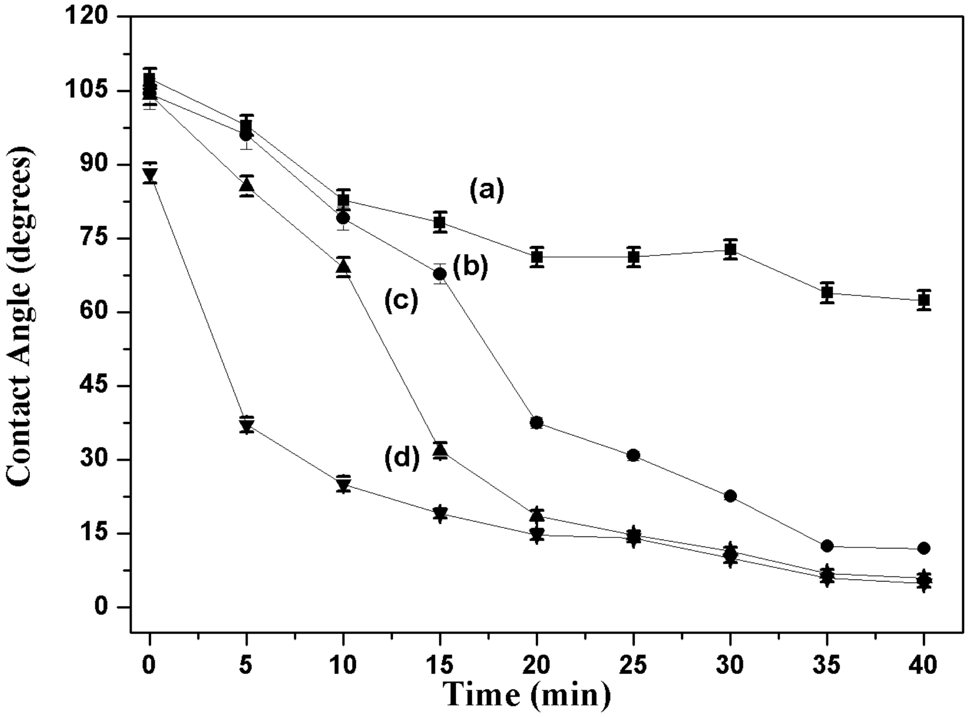

Figure 5.2 – Variation in contact angle with irradiation time for N-doped TiO_2 films synthesized at (a) 400, (b) 450, (c) 500, and (d) 550 °C

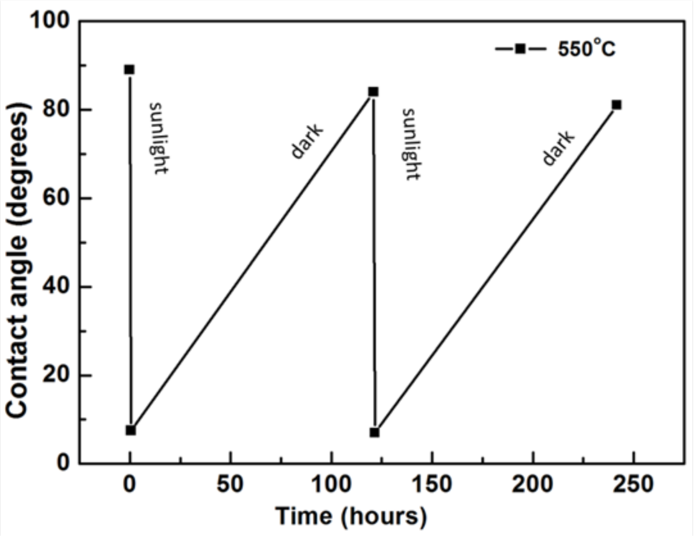

Figure 5.3 – Switching pattern of N-doped samples synthesized at 550°C

In order to understand the reason behind sunlight driven hydrophobic - super hydrophilic transitions of N-doped TiO_2 samples, it was important to investigate the chemical nature of the surfaces before and after sunlight irradiation. Therefore, XPS spectra of N-doped TiO_2 samples before and after sun light irradiation were acquired. Adequate precautions such as covering view ports of XPS chamber with aluminum foils were undertaken to avoid exposure of samples to ambient light. The O1s spectra before and after irradiation is given in Fig 5.4 to Fig 5.7. The deconvolution of the high resolution O-1s spectra(Figure 5.4-5.7) shows five peaks. The peaks corresponding to BE values 530.6 and 531.3 eV can be attributed to the O-Ti bonds.[38,39] The peaks at 532.4, 533.2 eV, 534.2 eV correspond to HO-Ti, adsorbed H_2O and O-C bonds respectively.[40–42]

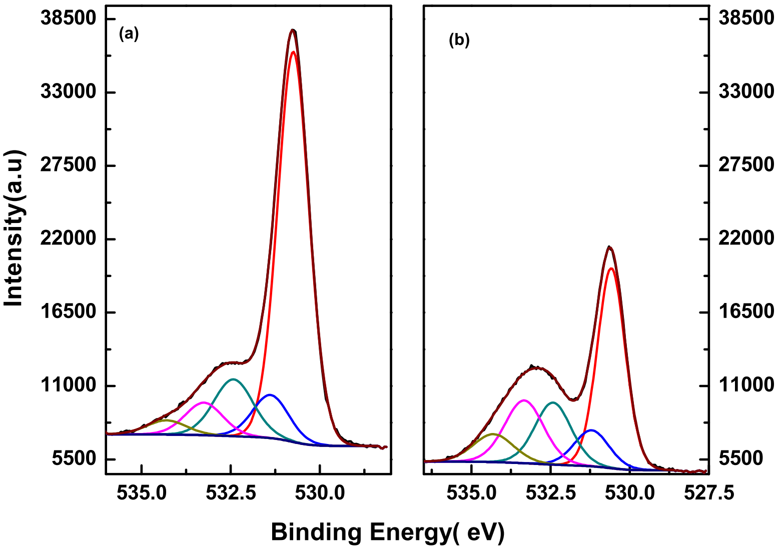

Figure 5.4 – Deconvoluted O1s spectra of N-doped TiO_2 synthesized at 400°C, before and after sunlight irradiation.

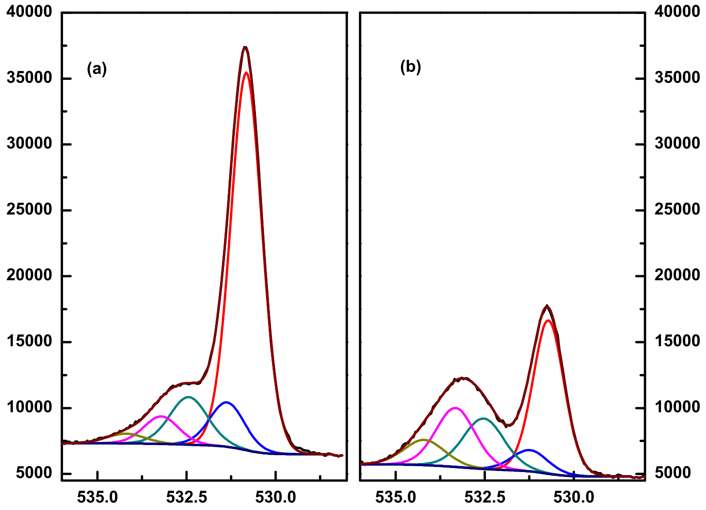

Figure 5.5 – Deconvoluted O1s spectra of N-doped TiO_2 synthesized at 450°C, before and after sunlight irradiation.

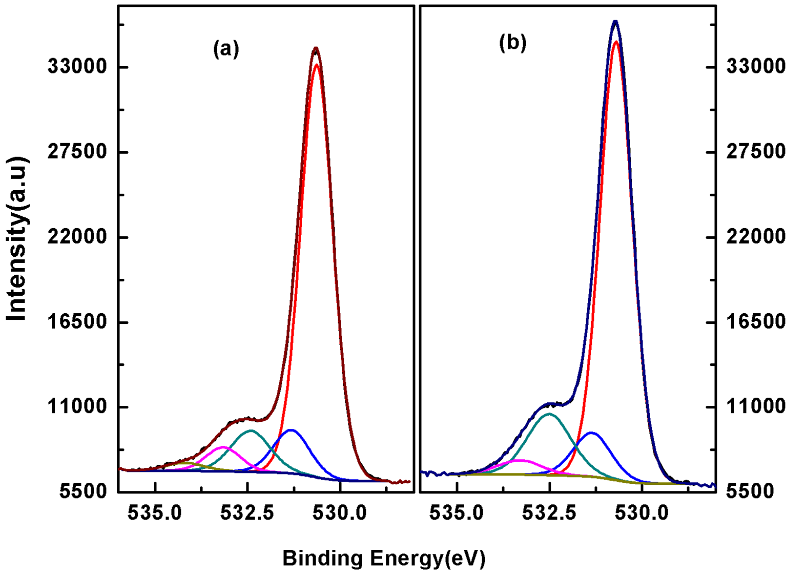

Figure 5.6 – Deconvoluted O1s spectra of N-doped TiO_2 synthesized at 500°C, before and after sunlight irradiation.

Table 5.2 – Fraction of HO-Ti and CO surface species with respect to total surface O-Ti species

Sample id	f_{OH} = OH/(Ti-O+OH)		f_{CO} = CO/(TiO+OH+CO)	
	Before irradiation	After irradiation	Before irradiation	After irradiation
N:$TiO_2$400 °C	0.139	0.247	0.0336	0.011
N:$TiO_2$450 °C	0.125	0.231	0.025	0.006
N:$TiO_2$500 °C	0.09	0.114	0.0186	0.0
N:$TiO_2$500 °C	0.113	0.447	0.0202	0.0

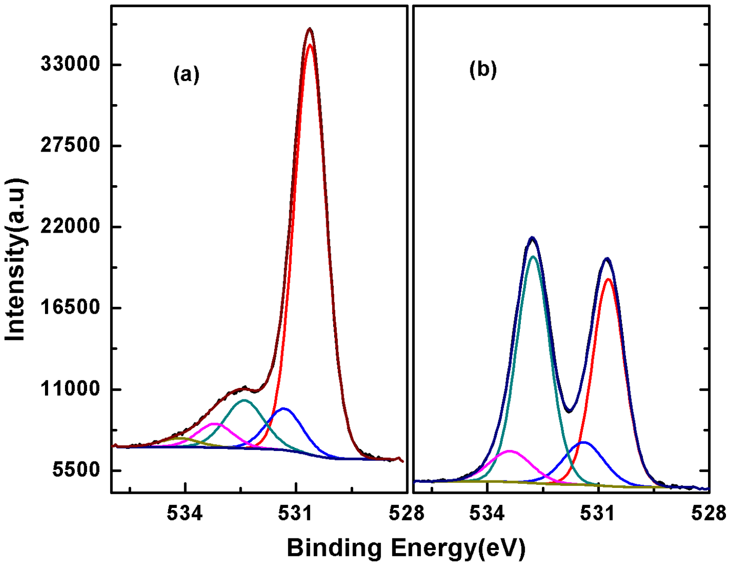

Figure 5.7 – Deconvoluted O1s spectra of N-doped TiO_2 synthesized at 550°C, before and after sunlight irradiation.

It is important to point out that the hydrophilicity in TiO_2 surfaces is attributed to the formation of Ti-OH species and destruction of surface adsorbed organic species. Therefore, the fraction of HO-Ti species and CO surface species before and after irradiation is expected to throw some insights into the mechanism of hydrophobic to hydrophilic conversion. Table-5.2 shows the fraction of Ti-OH species calculated from the area under the deconvoluted peaks corresponding to 532.4 and 534.2 eV and relative sensitivity factor of oxygen.

From table 5.2 it is clear that f_{OH} increases with sunlight irradiation confirming surface hydroxylation as one of the physico-chemical process responsible for photo-induced hydrophilicity. Though there is an increase in f_{OH} for films synthesized at

400°C, it did not show super-hydrophilicity ($\theta \leq 10°$). The lack of such superhydrophilicity is explained on the basis of the presence of carbonaceous species on the samples. The origin of carbonaceous species in the samples is attributed to the incomplete surface reaction of the precursor (carbon bearing metalo-organic precursors ($Ti(OAcAc)_2$)) used in the synthesis of N-doped TiO_2 films. It is known that as the synthesis temperature increases, it leads to complete oxidation of the precursor to CO_2 and other gaseous products, thus leaving behind a surface with less remnant carbonaceous species. This is evident from the fraction of CO species as obtained from the analysis of O 1s spectra, which is given as f_{CO} in Table 5.2. It is observed from table 5.2 that f_{CO} decreases as the synthesis temperature increases, which indicates presence of highest amount of carbonaceous species for the sample synthesized at $T_s = 400\ ^\circ$ C as compared to the samples synthesized at higher temperatures. Sunlight irradiation on these samples leads to destruction of carbonaceous species, which is quantified by calculating f_{CO} before and after sunlight irradiation (refer last two columns of Table 5.2).

It is observed that the decrease in f_{CO} for the samples synthesized at 400 and 450 °C is marginal after sunlight irradiation, whereas f_{CO} decreases to zero for the samples synthesized at 500 and 550°C. This indicates complete destruction of carbonaceous species .in case of samples synthesized at T_s= 500 and 550°C. Thus, the increase in f_{OH} explains the hydrophobic to hydrophilicity in all the samples. However, superhydrophilicity as observed for the samples synthesized at 500 and 550°C is attributed to the decrease in f_{CO}. This confirms the role of adsorbed carbonaceous species in the super-hydrophilic behavior of N-doped TiO_2 surfaces. Since, destruction of carbonaceous species is the key to attain superhydrophilicty, C 1s spectra of the N-doped TiO_2 samples were analysed before and after sunlight irradiation which are shown from fig 5.8 to 5.11. The deconvoluted C1s spectra shows four peaks. Among the four peaks, two peaks are centered around 285 eV, the other two are centered around

287.4 eV and 289.75 eV. The C-1s peaks around 285 eV corresponds to adventitious carbon (contaminated amorphous C) present in the film surface. The peaks with BE values ∼287.4 and ∼289.75 eV corresponds to oxygen bearing carbonaceous species. It is observed that there is a clear reduction in the intensity of peaks corresponding to BE values ∼287.4 and ∼289.75 eV for the samples synthesized at 500 and 550°C, after sunlight irradiation, indicating the role of carbonaceous species in the super-hydrophilic character of these surfaces. No such reduction was observed in the case of films synthesized at 400 and 450 °C. The C-1s peaks around 285 eV is not considered as adventitious carbon is found on the surface of all films as a result of contamination from the atmosphere. This corroborates that the major factor behind the hydrophobic → hydrophilic transition is surface hydroxylation whereas the process responsible for the hydrophilic → super-hydrophilic transition is destruction of hydrocarbons present on the surface.

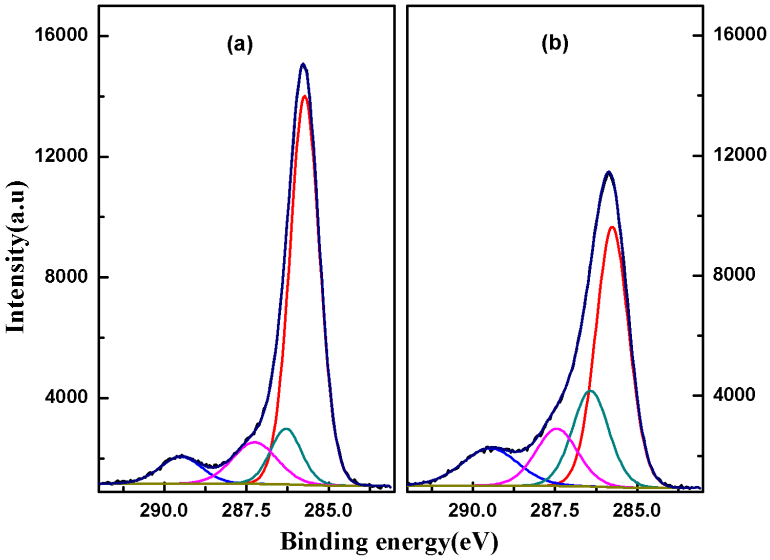

Figure 5.8 – Deconvoluted C1s spectra of N-doped TiO_2 synthesized at 400°C, before and after sunlight irradiation.

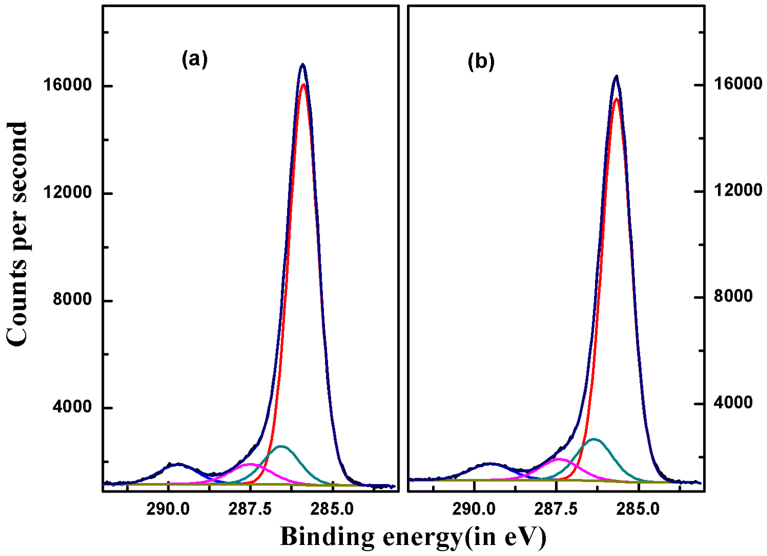

Figure 5.9 – Deconvoluted C1s spectra of N-doped TiO_2 synthesized at 500°C, before and after sunlight irradiation.

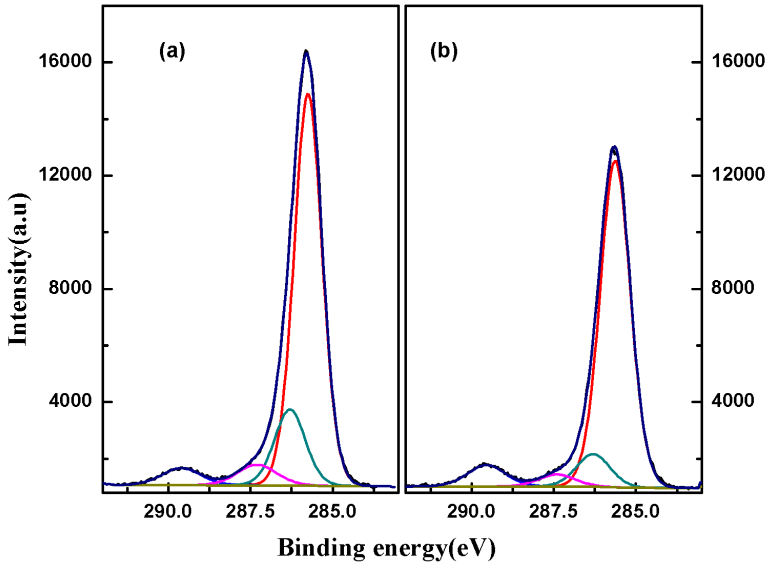

Figure 5.10 – Deconvoluted C1s spectra of N-doped TiO_2 synthesized at 500°C, before and after sunlight irradiation.

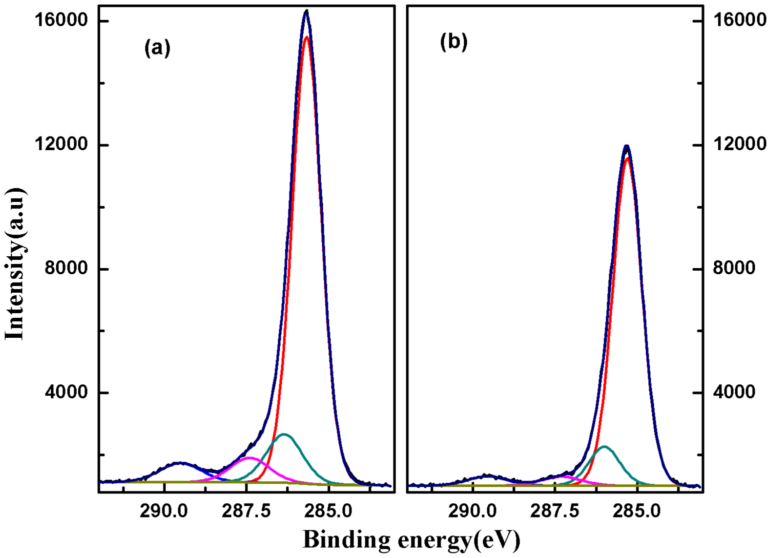

Figure 5.11 – Deconvoluted C1s spectra of N-doped TiO_2 synthesized at 550°C, before and after sunlight irradiation.

In view of the above analysis, the mechanism behind the hydrophobic ↔ superhydrophilic conversion is described as follows. The hydrophobic nature of the films indicates that its surface energy is not adequate to overcome the surface tension of water, when the water droplets come in contact with it. The low surface energy of the films can be attributed to the presence of adsorbed hydrocarbons. Because the molecular forces that hold the hydrocarbons together are much weaker than the forces that act between water molecules, the film surface do not possess adequate energy to overcome the water surface tension and consequently the surface remains hydrophobic. The photo-generated free electrons and holes diffuse to the surface and destroy the adsorbed hydrocarbon species generating high energy fresh surfaces. In addition, the holes attack and cleave the surface Ti-O bonds leading to the formation of surface hydroxyl groups and consequent surface restructuring enhancing the surface energy. The resultant high-energy surface decreases its energy by surface wetting. Thus the intrinsically hydrophobic surface is transformed to superhydrophilic.

5.4 Kinetics of the hydrophobic to superhydrophilic transition

The kinetics of hydrophobic ↔ superhydrophilic transition can be studied from the variation of cosine of contact angle ($cos\theta$) with time. According to Young's theory the $cos\theta$ of a liquid droplet on a solid surface is a function of the interfacial energy between the solid and liquid[25] that in turn changes with the surface fraction of hydrophilic region. The three interfacial energies are related to the $cos\theta$ by the Young's equation as given in equation 5.1 :

$$\gamma cos\theta = \gamma_{SG} - \gamma_{SL} \tag{5.1}$$

where γ is the surface tension of liquid, γ_{SG} is the interfacial energy between the solid and the gas, and γ_{SL} is the interfacial energy between the solid and the liquid. Upon photo-irradiation the hydrophobic regions are converted to hydrophilic regions reducing the interfacial energy between the solid surface and liquid.

The simplest possible relation between the interfacial energy, γ_{SG} - γ_{SL}, and the surface fraction of hydrophilic regions, c, is a linear relation,

$$\gamma_{SG} - \gamma_{SL} = \gamma_1 c + \gamma_2 \tag{5.2}$$

Now, Young's equation(equation 5.1)can be rewritten as

$$f \equiv cos\theta = \frac{\gamma_{SG} - \gamma_{SL}}{\gamma} = f_1 c + f_2 \tag{5.3}$$

where $f_1 = \gamma_1 / \gamma$,$f_2 = \gamma_2 / \gamma$.When c = 0, $cos\theta$ has the value of f_2, whereas at c = 1 it has a value of $f_1 + f_2$. The hydrophilic regions turn back to hydrophobic in the dark. When both the hydrophilic conversion and its back-reaction are characterized by single rate constants, the kinetics of the change of the surface fraction of hydrophilic regions is given by

$$\frac{d}{dt}c(t) = k_f(1-c) - k_b c \tag{5.4}$$

where k_f is the forward reaction rate constant and k_b denotes the backward reaction rate constant. By substituting the solution of eq 5.4 into eq 5.3 the time evolution of $cos\theta$ after photo-irradiation is obtained as

$$f(t) = f_1[\frac{k_f}{k_f+k_b} - (\frac{k_f}{k_f+k_b} - c(0))exp{-}(k_f+k_b)t] + f_2 \tag{5.5}$$

Hence, the value of of $cos\theta$ increases from the initial value of

$$f(t=0) = f_1 c(0) + f_2 \tag{5.6}$$

to the final value corresponding to saturated hydrophilicity,

$$f(t\to\infty) = \frac{f_1}{k_f+k_b} + f_2 \tag{5.7}$$

The rate constant for the hydrophillic to the hydrophobic conversion in the dark is given by,

$$f_b(t) = f_1 c_b(0) exp(-k_b)t + f_2 \tag{5.8}$$

Where, $f_b(t)$ is the decay function in the dark and $c_b(0)$ is the initial surface fraction of hydrophilic regions.

5.4.1 Calculation of rate constants

Exponential equation represented in equation 5.8 was used for fitting the decay in $cos\theta$ values with respect to time which was obtained for the hydrophilic to hydrophobic conversion (Fig 5.12 (a)). The fitted parameters yielded f_2 as 0.1918 and k_b (the rate of super-hydrophilic → hydrophobic conversion) as 1.97 x 10^{-4} min^{-1}. At t= 0,c=0 equation 5.6 gives us $cos\theta = f_2$. Hence,the contact angle at t=0 (taking f_2 =0.1918) was calculated to be 79°. Similarly, the hydrophobic to super-hydrophilic conversion rate, k_f, under sunlight can be obtained from the plot of cosθ against irradiation time(Fig 5.12(b)), using the value of k_b. The calculated rate, k_f, is 0.216 min^{-1}. Since $k_f >> k_b$ the largest value of cosθ obtained at $t = \infty$ (see equation 5.7) can be described by

$$cos\theta = f_1 + f_2 \tag{5.9}$$

Using the highest value of cosθ in this experiment which corresponds to 0.99 in equation 5.9, value of f_1 (γ_1/γ) was found out to be 0.798. When f_1 and f_2 is substituted in the equation 5.9, which also represents the state of superhydrophilicty, the contact angle was found out to be 8.1°. The smallest and largest contact angle (8.1° and 79°) calculated from the analysis of cosθ versus time curves given in figure 5.12(a) and 5.12(b) matches with the corresponding experimentally observed values of 5° and 88° (Fig 5.2 (d)).

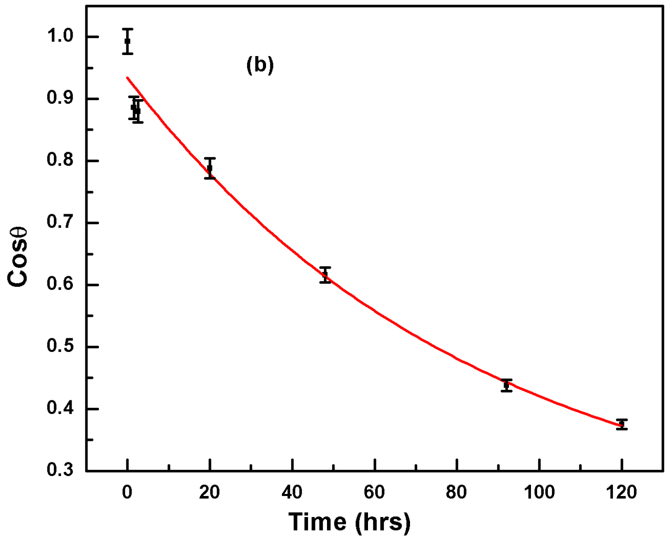

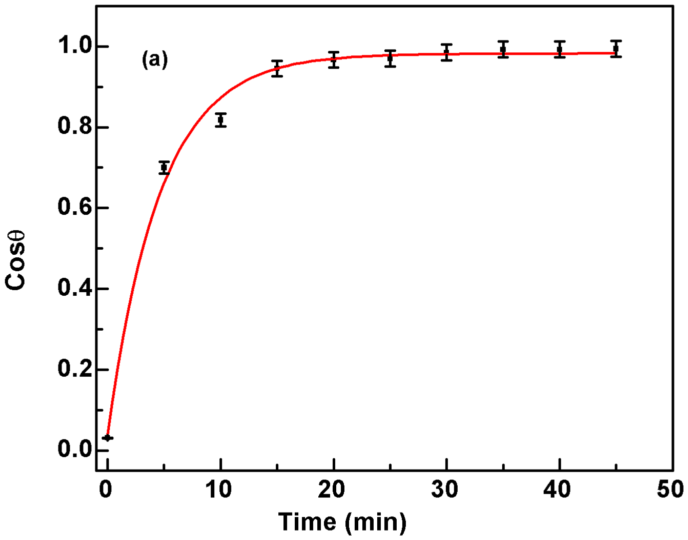

Figure 5.12 – Variation in $cos\theta$ with time (b) while kept in dark super-hydrophilic → hydrophobic conversion (a) hydrophobic → super-hydrophillic conversion

5.5 Wetting study of an oxygen deficient TiO_2 thin film.

Among the oxygen deficient films,the film with highest concentration of oxygen vacancies (TiO_2 450 °C-8h) was chosen and its wetting characteristics was evaluated by water contact angle (CA) measurements. The time evolution of contact angle of TiO_2

450 °C-8h is given figure 5.13. Time evolution of CA of N-doped films synthesized at T_s= 500, 550 °C are also shown in the figure for comparative purpose. It is observed from the figure that, TiO_2 450 °C-8h film attained hydrophilicity in 40 mins and superhydrophilicity in about 65 mins as compared to the N-doped films, which attained superhydrophilicity in 40 mins. TiO_2 450 °C-8h film reverted back to its original hydrophobic state in 5-6 days.

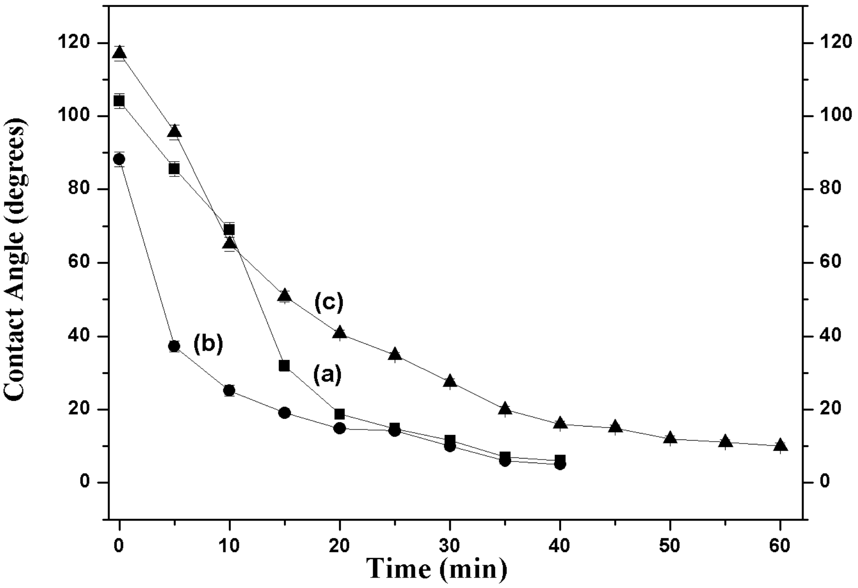

Figure 5.13 – Variation in contact angle with irradiation time for (a) N-doped TiO_2,T_s= 500 °C (b) N-doped TiO_2,T_s= 550 °C (c) TiO_2 450 °C - vacuum annealed for 8hours.

5.6 Conclusion

Wetting studies of TiO_2 and N-doped TiO_2 films revealed that Nitrogen doping in TiO_2 transforms hydrophobic surfaces to super-hydrophilic surfaces upon sunlight irradiation. The hydrophilic surfaces reverted to the initial hydrophobic state in 5 days when kept in dark and became hydrophilic again on sunlight irradiation confirming the switching behavior. Analysis of the surface before and after irradiation, by XPS, revealed generation of HO-Ti species and destruction of organic species upon sunlight irradiation, confirming the role of surface hydroxylation and organic species removal in the wetting behaviour. The rate of hydrophobic → superhydrophilic conversion when irradiated with sunlight and the rate of superhydrophilic → hydrophobic conversion when the irradiated film is kept under dark calculated following the theoretical analysis of Seki and Tachiya is 0.224 min^{-1} and 2.03x10 $^{-4}$ min^{-1} respectively. The oxygen deficient film also showed superhydrophilicity upon exposure to sunlight for 65 mins as compared to N-doped films, which attained superhydrophilicity in 40 mins.

Bibliography

[1] Lee, J. Y.; Park, J.; Cho, J. H. Electronic Properties of N-and C-doped TiO_2 *Appl. Phys. Lett.* **2005**, *87*, 11904.

[2] Xiaobo, C.; Burda, C. The Electronic Origin of the Visible-Light Absorption Properties of C-, N- and S-Doped TiO_2 Nanomaterials. *J. Am. Chem. Soc.* **2008**, *130*, 5018.

[3] Nakamura, R.; Tanaka, T.; Nakato, Y. Mechanism for Visible Light Responses in Anodic Photocurrents at N-Doped TiO_2 Film Electrodes *J. Phys. Chem. B.* **2004**, *108*, 10617.

[4] Asahi, R.; Morikawa, T.; Ohwaki, T.; Aoki, K.; Taga, Y. Visible-Light Photocatalysis in Nitrogen-Doped Titanium Oxides. *Science.* **2001**, *293*, 269.

[5] Fujishima, A.; Rao,T. N.; Tryk, D. A. Titanium Dioxide Photocatalysis: Photochemistry Reviews. *J. of Photochemistry and Photobiology C.* **2000**, *1*, 1.

[6] Carp, O.; Huisman, C.L.; Reller, A. Photoinduced Reactivity of Titanium Dioxide. *Progress in Solid State Chemistry.* **2004**, *32*, 33.

[7] Wang, R.; Hashimoto, K.; Fujishima, A. Light-induced Amphiphilic Surfaces. *Nature.* **1997**, *388*, 431.

[8] Zubkov, T.; Stahl, D.; Thompson, T. L.; Panayotov, D.; Diwald, O.; Yates, J. Ultraviolet Light-Induced Hydrophilicity Effect on $TiO_2(110)(1\times1)$. Dominant

Role of the Photooxidation of Adsorbed Hydrocarbons Causing Wetting by Water Droplets. *J. Phys. Chem. B.* **2005**, *109*, 15454.

[9] Yang, M. C.; Yang, T. S.; Wong, M. S. Nitrogen-Doped Titanium Oxide Films as Visible Light Photocatalyst by Vapor Deposition, *Thin Solid Films.* **2004**, *1-5*, 469.

[10] Yang, T. S.; Yang, M. C.; Shiu, C. B.; Chang, W. K.; Wong, M. S. Effect of N_2 Ion Flux on the Photocatalysis of Nitrogen-Doped Titanium Oxide films by Electron-Beam Evaporation. *Appl. Surf. Sci.* **2006**, *252*, 3729.

[11] Irie, H.; Washizuka, S.; Yoshino, N.; Hashimoto, K. Visible-Light Induced Hydrophilicity on Nitrogen-Substituted Titanium Dioxide Films. *Chem. Commun.* **2003**, *11*, 1298-1299.

[12] Borras, A.; Lopez, C.; Rico, V.; Gracia, F.; Gonzalez-Elipe, A. R.; Richter, E.; Battiston, G.; Gerbasi, R.; McSporran, N.; Sauthier, G.; Gyorgy, E.; Figueras, A. Effect of Visible and UV Illumination on the Water Contact Angle of TiO_2 Thin Films with Incorporated Nitrogen. *J. Phys. Chem. C.* **2007**, *111*, 1801.

[13] Yu, J.C.; Ho, W.; Lin, J.; Yip, H.; Wong, P. K. Photocatalytic Activity, Antibacterial Effect, and Photoinduced Hydrophilicity of TiO_2 Films Coated on a Stainless Steel Substrate. *Environ. Sci. Technol.* **2003**, *37*, 2296.

[14] Allain, E.; Besson, S.; Durand, C.; Moreau, M.; Gacoin, T.; Boilot, J.P. Transparent Mesoporous Nanocomposite Films for Self-Cleaning Applications. *Adv. Funct. Mater.* **2007**, *17*, 549.

[15] Antony, R.P.; Mathews, T.; Ramesh, C.; Murugesan, N.; Dasgupta, A.; Dhara, S.; Dash, S.; Tyagi, A. K. Efficient Photocatalytic Hydrogen Generation by Pt Modified TiO_2 Nanotubes Fabricated by Rapid Breakdown Anodization. *Int. J. Hydrogen Energy.* **2012**, *37*, 8268.

[16] Oregan, B.; Gratzel, M. A Low-Cost, High-Efficiency Solar Cell Based on Dye-Sensitized Colloidal TiO_2 Films. *Nature.* **1991**, *353*, 737.

[17] Nazeeruddin, M. K.; Kay, A.; Rodicio, I.; Humphry-Baker, R.; Mueller, E.; Liska, P.; Vlachopoulos, N.; Graetzel, M. Conversion of Light to Electricity by Cis-X_2Bis (2, 2'-bipyridyl-4, 4'-dicarboxylate) Ruthenium (II) Charge-Transfer Sensitizers (X= Cl^-, Br^-, I^-, CN^-, and SCN^-) on Nanocrystalline Titanium Dioxide Electrodes. *J.Am.Chem.Soc.* **1993**, *115*, 6382.

[18] Iftimie, N.; Crisan, M.; Braileanu, A.; Crisan, D. C.; Nastuta, A.; Rusu, G. B.; Popa, P. D.; Mardare, D. On the Sensing Gas Properties of Titanium Dioxide Films. *J. Optoelectron. Adv. Mater.* **2008**, *10*, 2363.

[19] Martinez-Ferrero, E.; Sakatani, Y.; Boissiere, C.; Grosso, D.; Fuertes, A.; Fraxedas, J.; Sanchez, C. Nanostructured Titanium Oxynitride Porous Thin Films as Efficient Visible-Active Photocatalysts. *Adv. Funct. Mater.* **2007**, *17*, 3348.

[20] Bozzi, A.; Yuranova, T.; Guasaquillo, I.; Laubb, D.; Kiwi, J. *J. Photochem. Photobiol. A.* **2005**, *174*, 156.

[21] Nakajima, A.; Hashimoto, K.; Watanabe, T.; Takai, K.; Yamauchi, G.; Fujishima, A. Transparent Superhydrophobic Thin Films with Self-Cleaning Properties. *Langmuir.* **2000**, *16*, 7044.

[22] Fujishima, A.; Zhang, X. T.; Tryk, D. A. TiO_2 Photocatalysis and Related Surface Phenomena. *Surf. Sci. Rep.* **2008**, *63*, 515.

[23] Parkin, I.P.; Palgrave, R. G. Self-Cleaning Coatings. *J. Mater. Chem.* **2005**, *15*, 1689.

[24] Seki, K.; Tachiya, M. Kinetics of Photoinduced Hydrophilic Conversion Processes of TiO_2 Surfaces *J. Phys. Chem. B.* **2004**, *108 (15)*, 4806.

[25] Young, T. An Essay on the Cohesion of Fluids. *Philos. Trans. R. Soc. London .* **1805**, *95*, 65.

[26] Adamson,A. W. ; Ling, I. The Status of Contact Angle as a Thermodynamic Property, Contact Angle, Wettability, and Adhesion, *Chapter 3*, 57.

[27] Johnson Jr.R. E. Conflicts between Gibbsian Thermodynamics and Recent Treatments of Interfacial Energies in Solid-Liquid-Vapor, J. Phys. Chem. 1959, 63 (10),1655–1658.

[28] Seo, K.; Kim, M.; Kim,D. H. Re-derivation of Young's Equation, Wenzel Equation, and Cassie-Baxter Equation Based on Energy Minimization, *doi:10.5772/61066.*

[29] Whyman,G.; Bormashenko, E.; Stein, T. The rigorous derivation of Young, Cassie–Baxter and Wenzel equations and the analysis of the contact angle hysteresis phenomenon, *Chemical Physics Letters.* **2008**, *450*, 355.

[30] Wenzel, R.N. Resistance of Solid Surfaces to Wetting by Water, *Industrial and Engineering Chemistry.* **1936**, *28*, 987.

[31] de Gennes, P. G. Wetting: Statics and Dynamics. *Rev. Mod. Phys.* **1985**, *57*, 827.

[32] Cassie, A. B. D.; Baxter, S. Wettability of Porous Surfaces. *Trans. Faraday Soc.* **1944**, *40*, 546.

[33] Rosario, R.; Gust, D.; Garcia, A. A.; Hayes, M.; Taraci, J. L.; Clement, T.; Dailey, J. W.; Picraux, S. T. Lotus Effect Amplifies Light-Induced Contact Angle Switching. *J. Phys. Chem. B.* **2004**, *108*, 12640.

[34] Marmur, A. The Lotus Effect: Superhydrophobicity and Metastability. *Langmuir.* **2004**, *20*, 3517.

[35] Feng, X.; Zhai, J.; Jiang, L. The Fabrication and Wwitchable Superhydrophobicity of TiO_2 Nanorod Films. *Angew. Chem. Int. Ed.* **2005**, *44 (32)*, 5115.

[36] Borras, A.; Gonzalez-Elipe, A. R. Wetting Properties of Polycrystalline TiO_2 Surfaces: A Scaling Approach to the Roughness Factors, *Langmuir.* **2010**, *26 (20)*,15875.

[37] Miwa, M.; Nakajima, A.; Fujishima, A.; Hashimoto, K.; Watanabe, T. Effects of the Surface Roughness on Sliding Angles of Water Droplets on Superhydrophobic Surfaces, *Langmuir.* **2000**, *16*, 5754.

[38] Ingo, G. M.; Dire, S.; Babonneau, F. XPS Studies of SiO_2-TiO_2 Powders Prepared By Sol-Gel Process. *Appl. Surf. Sci.* **1993**, *70 - 71*, 230.

[39] Kuznetsov, M. V.; Zhuravlev, J. F.; Gubanov, V. A. XPS Analysis of Adsorption of Oxygen Molecules on the Surface of Ti and TiN_x Films in Vacuum. *J. Electron Spectrosc. Relat. Phenom.* **1992**, *58*, 169.

[40] Pouilleau, J.; Devilliers, D.; Groult, H.; Marcus, P. Surface Study of a Titanium-Based Ceramic Electrode Material by X-Ray Photoelectron Spectroscopy. *J. Mater. Sci.* **1998**, *32*, 5645.

[41] Nefedov, V. I.; Gati, D.; Dzhurinskii, B. F.; Sergushin, N. P.; Salyn, Y. V. *Journal of Inorganic Chemistry.(Zhurnal Neorganicheskoi Khimii).* **1975**, *20*, 2307.

[42] Glenis, S.; Benz, M.; LeGoff, E.; Schindler, J. L.; Kannewur, C. R.; Kanatzidis, M. G. Polyfuran: A New Synthetic Approach and Electronic Properties. *J. Am. Chem. Soc.* **1993**, *115*, 12519.

[43] Raut, N. C; Mathews, T.; Ajikumar, P. K.; George, R. P.; Dash, S.; Tyagi, A. K. Sunlight Active Antibacterial Nanostructured N-Doped TiO_2 Thin Films Synthesized by an Ultrasonic Spray Pyrolysis Technique. *RSC Adv.* **2012**, *2*, 10639.

[44] Raut, N. C.; Mathews, T.; Panda, K.; Sundaravel, B.; Dash, S.; Tyagi, A. K. Enhancement of Electron Field Emission Properties of TiO_{2-x} Nanoplatelets by N-doping. R*SC Adv.* **2012**, *2*, 812.

Chapter 6

Summary and Scope for Future work.

6.1 Summary

Nano-structured TiO_2 and N-doped TiO_2 thin films are synthesized using a cost effective and environment friendly spray pyrolysis technique by keeping the substrate temperature (T_s) at 400, 450, 500 and 550 °C. Crystallographic studies of the films confirm formation of phase pure anatase TiO_2. Microstructure studies of these films reveal early stages of grain formation at $T_s = 400$ and 450 °C and well defined 20 nm wide and 10 nm long crystalline grains at $T_s = 500$ and 550 °C. Optical absorption studies carried out by using UV-Vis spectrometer reveal formation of interband states in case of N-doped TiO_2. The stoichiometry of the films are calculated from X-ray photoelectron spectra and the film synthesized at $T_s = 450$ °C is found to be nearly stoichiometric compared to the films synthesized at $T_s = 400$, 500 and 550 °C. The chemical nature and location of the nitrogen dopant is deduced using X-ray photoelectron spectroscopy (XPS) and X-ray absorption spectroscopy (XAS), respectively. Nitrogen 1s (XPS) spectra showed three peaks with an energy value of 396.6, 397.5 and $\sim$400eV, corresponding to substitutional nitrogen, interstitial nitrogen and NO species, respectively.[1] Out of these three peaks, the peak at 396.6eV is traditionally referred as substitutional nitrogen by several authors. However, a careful reading of literature revealed that it corresponds to Ti-N bond of Titanium nitride, implying that it merely represents a Ti-N linkage and is not exactly substituting lattice oxygen. As XPS cannot pinpoint the location of the said atom, X-ray absorption studies (XAS) are undertaken to delineate the exact location of nitrogen, which revealed that nitrogen in the TiO_2 host is located at a distance of $\sim$ 2.3 Å. In addition to this, pre-edge region of the XAS reveals three peaks (A1, A2, A3) at 4957, 4961, and 4963 eV corresponding to 1s- $1t_{1g}$, 1s- $1t_{2g}$ and 1s- $3e_g$ electronic transition due to the distorted TiO_6 octahedral geometry in anatase phase of TiO_2.[2,3] Analysis of post edge region of X-ray absorption spectra, which is also known as extended absorption fine structure (EXAFS), reveals that average $(\text{Ti-O})_{axial}$ and $(\text{Ti-O})_{equatorial}$ distances are increased in doped TiO_2 with respect to pristine TiO_2 thin films. The $(\text{Ti-O})_{axial}$ and $(\text{Ti-O})_{equatorial}$ bond lengths for N-doped TiO_2 calculated from EXAFS are found to be in agreement with the theoretically calculated values by Ceotto et. al.[4]

Since, nitrogen doping of TiO_2 leads to creation of oxygen vacancies, oxygen deficient anatase TiO_2 films are synthesized to study the effect of oxygen vacancies alone. For introducing oxygen vacancies, first anatase TiO_2 films are synthesized by the custom made spray pyrolysis unit by keeping the substarte temperature at T_s= 450 °C and 500 °C. These films are then subjected to annealing in vaccum/ reducing (H_2) environment. As, annealing is known to cause phase transition of anatase to rutile, grazing incidence X-ray diffraction (GIXRD) studies are undertaken. GIXRD of the films revealed that there is no change in crystal structure due to annealing. The crystallite sizes are calculated from the GIXRD spectra by using Scherrer formula and are found to be in the range 29 to 91 nm. The formation of oxygen vacancies, due to annealing in vacuum/ reducing environment, is ascertained by comparing the co-ordination number (C.N) obtained from EXAFS analysis with the C.N obtained by using the equation devised by Frenkel et. al. for calculating the C.N in nanoparticles.[5] The calculated C.N for the nano-sized crystallites of oxygen deficient TiO_2 films in the present study is found to be 5.9. C.N obtained from EXAFS analysis is less than 5/5.7 for oxygen deficient TiO_2 films synthesized at T_s= 450 °C /500 °C. Comparison of C.N obtained from EXAFS studies and the theoretical calculation using Frenkel's equation proved that the oxygen vacancies are indeed created in TiO_2 films due to vacuum/H_2 annealing and is not due to nano-sized crystallites. Furthermore, it is observed that the films synthesized and annealed at T_s = 450 °C are more oxygen deficient (CN of TiO_{2-x}-450 °C is in the range of 4.6 to 4.8) compared to the films synthesized at T_s = 500 °C (CN of TiO_{2-x}-500 °C is in the range of 4.6 to 5.7). This is attributed to the porous microstructure of the film synthesized at T_s = 500 °C, which undergoes surface restructuring and absorbs the desorbed oxygen species available near surface as pointed out by Krivstov et.al.[6] In addition, the effect of oxygen vacancy on the local structure is understood by analyzing X-ray absorption near edge spectra (XANES). XANES of oxygen deficient TiO_2 films show three peaks (A_1, A_2, A_3) positioned around 4957, 4961, and 4963 eV with varying intensity. Analyzing peak position and height of A_1, A_2 and A_3 reveals that oxygen deficient TiO_2 films consist of both six and few five coordinated Ti centers. In addition to the above, oxygen vacancies are known to induce disorderness in the system, which is reflected in the integrated intensity of A_2 peak. To understand this, A_2 peak was fitted and its integrated intensity is found to be highest for the films annealed for 2 hours. This is in accordance with the fact that grain size and crystallinity increases with increase in annealing time as given in the literature. Comparison between theoretically simulated XAS spectra using FEFF with the experimental result reveals that oxygen deficient anatase TiO_2 also gives rise to three pre-edge peaks and there is no change in the local symmetry owing to oxygen deficiency.

Nitrogen doping and oxygen vacancies change the electronic structure of TiO_2, which in turn can make the films visible light active. Hence, wetting studies are performed on these films. The photo-induced wetting studies of N-doped TiO_2 films reveal, they become superhydrophilic upon 40 min sunlight irradiation and revert back to hydrophobic state when kept in dark for 5 days. This confirms the switching (hydrophobic $\leftrightarrow$ superhydrophilic) behaviour and the rate of hydrophobic $\rightarrow$ superhydrophilic and superhydrophilic $\rightarrow$ hydrophobic transition is found to be 0.224 min^{-1} and 2.03 x 10^{-4} min^{-1}, respectively. Similar photo-induced wetting behaviour is also observed for oxygen deficient TiO_2 films.

6.2 Scope of Future Work

- Oxygen deficient TiO_2 synthesized by vacuum annealing has been studied. The samples synthesized under reductive atmosphere could not be pursued due to difficulties in handling H_2. Hence, an extensive study of oxygen deficient TiO_2 synthesized by annealing films under hydrogen atmosphere can be pursued further.

- Oxygen vacancies alters the band gap by reducing Ti^{4+} states to Ti^{3+}.Since, Ti 3d states contribute primarily to the conduction band of TiO_2, it is expected that oxygen vacancies would affect the conduction band of TiO_2. Hence, a detailed band structure analysis can be undertaken for oxygen deficient TiO_2 films by using Ultraviolet Photo-electron Spectroscopy (UPS) and Reflection high-energy electron loss spectroscopy (RHEELS).

- Wetting studies of doped and oxygen deficient TiO_2 revealed reversible hydrophobic to superhydrophilic conversion of TiO_2 surfaces upon sunlight irradiation. Though superhydrophilicity is attained in 40 to 50 mins, its reversal to initial hydrophobic state when kept in dark took a long time. Hence, efforts should be made to reduce the superhydrophilic to hydrophobic state, so that the material can truly be utilised in various applications.

Bibliography

[1] Saha, N. C.; Tompkins, H. G. Titanium nitride oxidation chemistry: An X-ray Photoelectron Spectroscopy Study. *J. Appl. Phys.* **1992**, *72*, 3072.

[2] Sandstrom, D. R.; Filby, R. H.; Lytle, F. W.; Greegor, R. B. Study of Ti in Solvent-Refined Coal by X-ray Absorption Spectroscopy. *Fuel.* **1982**, *61*, 195.

[3] Chen, L. X.; Rajh, T.; Wang, Z.; Thurnauer, M. C. XAFS Studies of Surface Structures of TiO_2 Nanoparticles and Photocatalytic Reduction of Metal Ions. *J. Phys. Chem. B.* **1997**, *101*, 10688.

[4] Ceotto, M.; Lo Presti, L.; Cappelletti, G.; Meroni, D.; Spadavecchia, F.; Zecca, R.; Leoni, M.; Scardi, P.; Bianchi, C. L.; Ardizzone, S., About the Nitrogen Location in Nanocrystalline N-Doped TiO_2: Combined DFT and EXAFS Approach. *J. Phys. Chem. C.* **2012**, *116*, 1764.

[5] Frenkel,A. I.; Yevick, A.; Cooper, C.; Vasic,R. Modeling the Structure and Composition of Nanoparticles by Extended X-Ray Absorption Fine-Structure Spectroscopy. *Annu. Rev. Anal. Chem.* **2011**, *4*, 23.

[6] Krivtsov,I.; Ilkaeva, M.; Salas-Colera, E.; Amghouz, Z.; Garcia,J. R.; Diaz, E.; Ordonez, S.;Villar-Rodil, S. Consequences of Nitrogen-Doping and Oxygen Enrichment on Titanium Local Order and Photocatalytic Performance of TiO_2 Anatase. *J.Phys. Chem. C.* **2017**, *121*, 6770-6780.